A Fast Pixelated Thermal-Neutron Detector

Rofors, Emil

2020

A Fast Pixelated Thermal-Neutron Detector

EMIL ROFORS | DEPARTMENT OF PHYSICS | LUND UNIVERSITY

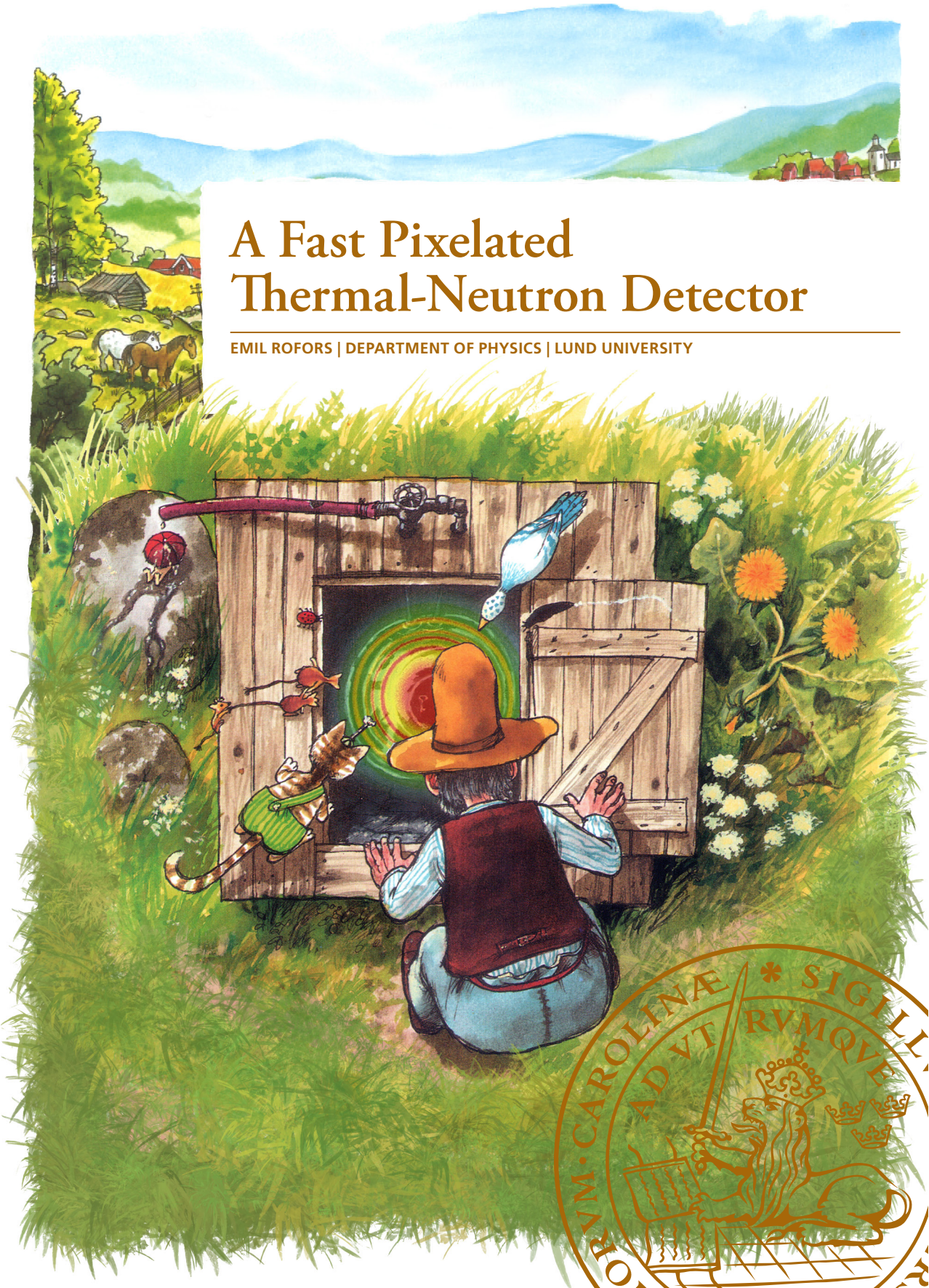

The books about the inventive old man Pettson and his talking cat Findus, by Swedish author Sven Nordqvist, nurtured my curiosity as a child and are very dear to me. The research journey over the past 4.5 years that resulted in this thesis resembles the story when Pettson set out to make a "pancake cake" for Findus' birthday. To make the pancakes they need flour, to get flour they need a bike, to fix the bike they need to get into a shed, to get into the shed they need to get the shed key that's down in the well, to get the key out of the well they need... And so the children's story goes.

Fundamental knowledge of the world around us will be provided by the neutrons of the European Spallation Source. Revolutionizing materials, improved medicines, new solutions for renewable energy, discoveries in magnetism and much more await from the research to be performed. To make use of the neutrons we need to detect them, to detect the neutrons we need to convert them to other particles, to read out the converted particles we need them to generate scintillation light, to register the scintillation light we need... And so the research story goes as well.

In this thesis, the recipe for our pancake cake is presented. Ingredients include 1 Pelletron accelerator, 2 simulation toolkits, 3 research reactors, 4 particle beams, and 5 countries to host our efforts in their labs.

Oh, and in the end, ***spoiler alert*** Findus got a wonderful birthday cake.

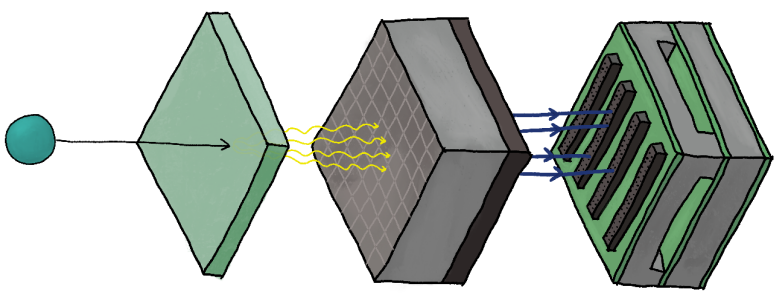

Printed by Media-Tryck, Lund 2020 NORDIC SWAN ECOLABEL 3041 0903

LUND UNIVERSITY

Faculty of Science
Department of Physics

ISBN 978-91-7895-678-4

A Fast Pixelated Thermal-Neutron Detector

A Fast Pixelated Thermal-Neutron Detector

by Emil Rofors

LUND
UNIVERSITY

Thesis for the degree of Doctor of Philosophy

Thesis supervisors: Dr. Kevin Fissum and Dr. Hanno Perrey

Faculty opponent: Dr. Bradley David Sawatzky,
Jefferson Lab
12000 Jefferson Ave
Newport News, VA 23606, USA

To be presented, with the permission of the Faculty of Science of Lund University, to the public in the Rydberg lecture hall at the Department of Physics, Professorsgatan 1, Lund, on Friday, the 18th of December 2020 at 13:15.

Organization
LUND UNIVERSITY
Department of Physics
Box 118
SE–221 00 LUND
Sweden

Document name
DOCTORAL DISSERTATION

Date of disputation
2020-12-18

Sponsoring organization

Author(s)
Emil Rofors

Title and subtitle
A Fast Pixelated Thermal-Neutron Detector

Abstract

This thesis presents the study of a position-sensitive scintillation-based detector called the Solid-State Neutron Detector (SoNDe). SoNDe is being developed for cold- and thermal-neutron detection at the small-angle neutron scattering (SANS) instrument SKADI at the European Spallation Source (ESS), currently under construction in Lund, Sweden. The response of the detector scintillator, multi-anode photomultiplier (MAPMT), and readout electronics has been investigated using particles relevant in the ^{6}Li(n,^{3}H)α reaction that is at the heart of the detection principle of SoNDe. Scintillation light was read out by the 8×8 pixel H12700A MAPMT. The pixel signal is strongly dependent on position and in general several pixels will register a signal (a hit) above a given threshold. To optimize planned detector operation at ESS, the number of pixels above set thresholds was investigated, with the maximization of the single-hit efficiency over the largest possible area as the primary goal. Paper I describes introductory tests validating the detector concept using signal generators and neutrons read out using the SoNDe electronics. Paper II is the first of three systematic irradiation studies and is performed with a broad α-particle beam from a radioactive source using a VME-based data-acquisition system. Scans of highly focused beams of protons and deuterons from a Pelletron across the detector are presented in Paper III. Scans of a collimated thermal-neutron beam from a reactor read out using the SoNDe readout electronics is presented in Paper IV. A simulation model developed using GEANT4 and tuned with the measurements reported in Papers I–IV is described in detail in Paper V. For all of the beams employed in this thesis, the optimal threshold for single-hit efficiency was found at a value of ∼50% of the mean of the full-deposition peak. Of the detected particles, ∼80% were registered in a single pixel. Lower thresholds resulted in higher pixel multiplicities. These events could be localized with better than 5 mm position resolution and could potentially facilitate operation of the detector in a higher multiplicity mode while still fulfilling the 6 mm neutron position-reconstruction accuracy requirement set by the SANS program to be performed at the SKADI instrument.

Key words
SoNDe, thermal-neutron detector, GS20 scintillator, Li-glass, H12700A MAPMT, position-dependent response, alpha-particle, proton, deuteron, neutron, ESS, SKADI

Classification system and/or index terms (if any)

Supplementary bibliographical information

Language
English

ISSN and key title

ISBN
978-91-7895-678-4 (print)
978-91-7895-679-1 (pdf)

Recipient's notes

Number of pages
164

Price

Security classification

Signature 

Date 2020-11-10

A Fast Pixelated Thermal-Neutron Detector

by Emil Rofors

LUND
UNIVERSITY

A doctoral thesis at a university in Sweden takes either the form of a single, cohesive research study (monograph) or a summary of research papers (compilation thesis), which the doctoral student has written alone or together with one or several other author(s).

In the latter case the thesis consists of two parts. An introductory text puts the research work into context and summarizes the main points of the papers. Then, the research publications themselves are reproduced, together with a description of the individual contributions of the authors. The research papers may either have been already published or are manuscripts at various stages (in press, submitted, or in draft).

Cover illustration front: Pettson and Findus stumble upon a small-angle neutron scattering spectrum on their quest for pancakes, see story on the back cover. Art by Sven Nordqvist, edit by Emil Rofors.

Cover illustration back: SoNDe module by Emil Rofors.

Funding information: The thesis work was financially supported by the European Union via the Horizon 2020 Solid-State Neutron Detector Project, Proposal ID 654124, the BrightnESS Project, Proposal ID 676548, and The Märta and Eric Holmberg Endowment of Fysiografen grant No. 38977.

Faculty of Science, Department of Physics

ISBN: 978-91-7895-678-4 (print)
ISBN: 978-91-7895-679-1 (pdf)

Printed in Sweden by Media-Tryck, Lund University, Lund 2020

Till Månna

Contents

List of Figures

Abbreviations

ACIS Application-Specific Integrated Circuits

ACS All-Channel Spectroscopy

ADC Analog-to-Digital Converter

EFU Event Formation Unit

ESS European Spallation Source

FPGA Field-Programmable Gate Array

FWHM Full-Width at Half-Maximum

GUI Graphical User Interface

LIBAF Lund Ion Beam Analysis Facility

MAPMT Multi-Anode PhotoMultiplier Tube

NRA Nuclear-Reaction Analysis

PIXE Particle-Induced X-ray Emission

PMT PhotoMultiplier Tube

QDC Charge(Q)-to-Digital Converter

SANS Small-Angle Neutron Scattering

SKADI Small-K Advanced Diffractometer

SoNDe Solid-State Neutron Detector

TOF Time Of Flight

VME Versa Module Eurocard

List of publications

This thesis is based on the following publications, referred to by their Roman numerals:

I **Recent Developments SoNDe High-Flux Detector Project**

S. Jaksch,R. Engels, G. Kemmerling, U. Clemens, S. Désert, H. Perrey, C. Gheorghe, A. Fredriksen, P. Øya, H. Frielinghaus, K. Fissum, A. Jalgén, **E. Rofors**, K. Kanaki, R. Hall-Wilton, R. Al Jebali
JPS Conf. Proc. 22, 011019 (2018)
doi: 10.7566/JPSCP.22.011019

II **Response of a Li-glass/multi-anode photomultiplier detector to α-particles from ^{241}Am**
E. Rofors, H. Perrey, R. Al Jebali, J.R.M. Annand, L. Boyd, U. Clemens, S. Desert, R. Engels, K.G. Fissum, H. Frielinghaus, C. Gheorghe, R. Hall-Wilton, S. Jaksch, A. Jalgén, K. Kanaki, G. Kemmerling, V. Maulerova, N. Mauritzson, R. Montgomery, J. Scherzinger, B. Seitz
Nucl. Instr. Meth. Phys. Res. A Vol 929, June 2019, p90-96
doi: 10.1016/j.nima.2019.03.014

III **Response of a Li-glass/multi-anode photomultiplier detector to focused proton and deuteron beams**
E. Rofors, J. Pallon, R. Al Jebali, J.R.M. Annand, L. Boyd, M.J. Christensen, U. Clemens, S. Desert, M. Elfman, R. Engels, K.G. Fissum, H. Frielinghaus, R. Frost S. Gardner, C. Gheorghe, R. Hall-Wilton, S. Jaksch, K. Kanaki, G. Kemmerling, P. Kristiansson, K. Livingston, V. Maulerova, N. Mauritzson, R. Montgomery, H. Perrey, T. Richter, J. Scherzinger, B. Seitz, M. Shetty
Nucl. Instr. Meth. Phys. Res. A Vol 984, Dec 2020, 164604
doi: 10.1016/j.nima.2020.164604

IV **Response of a Li-glass/multi-anode photomultiplier detector to collimated thermal-neutron beams**
E. Rofors, N. Mauritzson, H. Perrey, R. Al Jebali, J.R.M. Annand, L. Boyd, M.J. Christensen, U. Clemens, S. Desert, R. Engels, K.G. Fissum, H. Frielinghaus, C. Gheorghe, R. Hall-Wilton, S. Jaksch, K. Kanaki, G. Kemmerling, I. Llamas Jansa, V. Maulerova, R. Montgomery, T. Richter, J. Scherzinger, B. Seitz, M. Shetty
Preprint to be submitted to Nucl. Instr. Meth. Phys. Res. A
arXiv:2010.06347

V **Simulation of the Response of the Solid State Neutron Detector for the European Spallation Source**
L. Boyd, **E. Rofors**, J.R.M. Annand, K.G. Fissum, R. Hall-Wilton, R. Al Jebali, K. Kanaki, K. Livingston, N. Mauritzson, R. Montgomery, H. Perrey, B. Seitz
Preprint submitted to Nucl. Instr. Meth. Phys. Res. A
arXiv:2010.15695

All papers are reproduced with permission of their respective publishers.

Publications not included in this thesis:

A polyethylene-B_4C based concrete for enhanced neutron shielding at neutron research facilities
D.D. DiJulio, C.P. Cooper-Jensen, H. Perrey, K. Fissum, **E. Rofors**, J. Scherzinger, P.M. Bentleyac
Nucl. Instr. Meth. Phys. Res. A, Vol 859, 1 July 2017, p41-46
doi: 10.1016/j.nima.2017.03.064

A comparison of untagged gamma-ray and tagged-neutron yields from ^{241}AmBe and ^{238}PuBe sources
J. Scherzinger, R. Al Jebali, J.R.M. Annand, K.G. Fissum, R. Hall-Wilton, S. Koufigar, N. Mauritzson, F. Messi, H. Perrey, **E. Rofors**
Appl. Radiat. Isot., Vol 127, September 2017, p98-102
doi: 10.1016/j.apradiso.2017.05.014

Tagging fast neutrons from a ^{252}Cf fission-fragment source

J. Scherzinger, R.Al Jebali, J.R.M. Annand, A. Balac, K.G. Fissum, R. Hall-Wilton, D. Hamilton, N. Mauritzson, F. Messi, H. Perrey, **E. Rofors**
Appl. Radiat. Isot., Vol 128, October 2017, p270-274
doi: 10.1016/j.apradiso.2017.05.022

From micro- to macro-neutron sources: The Lund Broad-band Neutron Facility

H. Perrey, M. Elfman, K. Fissum, R.J.W. Frost, N. De La Rosa, M. Kristensson, P. Kristiansson, N. Mauritzson, F. Messi, C. Nilsson, J. Pallon, **E. Rofors**
E3S Web of Conferences 231, 01005 (2020)
doi: 10.1051/epjconf/202023101005

Populärvetenskaplig sammanfattning på svenska

Forskare i största allmänhet kan vara rätt tokiga, men vad är det som gör bl. a. materialforskare, kemister, biologer och fysiker extra tokiga i de små, neutrala partiklarna neutroner? De finns ju överallt[1] - i luft, i vatten, i metall, i dig, ja i princip alla atomers kärnor innehåller neutroner[2], tillsammans med positiva protoner och omges vidare av negativa elektroner. Avhandlingen du nu läser är gjord med ca en miljards miljards miljoner neutroner (∼50 gram) tillsammans med 50 gram protoner och 0.0000005 gram elektroner[3]. Det forskare är exalterade över är hur mycket detaljerad information en neutron kan avslöja om ett prov som ska undersökas, om neutronen skickas mot provet och får studsa runt mot provets atomer. Just neutraliteten är en av neutronens egenskaper som gör studsandet så givande – utan laddning kan neutronerna passera elektroner som ingenting och studsa mot, eller göra bilder av, atomkärnorna i provet. Detta är principen som forskare vill använda för att pusha sina resultat framåt inom en rad olika områden. För att möjliggöra detta gick 13 europeiska länder ihop och bestämde sig för att bygga världens starkaste neutronanläggning, och att den skulle ligga i Lund! Anläggningen, som kostar nästan 2 miljarder € att bygga, fick namnet European Spallation Source (ESS). "Spallation" är namnet på en metod att knocka neutroner ut från ett ämne. Sådana frigjorda neutroner kan sen styras mot forskarnas prover. För detta har ESS valt den tunga metallen wolfram, som har tätt med neutroner i atomkärnorna, att "spalleras". Neutronerna i wolframet slås genom spallation fria så de kan riktas mot prover som ska undersökas, som i bilden här:

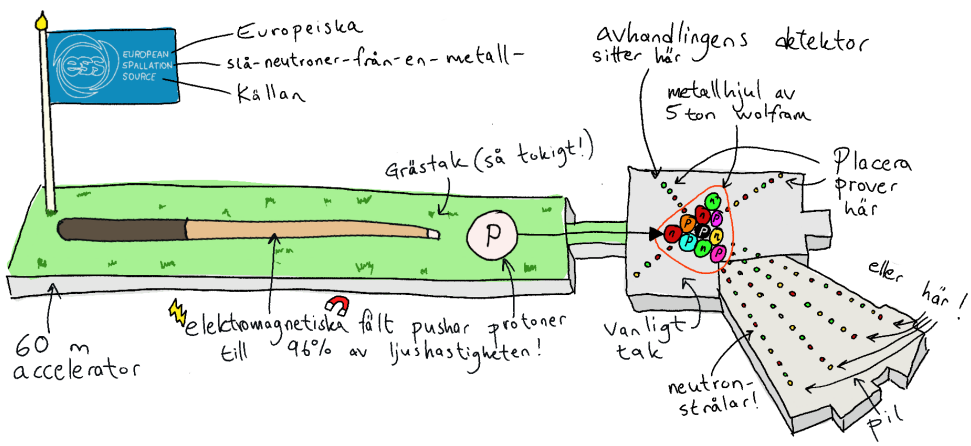

Som vi ser här kommer ESS bestå av en gigantisk biljardkör som accelererar protoner, som i sin tur slår ut neutroner från ett 5 ton tungt metallhjul av wolfram. Ok, det är inte en

[1] neutroner d.v.s., forskare håller sig gärna i mörka källarlabb

[2] utom väteatomer, vars kärna bara består av en proton

[3] och mycket, mycket kaffe

riktig biljardkör, men liknelsen av öppningsstöten i biljard beskriver spallationsprocessen ganska väl. På ESS motsvaras kören av världens starkaste (linjära) accelerator. De bortslagna neutronerna riktas mot 15 olika instrument som alla är specialiserade på olika neutronmätmetoder (endast 7 av neutronstrålarna visas i den förenklade bilden). SKADI är namnet på ett av instrumenten och det är på SKADI, som neutrondetektorn den här avhandlingen handlar om, ska användas.

Kemister, biologer, energiforskare och folk som vill ha detaljerad nanometerinformation om ett prov att vallfärda med sina prover till SKADI när ESS öppnar om några år. En forskare får då först skicka in en ansökan, som beskriver vad som ska undersökas, varför det är nytt och intressant och hur lång tid det kommer ta. En kommitté går därefter igenom alla ansökningar, väljer ut de bästa och delar slutligen ut instrumenttid. Att sedan använda ESS kostar inte forskaren någonting!

Varje instrument behöver ett sätt att fånga upp och detektera neutronerna efter att de passerat proverna. Jämfört med att ta en röntenbild så motsvarar neutrondetektorn röntgenplåten, som sätts in bakom prover eller personer som belyses av röntenstrålning. Det är lätt att missa en neutron när de ska detekteras. Utan laddning far de gärna rakt igenom en detektor. Det finns dock en handfull ämnen som är bra på att fånga upp neutronerna. Ett alternativ är en form av litium, som heter litium-6. Litium-6 går att framställa ifrån naturligt litium och blandat med ett detektionsglas bildas en fönsterglasliknande skiva, som för varje neutron som träffar den blixtrar till. Varje ljusblixt, så kallad scintillation, motsvarar en neutron. Blixtarna är korta och snabba och den snabbheten är nyckeln till att göra en detektor snabb nog att räkna in neutronerna som kommer välla in miljontals om gången. ESS kommer producera fler neutroner per sekund än någon annan anläggning gjort tidigare. Blixtarna registreras i en snabb och mycket ljuskänslig version av en kamera[4] . Snabb blixträkning kräver också snabb elektronik som översätter varje detekterad neutron till en digital signal. Signalen går till en dator för analys så forskaren får ut informationen om och bilderna av provet hen undersöker.

I avhandlingen testas detektorn på flera sätt för att bedöma huruvida den kan klara ESS-jobbet och i så fall hur den ska användas på bästa sätt. Varje neutron som detektorn missar är en förlorad neutron, en slösad kostnad och leder till en försämrad bild. Efter att ha vridit och vänt på detektorn med olika strålningstyper och partiklar, mätmetoder och simuleringar kunde vi konstatera att ja, detektorn levererar. Avhandlingen presenterar metoder för att utnyttja maximalt antal neutroner och när ESS slår upp dörrarna för forskare år 2023 och dessa detektorstudier kommer till nytta, har vi mycket spännande resultat att se fram emot!

[4]ett så kallat multianodsfotomultiplikatorrör[5]

[5]tips till nästa hänga gubbe!

Part I

A Fast Pixelated Thermal-Neutron Detector

Chapter 1

Introduction

1.1 Overview

Since the discovery of the neutron over 80 years ago, neutron scattering has developed into a tool used widely for measuring structures and dynamics in physics, chemistry, biology, and materials science. As the neutron community has expanded, applications have diversified. This has resulted in expanded energy ranges and increased fluxes for neutron beams. Neutron research centers for the general scientific community are evolving from national efforts to international efforts. The European Spallation Source (ESS) [1, 2, 3, 4] is currently under construction in Lund, Sweden. Financed by thirteen member states, it will be the most powerful neutron source worldwide when operation commences in 2023. At ESS, high-energy protons accelerated by a linear accelerator will collide with a rotating heavy-metal wheel to free high-energy neutrons via a process known as spallation, Fig. 1.1. The highly energetic freed neutrons will then be moderated to much lower energies and directed via beam guides towards instrument stations, where they can be employed to study samples of materials via scattering. To extract the information about the samples that the scattered neutrons carry, the neutrons must be detected. Traditionally, nuclear reactions between the neutron and ^{3}He gas have been employed to detect the neutrons. Today, ^{3}He gas has become prohibitively expensive [5, 6, 7, 8], and as a result, detectors which employ alternative techniques have to be developed. This thesis reports on the efforts to develop one such detector, the Solid-State Neutron Detector (SoNDe) [9, 10].

1.2 Beams of neutrons

Chargeless neutrons are fundamental to the existence of nuclei as they facilitate nuclear binding via the strong force. The neutron was discovered in 1932 by James Chadwick (Nobel prize, physics 1935) [11]. The absence of charge makes charged particles such as atomic electrons and even protons electrically invisible to neutrons. Neutrons may thus be used as deeply penetrating, non-destructive probes of matter. Neutron beams are ideal for applications such as imaging and investigating materials.

The neutron-matter interaction probability is dependent on the energy of the incident neutron. Of particular interest to this thesis are thermal neutrons, which are considered to be in thermal equilibrium with their surroundings at room temperature.

The De Broglie wavelength of a neutron is given by

$$\lambda = \frac{h}{p_n} = \frac{h}{\sqrt{2 \cdot m_n \cdot T_n}}\,, \tag{1.1}$$

where λ is the wavelength, h is the Planck constant, p_n is the neutron momentum, m_n is the neutron mass, and T_n is the neutron kinetic energy. Cold and thermal neutrons are thus valuable atomic probes as they have De Broglie wavelengths on the same order of magnitude as inter-atomic distances, 10^{-10} m (1 Å). The energies of these neutrons are also typical for collective excitations in solids and liquids. Typical neutron-energy ranges are displayed in Table 1.1.

Table 1.1: Neutron-energy nomenclatures and ranges. Material physicists typically use units of wavelength when referring to neutron energies.

Type	Energy (eV)	Wavelength (Å)	Speed (m/s)
Cold	$0.01 - 0.025$	$1.8 - 90$	$44 - 2200$
Thermal	0.025	1.8	2200
Epithermal	~ 1	~ 0.3	$\sim 14 \cdot 10^3$
Fast	$> 1 \cdot 10^6$	$< 3 \cdot 10^{-4}$	$> 1.4 \cdot 10^7$

As previously mentioned, spallation is a process where high-energy protons collide with a heavy-metal target releasing high-energy neutrons, Fig. 1.1. The freed neutrons are generally fast, having kinetic energies that are very large (MeV and higher). The large kinetic energy means the De Broglie wavelength is not compatible with inter-atomic distances. Energetic neutrons must thus have their energy reduced in order to make them useful as atomic probes. Moderation (collision-based reduction of neutron energy) generally involves the energetic neutron undergoing elastic scattering from a ^{1}H moderator 10–20 times. The recoiling ^{1}H atoms carry away the excess kinetic energy, resulting in a thermal neutron. At ESS, the moderator design is based upon a volume of supercritical, 17 K, $\geq$99% parahydrogen [12].

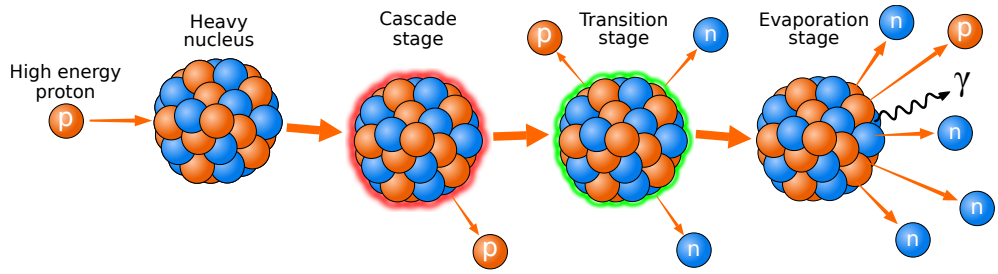

Figure 1.1: The process of spallation. A high-energy proton (left, red) collides with a heavy nucleus. The nucleus then transitions through a Cascade stage (red outline), a Transition stage (green outline), and an Evaporation stage (rightmost image). This results in neutrons (blue) and other forms of radiation, such as protons and γ-rays. The evaporation stage results in the most free neutrons. Figure from [13], reproduced with the permission of the author.

Free neutrons are not stable particles. They β-decay into protons with a halflife of ~10 minutes. Thermal neutrons, despite the 25 meV energy, are not slow – they have a speed of ~2 km/s. Thus, in one halflife, a thermal neutron can travel 1200 km. Moderated neutrons can be directed to drift several 10s of meters from the spallation/moderation site to an experimental station where they may be used to study a sample. By engineering the drift, beams of neutrons with highly specialized properties may be produced.

1.3 Neutron diffraction

The small-angle neutron scattering (SANS) technique exploits elastic scattering of the neutron beam upon sample nuclei, Fig. 1.2. As the name implies, the scattering angle is generally small. The angle 2θ between the incident neutron wave vector $\vec{k}_i$ and the scattered neutron wave vector $\vec{k}_s$ depends on the relative positions of the atoms in the sample. Using the scattering vector $\vec{q}$, the momentum transfer can be defined as $\hbar\vec{q} = \hbar(\vec{k}_s - \vec{k}_i)$. If the scattering is elastic ($|\vec{k}_s| = |\vec{k}_i|$), then

$$|\vec{q}| = 2|\vec{k}| \sin\theta \,. \tag{1.2}$$

The magnitude of the scattering vector $|\vec{q}|$ is q. Equation 1.2 is equivalent to

$$q = (4\pi/\lambda) \sin\theta \,, \tag{1.3}$$

where λ is the De Broglie wavelength of the neutron. Bragg's law states that

$$n\lambda = 2d \sin\theta \,, \tag{1.4}$$

where n is a positive integer and d is the interplanar spacing in the sample. Combining Eq. 1.3 and Eq. 1.4 shows that the momentum transfer is related to probed length scales according to $q = \frac{2\pi}{d}$ [14]. By measuring spatial distributions of detected neutrons which

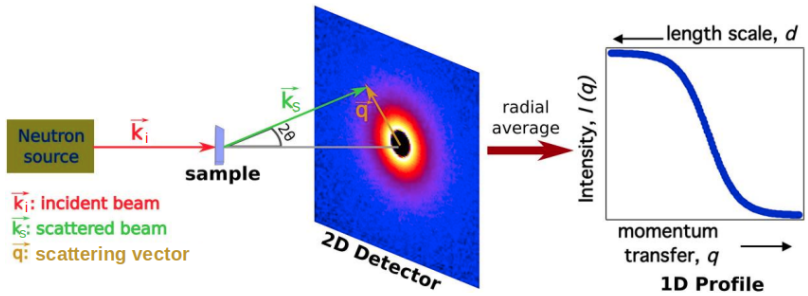

Figure 1.2: The general principle of a small-angle neutron scattering (SANS) experiment. The neutron beam (left) scatters from the sample at different angles. Scattered neutrons are detected in a 2D detector (rings, center, colored plot). For samples with randomly arranged molecules, the scattered intensities can be radially averaged into a 1D representation (right). Figure modified from [14], licensed for reproduction under CC BY 4.0.

have undergone elastic scattering in the q-range 0.0005 - 1 Å^{-1}, it is possible to determine the size, arrangement, and interaction of the components in the sample on scales ranging from µm to Å. SANS can also be used to access information about magnetic structures and interactions through the magnetic dipole moment of the neutron.

The Small-K[1] Advanced Diffractometer (SKADI) [15, 16] at ESS is a SANS instrument designed for very low q-values and high position resolution. The ∼60 m instrument consists of the neutron beamline with choppers and collimation, a sample area, and a detector tube with three neutron-detector planes, Fig. 1.3. The neutron-detector planes will register the scattered neutrons as a function of angle and energy. General design properties of SKADI are:

1. a $3\times3\,\text{m}^2$ sample area and versatile collimation resulting in flexibility
2. good wavelength resolution due to the ∼60 m length
3. access to very small q using focusing collimation elements, down to $\sim10^{-4}\,\text{Å}^{-1}$
4. access to a three-decade q-range in a single configuration
5. access to polarization observables for investigations of magnetic samples and incoherent background subtraction

The combination of the SANS technique and low q-values facilitates the investigation of long length scales. Three detector planes, two of which are movable, enable a large dynamic q-range. An aperture in the upstream detector plane allows neutrons with small scattering angles to pass through to the second detector plane. An aperture in the second detector plane allows neutrons with very small scattering angles to pass through to the third detector

[1] K is an alternate notation to q used in this thesis.

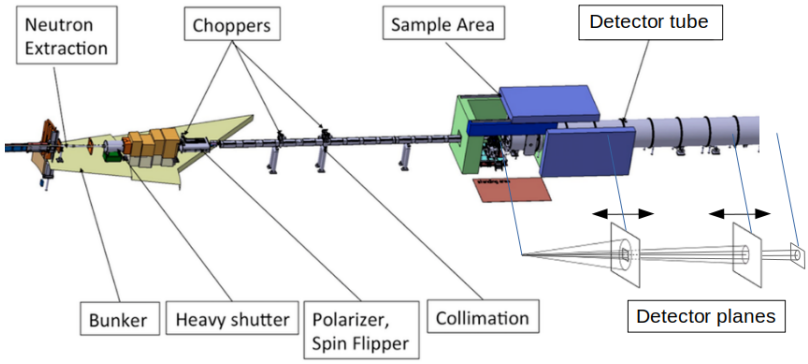

Figure 1.3: Schematic of the Small-K Advanced Diffractometer (SKADI) instrument. Beams of neutrons (from left) are shaped using shutters, choppers, and collimators (middle) and scattered on a sample housed within the blue structure. Configurable detector planes (right) register the scattered neutrons at small angles of deflection. Figure modified from [17].

plane. The unprecedented flux that will be available at ESS will make SKADI able to measure processes happening in samples on time scales previously inaccessible to SANS experiments. The scientific mission of the SKADI instrument translated into detector properties requires:

1. reconstruction of the detected neutron position with an accuracy of $6 \times 6\,\mathrm{mm}^2$
2. sustainable integrated count rates of $\sim$20 MHz over $1 \times 1\,\mathrm{m}^2$
3. a timestamp precision of 150 ns with a resolution of 10 ns

Based on these requirements, the Solid-State Neutron Detector (SoNDe) [9, 10] has been developed.

1.4 Solid-State Neutron Detector

The Solid-State Neutron Detector (SoNDe) is based on a modular design consisting of three basic components, Fig. 1.4:

1. a 1 mm thick cerium-activated ^{6}Li-glass scintillator sheet
2. a Hamamatsu model H12700A 8×8 (64 pixel) multi-anode photomultiplier tube (MAPMT)
3. purpose-built readout electronics

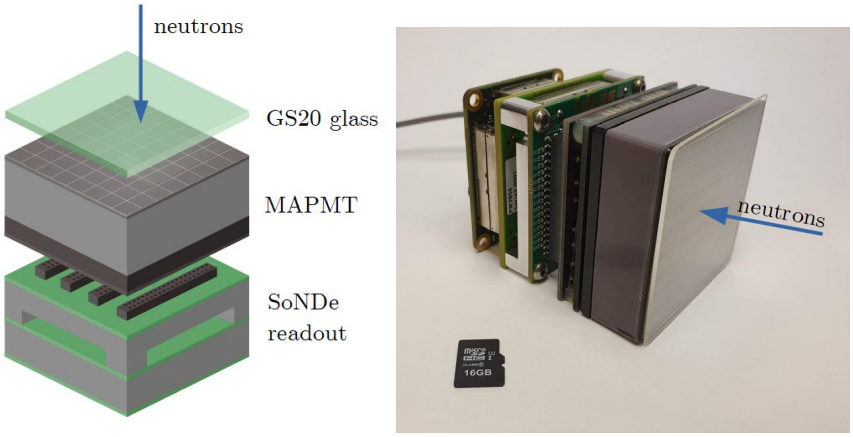

Figure 1.4: Exploded view drawing of a SoNDe module (left) and photograph of the assembled module (right). A micro-SD card is shown in the photograph for scale.

By restricting the readout electronics to the footprint of the scintillator and MAPMT, the modules can be closely packed resulting in configurable detectors with flexible shapes. For the SKADI instrument, 100 panels each consisting of four modules in a 2×2 configuration will be used to construct the three detector planes, for a total of detector area of $1\,\mathrm{m}^2$.

1.4.1 Cerium-activated ^{6}Li-glass scintillator

The properties that allow neutrons to deeply penetrate into samples make it likely that neutrons also pass easily through detector materials. Neutrons are thus difficult to detect, and the method of detection can vary dramatically depending upon the energy of the neutron. As previously mentioned, thermal-neutron detection has relied for decades upon ^{3}He gas which has recently become scarce and thus prohibitively expensive. Detectors based upon ^{3}He gas are also inherently slow. Other more readily available and thus less expensive nuclei which have a large capture cross section for thermal neutrons include ^{6}Li and ^{10}B, Fig. 1.5. Of these, the thermal-neutron capture cross section for ^{6}Li is smaller, but it proceeds via a single branch with a relatively large energy release, Eq. 1.5.

$$^1_0n + \,^6_3\mathrm{Li} \rightarrow \,^3_1\mathrm{H}\,(2.73\,\mathrm{MeV}) + \,^4_2\alpha\,(2.05\,\mathrm{MeV}),\; Q = 4.78\,\mathrm{MeV} \tag{1.5}$$

When a thermal neutron is captured on ^{6}Li, the resulting ^{3}H and α-particle share the Q-value as kinetic energy according to their masses. The deposition of the kinetic energy by the reaction products can lead to their detection. This in turn signals the presence of a neutron. The relatively high Q-value means that neutron reactions will potentially lead to relatively large signals, facilitating their identification.

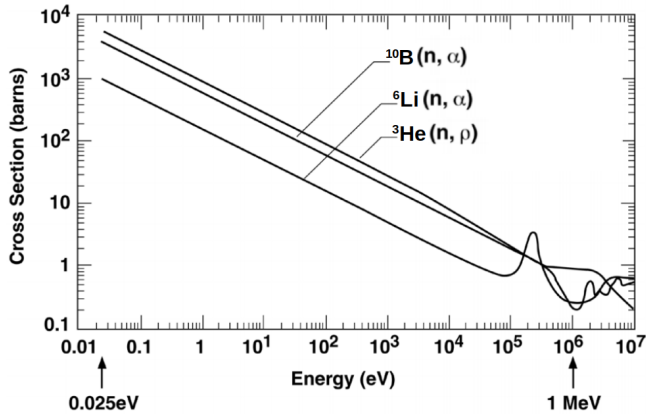

Figure 1.5: Cross sections for neutron-capture reactions in ^{10}B, ^{6}Li, and ^{3}He, all useful for cold- and thermal-neutron detection. Figure from [18].

The earliest use of a scintillator for particle detection was in 1903 by Crookes [19]. A scintillator is a detector material which converts ionizing radiation to visible light. The electrons from scintillator atoms and molecules are excited by the incident radiation to higher-lying states. Upon de-excitation, a flash of light (a collection of scintillation photons) is emitted. The number of scintillation photons is generally proportional to the energy deposited by the incident radiation. Scintillators are fast compared to gas-based proportional counters since the decay times are relatively short (typically 50-75 ns for glass scintillators compared to the electron drift times of typical proportional counters ($\leq$10μs) [19]. Fast signals lead to better time resolution since two pulses produced close in time may be separated. Scintillators are highly suitable for the detection of neutrons in high-flux environments.

When ^{6}Li is evenly distributed in a glass, the inorganic scintillator ^{6}Li-glass results. The production of scintillation light in a glass is defined by the electronic band structure. Regularities in the structure of the glass results in band gaps [20]. The scintillation process usually progresses via the addition of an activator to the glass which results in energy states within the band gap, Fig. 1.6. These band-gap energy states enable lower-energy transitions. Careful selection of the activator facilitates the tuning of the wavelength of the scintillation light. Ginther and Schulman first formulated cerium-activated glasses in 1958 [21] which produce blue scintillation light. Cerium-activated ^{6}Li-glass is fast (few ns ristime, 10s of ns falltime) but has a relatively low scintillation-light output and is sensitive to γ-ray radiation.

Table 1.2: Properties of the cerium-activated ^{6}Li-glass scintillator GS20 [22, 23].

Total lithium (weight%)	6.60%
^{6}Li isotopic enrichment	95%
Thermal neutron efficiency for 1 mm glass	~75%
Density	2.5 g/cm^{3}
Light output relative to anthracene	20-30%
Wavelength of maximum emission	395 nm
Decay time	50-70 ns

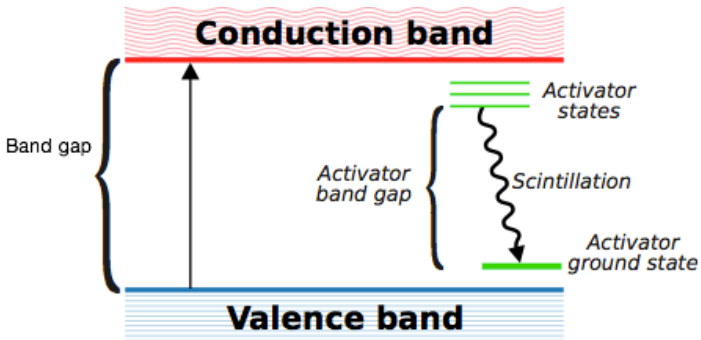

Figure 1.6: Electronic-band structure of an inorganic scintillator. Electrons in the valence band (blue) are excited to the conduction band (red) by the energy deposition of a particle in the scintillator. From the conduction band, the electrons de-excite via near-lying activator states (green) to the activator ground state by the emission of scintillation photons. Figure from [13], reproduced with the permission of the author.

GS20 is the widely available cerium-activated ^{6}Li-glass chosen for the SoNDe detector, Table 1.2.

1.4.2 Multi-anode photomultiplier tube

In the early days of scintillators, light flashes were registered by the human eye and counted. In 1944, Curran and Baker revolutionized scintillator usage by replacing the eye with the newly developed photomultiplier tube (PMT) [24]. PMTs are devices which register scintillations and convert them into electronic signals. Today, PMTs are standard devices employed for the detection of scintillation-light flashes. A drawback of a PMT with a single anode is that it may not be used to measure the spatial distribution of the incoming radiation. PMTs were thus made smaller and smaller, a simplistic approach to increased position resolution that was not sustainable. A more recent approach to miniaturization has been the development of the multi-anode photomultiplier tube (MAPMT). Conceptually, a MAPMT may be thought of as a tightly packed cluster of single-anode PMTs in a single housing, Fig. 1.7.

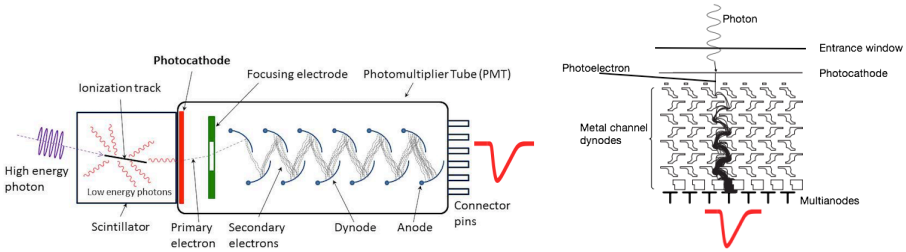

(a) PMT **(b)** MAPMT

Figure 1.7: Signal multiplication in a (single-anode) PMT (a, left) and MAPMT (b, right). A scintillation photon frees a single primary photoelectron at the photocathode. This photoelectron results in a signal at the (multi)anode represented by the red analog pulse. Figures from [25, 26].

Scintillation photons enter photomultipliers via an optical window and strike the photocathode. The quantum efficiency ($\sim$33%) represents the probability that a scintillation photon frees a single primary photoelectron via the photoelectric effect [20]. The single primary photoelectron is then accelerated and steered through a series of dynodes by an applied high voltage. At each dynode multiplication occurs. The end result is an analog pulse of electrons at the anode. The total charge amplification is $\sim 10^6$. A thermal neutron incident upon GS20 can result in 100s of scintillation photons at the photocathode. The charge in the net analog pulse corresponding to the thermal neutron is thus the sum of the charges due to the 100s of individual scintillation photons. This net charge is proportional to the kinetic energy deposited in the scintillator by the products, 4.78 MeV (the Q-value of the original reaction).

1.4.3 Signal processing

The analog electrical signals produced by the detector must be processed in a data-acquisition system (DAQ). Digitization is a common approach. Figure 1.8 displays an analog signal, similar to that generated by the MAPMT in Fig. 1.7, as an illustration of the analog-to-digital conversion (ADC) concepts of peak voltage V_{peak} and integrated current Q_{int}.

A voltage-to-digital converter (VDC) is a device that locates the peak voltage of the analog current pulse. The peak voltage V_{peak} is proportional to the energy deposited in the scintillator. A charge-to-digital converter (QDC) integrates the analog current pulse $i(t)$ over a time window known as a "gate" opening at T_{start} and closing at T_{stop} to yield the integrated current Q_{int}, Eq. 1.6.

$$Q_{\text{int}} = \int_{T_{\text{start}}}^{T_{\text{stop}}} i(t)dt \tag{1.6}$$

The charge Q_{int} is also proportional to the energy deposited in the detector by the event.

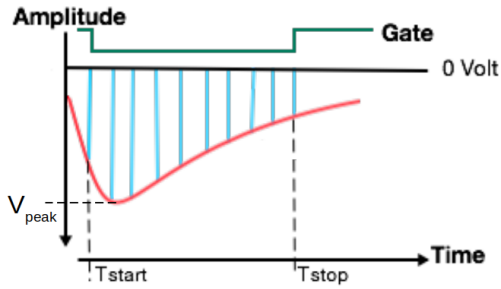

Figure 1.8: Analog-to-digital conversion, voltage and charge concepts. The red analog current pulse produced by the detector may be analyzed for V_{peak} (labeled) or Q_{int} (blue area).

Digitization of analog signals is a time-consuming process which results in rate-limiting deadtime as detectors must be inhibited during the time necessary to perform the digitization. The necessary signal pre-processing such as signal shaping, trigger and gate generation, and digitization is often achieved using generalized Versa Module Eurocard (VME) electronics modules. Well-understood VME electronics are envisioned for many tasks and tend to be slow and cumbersome, Fig. 1.9 (left panel). A much less cumbersome but also less generalized approach to signal digitization is employing Application-Specific Integrated Circuits (ASICs). An ASIC is, as the name implies, an embedded circuit developed for a single, specific purpose. Once produced, an ASIC cannot be reconfigured for other tasks. On the other hand, a Field-Programmable Gate Array (FPGA) can be programmed to perform different tasks but lacks some of the speed of an ASIC. FPGAs may be thought of as ASIC breadboards. The SoNDe custom readout electronics employ four ASICs for continuous MAPMT-signal processing. Each ASIC reduces 16 MAPMT channel signals into one analog output per ASIC. An FPGA is used for time stamping, pixel determination, and to control ADC readout of ASIC signals [9]. Figure 1.9 (right panel) shows the SoNDe readout electronics. The readout electronics can be configured to operate in two different modes:

1. All-channel Spectroscopy (ACS) mode, where once one of the 64 ASIC channels output a value higher than a set threshold, all 64 ASIC channels are digitized and their pulse heights are transferred with the current timestamp

2. Time-of-flight (TOF) mode (speed is the focus), where the digitization of pulse heights is skipped and only the pixel IDs of pixels above threshold are transferred with the current timestamp

Data acquired in TOF mode thus contain no underlying pulse-height information, simply which pixels had signal above a set threshold. Events involving the firing of a single pixel (multiplicity $M = 1$ events) are thus desirable as they are straightforward to interpret. Events

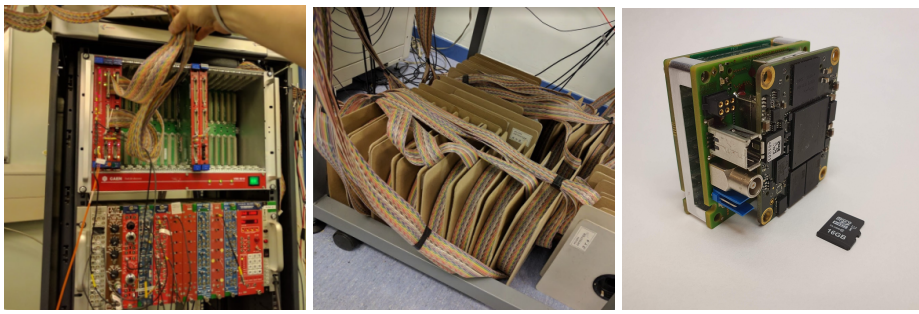

Figure 1.9: Signal-processing electronics. A comparison between the footprint of quasi-digital VME electronics and the corresponding custom SoNDe module electronics. VME-associated electronics (left). VME-associated delay cable (middle). Custom SoNDe readout electronics (right).

with higher multiplicities generally correspond to an area of two or more pixels and are thus outside the 6 mm resolution requirement of SKADI. The data acquired with the SoNDe module in this thesis were acquired using ACS mode. Data may always be reduced from an ACS-mode representation to a TOF-mode representation offline.

1.5 Visualization

Simulations are powerful tools used to aid in the interpretation of data. In this work, simulations were extensively employed to aid in the visualization of the processes leading to the detected signals. A precise detector model together with a detailed simulation should be able to replicate measured data and also provide insight into the behavior of new configurations. Deterministic models take input and apply equations to unambiguously determine output. Stochastic models, such as Monte Carlo simulations, take input and add an element of randomization to the equations so that probabilities determine the output. Deterministic models are thus generally simpler but can still provide useful insight into stochastic models.

The visualization of the transport of (scintillation) light is a key component to the understanding of the behavior of the data interpreted in this work. For light passing through a boundary between two media, Snell's law gives the angle of the transmitted light ray θ_t with respect to the normal of the boundary between the two media as

$$\theta_t = \sin^{-1}\left(\frac{n_i \sin\theta_i}{n_t}\right), \tag{1.7}$$

where n_i is the index of refraction and θ_i is the angle of the light ray in the medium of incidence, while n_t is the index of refraction of the medium of transmission. The Fresnel equations describe the fractions of light $R_{\parallel}$ and $R_{\perp}$ that are reflected at the boundary

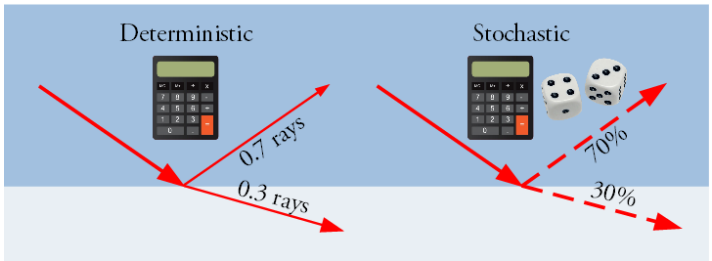

Figure 1.10: Deterministic and stochastic modeling. Comparison of deterministic (left) and stochastic (right) modeling of light passing into a lower refractive-index medium (light-blue band, bottom). The red vectors indicate the directions of the light rays. The deterministic model will divide the light in exact portions while the stochastic model allows each photon to reflect or transmit individually.

between the two media as

$$R_{\parallel} = \left| \frac{n_i \cos\theta_t - n_t \cos\theta_i}{n_i \cos\theta_t + n_t \cos\theta_i} \right|^2 , \; R_{\perp} = \left| \frac{n_i \cos\theta_i - n_t \cos\theta_t}{n_i \cos\theta_i + n_t \cos\theta_t} \right|^2 , \tag{1.8}$$

where $R_{\parallel}$ is the reflected power for light polarized parallel to the plane of incidence and $R_{\perp}$ for light polarized perpendicular to the plane of incidence. Unpolarized light results in $R = (R_{\parallel} + R_{\perp})/2$, and the conservation of energy means that the amount of transmitted light T is given by $T = 1 - R$. An illustration of the difference between the deterministic and stochastic approaches to the modeling of the passing of light from a medium with a lower index of refraction to a medium with a higher index of refraction is shown in Fig. 1.10.

1.5.1 Ray Optics Simulation

The Ray Optics Simulation [27] is an open source, deterministic simulation of light reflection and refraction. It models light propagation in 2D in a clear and user-friendly manner and facilitated early-stage modeling of the scintillation-light spread in the GS20 and MAPMT window upstream of the photocathode. Since the average ranges of the ^{3}H and α-particle in GS20 (recall Eq. 1.5) are 34.7 µm and 5.3 µm respectively [28], a neutron-absorption event could be well-approximated with a point source. A visualization of the scintillation light corresponding to a neutron-absorption event in the exact center of the GS20 sheet is shown in Fig 1.11. The figure clearly demonstrates the reflection and transmission of scintillation light throughout the detector components.

The model lacked degrees-of-freedom such as wavelength dependence for the index of refraction, non-linear geometries, and a third spatial dimension. Nevertheless, it was a valuable tool which provided useful insights and guidance in the early stages of this project.

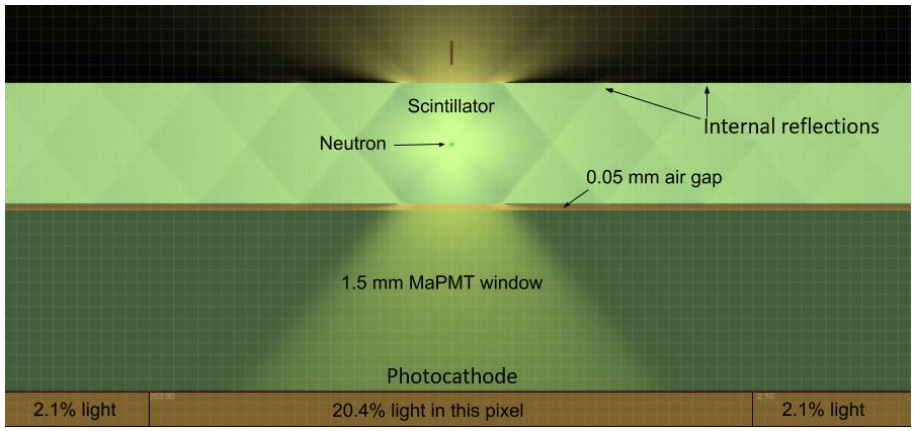

Figure 1.11: Ray Optics Simulation visualization. A 2D visualization of the scintillation-light spread subsequent to a neutron-absorption event in the exact center of the GS20 sheet (light green band across the middle of the figure). The yellow plume at the top of the figure is scintillation light escaping the non-instrumented side of the GS20 sheet. The yellow plume at the bottom of the figure is scintillation light which eventually reaches the photocathode.

1.5.2 GEANT4

GEANT4 [29, 30, 31] is an open source, stochastic simulation framework capable of modeling essentially all the processes involved in the detection of subatomic particles, from the characteristics of the incident beam, to the energy deposition and tracking of secondary particles, to the generation, propagation (recall Eqs. 1.7 and 1.8), and detection of the resulting scintillation light on the basis of individual scintillation photons (see below). A GEANT4 simulation requires detailed knowledge of geometries, material properties, and the source of irradiation. In general, if the model is correct, precise input parameters produce realistic results. For ease of use, the model read configuration parameters such as GS20 dimensions, grooving, optical coupling, incoming beam, and irradiation positions from a macro file. Particle interactions (including secondaries, tertiaries etc.) are sampled from extensive data libraries.

The mechanism for the production of scintillation light that went unaddressed in the Ray Optics Simulation is one of the strengths of the GEANT4 framework. The integrated light output of a scintillator $L(E)$ is a function of the type and energy E of the incident charged particle [32, 33] and is given as

$$L(E) = S \int_0^E \frac{dE}{1 + kB(\frac{dE}{dx})}, \tag{1.9}$$

where S is related to the scintillation efficiency, kB is the Birks parameter (see below), and dE/dx is the specific energy loss of the particle. The heavier the incident particle, the greater the probability that energy deposited in the scintillator does not yield scintillation photons, instead taking the form of heat. This is known as ionization quenching. In the

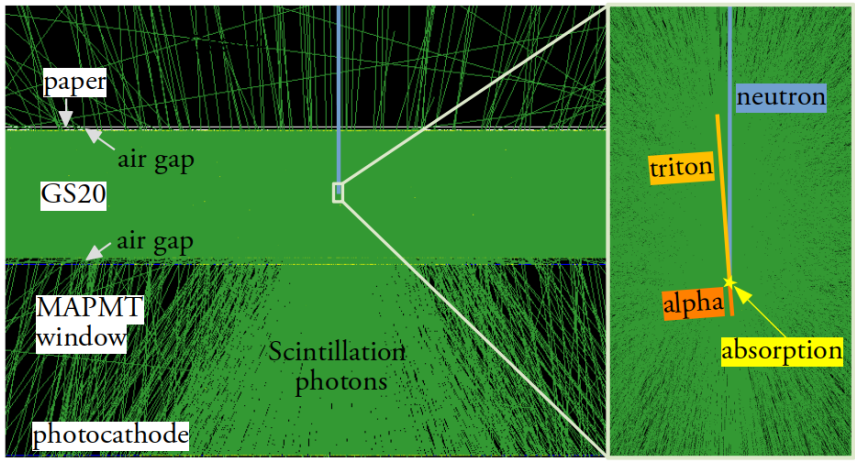

Figure 1.12: GEANT4 visualization. A 2D projection of a 3D visualization of the interaction between a thermal neutron and the GS20 sheet. (Left panel) The dark band at the top is upstream of the detector. A neutron (blue vertical line) is incident on the GS20 sheet (green band across the middle of the figure) from above, and a neutron-absorption event occurs in the center (white square). The GS20 sheet is saturated with scattering scintillation photons which are shown in green. The green plume at the bottom of the panel is scintillation light which eventually reaches the photocathode. (Right panel) enlargement of the small white square in the left panel. The yellow star indicates the point of neutron absorption, and the α-particle and ^{3}H tracks are shown.

context of this thesis, per unit of deposited energy, the resulting scintillation light yield is ranked as $^1\mathrm{H} > {}^2\mathrm{H} > {}^3\mathrm{H} > \alpha$-particles as a function of incident particle type. Thus, for the primary neutron-detection mechanism in GS20, when a neutron is absorbed by ^{6}Li resulting in a 2.73 MeV ^{3}H (range 34.7 µm) and 2.05 MeV α-particle (range 5.3 µm), quenching results in the ^{3}H dominating the production. By adjusting the Birks parameter kB to fit the shape of scintillation-light yield and S to account for the magnitude, the neutron-scintillation properties of GS20 may be extracted. Further precision may be obtained by examining the response of GS20 to individual ^{3}H and α-particle beams.

Figure 1.12 is a GEANT4 version of Fig. 1.11 (the Ray Optics Simulation) and shows GEANT4 predictions for the absorption of a thermal neutron in the center of the GS20 sheet. This is a 2D projection of a 3D visualization. This simulation is far more advanced, and in addition to scintillation-light transport, includes the incident thermal-neutron beam, the reaction between the neutron and the GS20, the ranges and energy depositions of the reaction products, and the scintillation-light production and quenching. A difference here is that a piece of paper is included on the upstream side of the GS20 sheet and reflects light back into the scintillator. Imperfect surface finishes are implemented via the polish parameter of the `Glisur` model in GEANT4 . The net result is a distribution of scintillation photons reaching the photocathode, which can be compared to the electronic signals discussed in Sec. 1.4.3.

Figure 1.13 shows GEANT4 predictions (2D projections) of scintillation-light cones result-

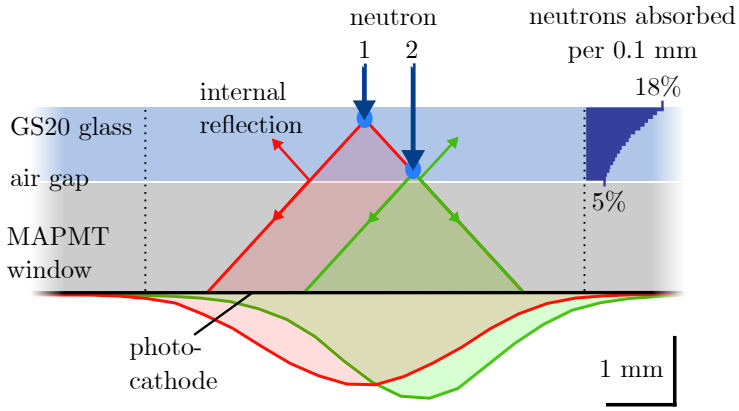

Figure 1.13: Scintillation-light distributions from GEANT4 . 2D representations of GEANT4 simulated scintillation-light cones (triangles) and photocathode yields (inverted normal distributions) resulting from interactions at the upstream GS20 surface (neutron 1, red) and the downstream GS20 surface (neutron 2, green). Vertical dotted lines indicate pixel edges. The number of interacting neutrons is shown as a function of penetration depth into the GS20 sheet in the top-right corner.

ing from neutrons interacting at the upstream and downstream edges of the GS20 sheet. The projections represent the opening angle defined by total internal reflection, and have been drawn to guide the eye to the simulated scintillation-light distributions arriving at the photocathode of the MAPMT. Scattering of scintillation photons results in the tails. The number of interacting neutrons shown as a function of penetration depth into the GS20 agrees with the thermal-neutron detection efficiency presented in Table 1.2.

The time invested in becoming familiar with the daunting GEANT4 toolkit over the course of this thesis was significant. The degree of familiarity required for the simulation of a SoNDe module on the level of individual scintillation photons was substantial. The insight provided has been invaluable.

1.6 This thesis

1.6.1 Goal

This goal of this thesis is to provide a *de facto* feasibility study, where the "as-built" response of a SoNDe module to incident radiation is correlated to the design goals of the SKADI instrument (recall Sec. 1.3). Specific goals included:

1. investigation of the response of the SoNDe module to beams of thermal neutrons as well as beams of α-particles and ^{3}H (recall Eq. 1.5). Beams of protons and deuterons were used to approximate beams of ^{3}H
2. examination of methods to increase the localization of the scintillation signal with a view to optimizing the position resolution of the SoNDe module under the constraints imposed by the single-hit ($M = 1$) mode of operation envisioned for ESS
3. identification of an algorithm to determine the "ideal" detector threshold that maximizes the number of single-pixel events
4. study of the position-sensitive response of the SoNDe module as a function of threshold with a precision of better than 1 mm for events triggering two pixels at the vertical and horizontal boundaries between pixels, and up to four pixels at the corners

In accomplishing these project goals, a knowledge database is to be created. This database is to include an archive of all experimental data, contributions to an analysis-code database, contributions to a simulation-code database, and any detector-associated interfaces or tools created. Further, "live" feedback is to be provided to the detector and electronics designers.

The goal of the author is to identify any regions of detector acceptance where an event position-reconstruction accuracy better than 6 mm might be obtained for multiple-hit ($M > 1$) events when operating the detector in TOF mode. This could in principle increase the geometric acceptance of the SoNDe detector while maintaining the critical SKADI instrument design goals. As every neutron produced by an large-scale accelerator such as ESS comes at a price, such a discovery could potentially increase the cost effectiveness of the instrument, particularly over the lifetime of the facility.

1.6.2 Structure

The studies included in this thesis are described in Papers I to V in Part II of the thesis. An attempt to illustrate the relationship between the Papers is presented in Fig. 1.14. The arrows indicate interplay between the studies. The projects reported on in Papers III–V unfolded

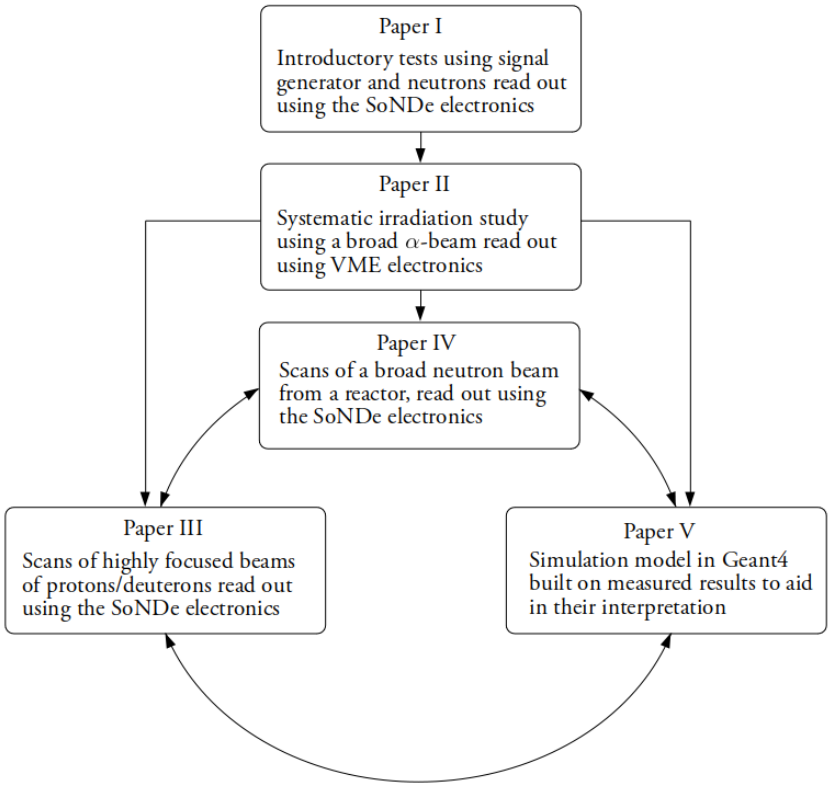

Figure 1.14: Thesis Structure. An overview of the structure of the thesis illustrating the relationship between the Papers resulting from the various projects. Papers III–V progressed more-or-less in parallel.

largely in parallel. On more than one occasion, progress in one of the complementary efforts led to progress in another project. Data analysis was often performed in an iterative fashion. The highly diverse beams provided by different experimental facilities provided datasets with unique strengths and weaknesses. These datasets were used to provide insights into one another. Crucially, the datasets facilitated the development of a sophisticated GEANT4 model of the detector on the level of individual scintillation photons, which in turn provided a much deeper understanding the nuances of particle detection with a SoNDe detector.

Chapter 2

Measurements

2.1 Concept validation tests

2.1.1 Overview

A collection of fundamental tests were performed from 2015 – 2017 which established the basic choices of the key components of a SoNDe module – GS20 as the scintillator, the Hamamatsu 8500A MAPMT [34] (which later evolved to the 12700A) and IDEAS-developed readout electronics[35]. The project is described in detail in Paper I.

2.1.2 Method

At the IDEAS product development lab in Oslo, Norway, a comprehensive suite of bench tests were performed to determine the range of linear response for the readout electronics. To emulate the output of the SoNDe electronics under experimental conditions, a precision pulse generator was employed to pass variable charges at variable rates to the readout, Fig. 2.1. In this manner, the maximum linear rate limit for the SoNDe module was established.

At the research reactor at Heinz Maier-Leibnitz Zentrum (MLZ) [36] in Garching, Germany, the response of a SoNDe module to 4.7 Å cold neutrons was first measured. The data were also used to aid in the development of the core detector software. The radiation hardness of a SoNDe module was also investigated. The radiation hardness of a detector may be thought of as the ability of a detector to withstand the radiation to which it will be exposed over its lifetime. At the research reactor at Laboratoire Léon Brillouin (LLB) [37] outside Paris, France, a SoNDe module was exposed to a white beam (all energies) of neutrons from

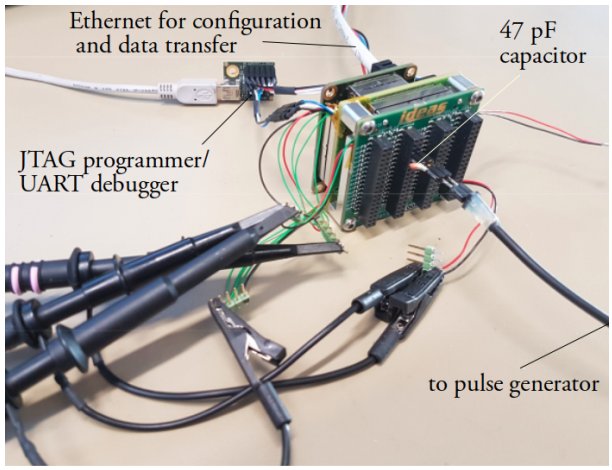

Figure 2.1: Early measurements with a pulse generator. An illustration of the SoNDe electronics development stage with a pulse generator being employed for rate-dependent measurements of linearity in Paper I. The SoNDe module is shown in the upper right-hand corner. Photograph courtesy of IDEAS [35].

the reactor for ∼10 days. This resulted in an integrated dose of neutrons calculated to be equivalent to ∼10 years of operation at ESS. Neutron-radiography images of the module before and after the radiation-hardness test completed the investigation. Data were also taken with a beam of thermal neutrons for various configurations of grooves cut into the scintillator to reduce optical crosstalk between pixels.

2.1.3 Simulation

An existing light-transport model developed in Forschungszentrum Jülich [38], Germany, was used to compare different grooving options of the scintillator to maximize the number of single-hit ($M = 1$) events. Mounting the GS20 on a separate intermediate "carrier" glass and cutting grooves all the way through the GS20 was found to be the most promising approach to localizing scintillation. This configuration maximized the amount of scintillation light reaching the pixel closest to the point of a neutron interaction. Applying light-reflecting paint to the grooves cut into the GS20 further enhanced this behavior.

2.2 α-particle measurements

2.2.1 Overview

α-particles are the most intensely ionizing of the products in the ^{6}Li(n,^{3}H)α reaction. The scintillation light they produce is thus the most quenched. Beams of α-particles may

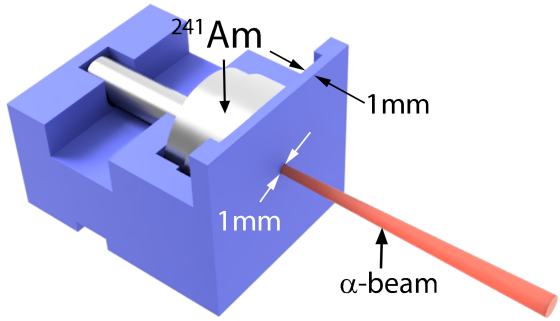

Figure 2.2: Holder and collimator for the thin-windowed ^{241}Am source. 3D-rendering of the assembly used to define α-particle beams for the scans performed in Paper II. The assembly shown has a 1 mm thick face plate and a 1 mm diameter hole, resulting in the diverging red beam of α-particles.

be readily obtained from actinides and are straightforward to handle and even collimate. α-particle irradiations of the SoNDe module were thus judged to be a reasonable starting point for the efforts of the author. In this study performed at the University of Glasgow[39] in the UK, $\sim$4.5 MeV α-particles from a thin-windowed ^{241}Am source were used to study the areal response of the SoNDe module. The beam was systematically scanned across the face of the detector. Signals were read out using a well-established VME-based electronics setup optimized for laser-irradiation studies of MAPMTs [40, 41]. The project is described in detail in Paper II.

2.2.2 Method

Initially, a laser mounted on an XYZ translation stage was used to irradiate the centers of each pixel of the SoNDe module in an effort to reproduce the gainmap supplied by Hamamatsu. The laser was then replaced by a various 3D-printed holders and collimators for the ^{241}Am α-particle source, Fig. 2.2. Varying the amount of air (distance) between the ^{241}Am-source window and the upstream face of the GS20 enabled the energy of α-particles reaching the GS20 to be varied. Due to the low intensity of the source, the smallest diameter collimator employed was 1 mm.

The VME-based DAQ allowed for a detailed study of the response of the GS20 and MAPMT. The VME-based DAQ was triggered on the MAPMT dynode-10 signal, effectively the OR of the 64 pixels. After inversion, amplification, and a small delay, the dynode-10 signal was discriminated and used to create a 200 ns QDC gate with a gate generator. Delayed ($\sim$200 ns, see the spools of flat ribbon cables shown in Fig 1.9, center panel) analog MAPMT signals corresponding to the α-particles being detected in the various pixels were processed using QDCs and stored in a `ROOT` [42, 43] file.

As well-defined points across the face of the detector were irradiated, it became apparent

that the response was highly dependent on the point of irradiation, even on the sub-pixel level. To systematically cover regions of the detector in a grid, automated scans were implemented through the purpose-built MAPMT Scanner GUI developed by the author, see Appendix B. A typical scan of 2×2 pixels could take from 5–15 hours to complete depending on the scan grid pitch and desired statistics. Failures of improvised mounting solutions, detector overheating, electronics issues, and computer hangs caused numerous scans to be lost.

2.2.3 Simulation

The Ray Optics Simulation (Sec. 1.5.1) was used to visualize the manner in which the scintillation photons propagated in the GS20 and MAPMT window. As the α-particles had a range of only 5.3 µm in the scintillating glass, the scintillations were approximated as originating from a point source at the upstream GS20 surface. The Ray Optics Simulation agreed well with the data, which aided in the interpretation. An unexpected observation during these measurements was that an optical coupling such as grease or elastomer was not needed to increase the light-collection efficiency between the GS20 and the MAPMT, despite the low light yield due to the α-particles. In fact, it was shown that such a coupling increased the light spread, resulting in an undesirable decreased single-hit efficiency.

2.3 Proton and deuteron measurements

2.3.1 Overview

The α-particle studies were blurred by the extended beam produced by the 3D-printed collimator and the multiple scattering in the window of the source. However, they clearly indicated that detector response as a function of the point of irradiation, particularly near pixel edges, required further study. Less intensely ionizing than α-particles, ^{3}H-particles suffer less quenching and produce more scintillation light per unit energy. The Lund Ion Beam Analysis Facility (LIBAF) [44] at Lund University in Sweden was employed to provide highly focused (100 µm diameter) beams of protons and deuterons. These beams were used to approximate beams of ^{3}H and provide data complementary to the α-particle results. Data were recorded simultaneously with the both a VME-based DAQ and with the dedicated SoNDe readout (Sec. 1.4.3). The project is described in detail in Paper III.

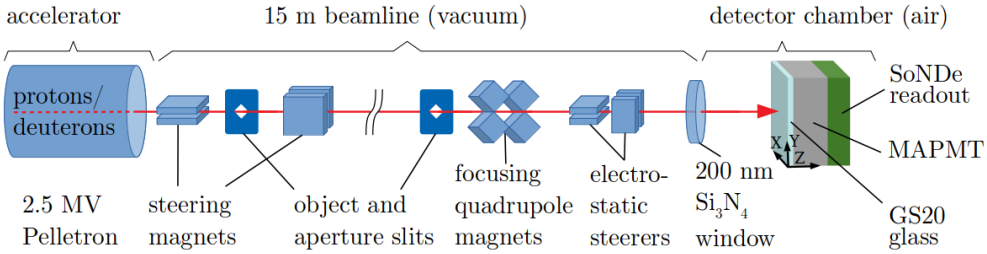

Figure 2.3: Schematic overview of the apparatus. The accelerator (left) produced continuous ∼nA beams. The beams were transported and reduced further in intensity via a beamline (middle) ending in a thin vacuum window. A detector chamber (right) containing a SoNDe module mounted on a motorized XYZ platform was positioned downstream of this window.

2.3.2 Method

Extensive scans of the SoNDe module were performed using the proton and deuteron beams by systematically stepping the detector through the beams provided at the facility, Fig. 2.3.

Three main challenges were identified:

1. beam rates. The 3 MeV Pelletron accelerator normally provides beams of $\sim 10^{10}$ protons per second. For the planned investigations using ACS readout mode, rates of ∼10 kHz were required. Slits were employed.

2. backgrounds. Deuterons with energies of a few MeV produce secondary neutrons when they strike the slits. This resulted in a radiation field that exceeded neutron limits in the experimental hall. A system to position the slits that could be run remotely was developed to control the beam intensity.

3. vacuum. Cooling necessitates that a SoNDe module operate in air, but the accelerator beamline is under vacuum. A thin ∼200 nm Si_3Ni_4 window served as a vacuum-to-air boundary. The energy loss of the beams in the air of the room was exploited to determine the energy of the beam.

With the challenges overcome, scans were successfully performed. The extreme level of beam collimation meant that small drifts in the accelerator had to be manually countered with the steering and focusing magnets every ∼20 minutes. Rates could then be kept between $1 - 10$ kHz, so that a typical scan would take a few hours. The ESS-developed Event Formation Unit (EFU) [45, 46] was used to receive and store the incoming data packages containing the event information from the detector. Data were thus acquired in the fashion anticipated for ESS operation. In this study, the data were stored in .csv

format, and stamped with the beam coordinates for each position of a scan. The scans were controlled using the MAPMT Scanner GUI (Appendix B).

2.3.3 Simulation

By this time in the project, the GEANT4 simulation had matured sufficiently to replace the Ray Optics Simulation. The proton and deuteron datasets demonstrated sensitivity to the choice of the Birks parameter (Eq. 1.9) employed in the simulations. An accurate Birks parameter is required to describe the quenching effects of protons and deuterons in GS20. The GEANT4 simulation replicated the gross behavior of the response of the SoNDe module to the beam scans, but the spread of signal to neighboring pixels was generally underestimated.

2.4 Neutron measurements

2.4.1 Overview

An evaluation of the response of the SoNDe module to collimated beams of thermal neutrons was crucial to the understanding of the device. At the research reactor at the Institute for Energy Technology (IFE) outside of Oslo, Norway, the R2D2 beamline [47] was used to perform these studies. Scintillation-light yield was maximized as both reaction products were detected. This new complementary dataset was recorded with the SoNDe readout (Sec. 1.4.3). The project is described in detail in Paper IV.

2.4.2 Method

Scans of the SoNDe module were performed by stepping the detector through the neutron beams provided at the facility, Fig. 2.4. Neutrons moderated within the reactor were monochromated to 2.0 (18 meV) or 2.4 Å (13 meV) beams. These beams were then collimated using slits [48], a HeBoSint mask [49], and a Mirrobor shielding sheet [50] to 3 mm or 1 mm diameter. The ratio of thermal neutrons from the beam to background in the SoNDe module resulted in the 1 mm diameter lower limit on the HeBoSint pinholes.

The SoNDe module was placed in a black box on an movable XY table. The ESS-developed EFU was used to receive and store data packages containing the event information from the detector. The DAQ engine `Daquiri` [51, 46], also developed by ESS, was used for live plotting of the beam position and ADC spectra, and monitoring beam rates. Data were thus acquired in the fashion anticipated for ESS operation. A socket was established between the

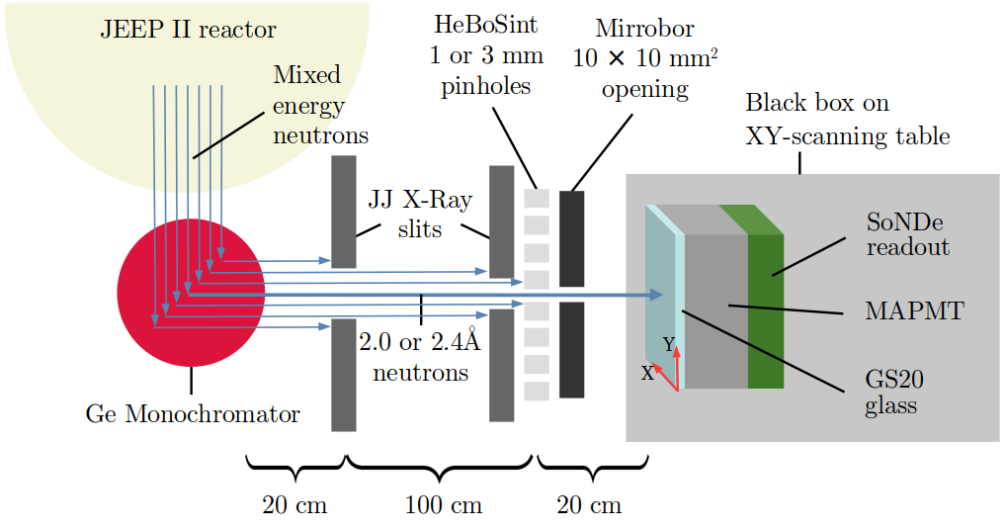

Figure 2.4: Schematic overview of the apparatus. The reactor (yellow half circle, top left) produced a continuous beam of neutrons (blue arrows) which was collimated and monochromated (red circle). The beam was then shaped with a pair of slits, a pinhole mask, and a shielding sheet before striking a black box containing the SoNDe module mounted on a motorized XYZ platform.

EFU computer (Ubuntu 16.04) and the PC that was used to control the beamline through `LabView` (Windows). In this manner, the SoNDe module was configured, measurements were started and stopped, and the detector was scanned using the MAPMT Scanner GUI (Appendix B).

The portable black box made for the measurement proved to be sufficiently light tight but resulted in the SoNDe module overheating. The tight space in the rather small black box caused unexpected failures during long scans due to lack of cooling. A regular table fan blowing on the entire assembly solved this problem. During overnight runs, an automated scan of a 2D grid covering multiple pixels in 0.5 mm steps took ∼10 hours to complete.

2.4.3 Simulation

The ever-maturing GEANT4 model of the SoNDe module was complemented with an algorithm to address electronic crosstalk, Sec. 2.5.3. Simulations of the data from 3 mm diameter neutron-beam scans were performed with slightly larger and smaller beam sizes and varying amounts of crosstalk to recreate the measured response of the detector. Ultimately, the dimension of the beam proved to be too large to precisely determine the level of electronic crosstalk, but the algorithm proved to be very promising.

2.5 GEANT4 modeling

2.5.1 Overview

While technically not a measurement, the large commitment by the author to the development of a precision GEANT4 model of the SoNDe detector led to an investment of at least as much time and energy to this sub-project as to any of the specific measurements. The GEANT4 model of the SoNDe detector was developed with the guidance of Dr. John Annand of the University of Glasgow and has been continually developed and refined throughout the studentship of the author. It is now mature and is described in detail in Paper V.

2.5.2 Method

As previously mentioned, the GEANT4 model has been developed to describe the behavior of the SoNDe module on the level of individual scintillation photons. The data from the α-particle (Sec. 2.2), proton and deuteron (Sec. 2.3), and neutron (Sec. 2.4) measurements were iteratively employed to improve the model. The development of a detailed model facilitated data analysis, but also enabled investigations of potential detector reconfigurations "in software" in order to test whether or not ideas had merit. A variety of configurations including different types of grooving, different optical-coupling media between the GS20 and the MAPMT, and different reflective coatings and degrees of polishing were investigated. An example of a detector configuration that was more straightforward to investigate with the GEANT4 model than in reality was the creation of a detector with 64 individual GS20 scintillators corresponding exactly to the MAPMT pixels, each with different degrees of polishing and each with the edges coated with reflective paint. The simulation has also been used to predict detector response to γ-rays and neutrons with energies up to 100 MeV, common backgrounds at spallation facilities.

2.5.3 Electronic crosstalk

One of the disadvantages of the compact nature of a MAPMT is electronic crosstalk. Scintillation photons reaching the photocathode in one pixel can induce a signal in neighboring pixels. This can be due to photoelectrons reaching a neighboring dynode, electrons in one dynode chain deviating during the multiplication process and starting a new avalanche in a neighboring dynode chain, or inter-pixel capacitance leading to AC coupling between anodes. The amount of electronic crosstalk depends upon the location on the photocathode that the primary photoelectron is released. Intuitively, the closer to the edge of the photocathode that a photoelectron is produced, the higher the level of induced electronic crosstalk in the neighboring pixel [52].

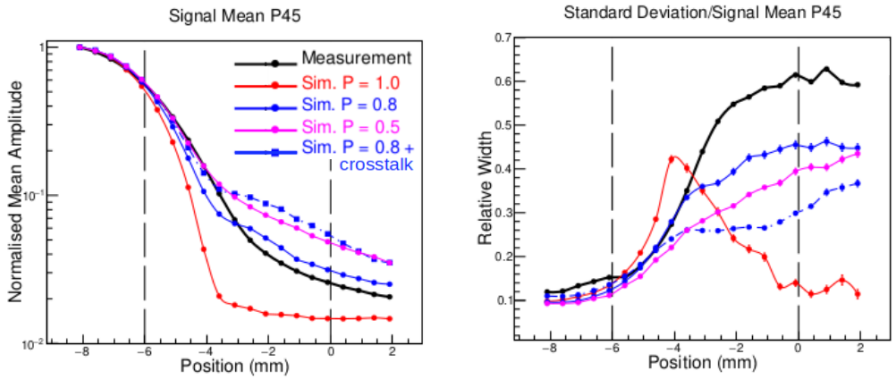

Figure 2.5: Proton scan considering GS20 polish and electronic crosstalk. Measured data (black dots and line) and GEANT4 simulations (colors) for a vertical scan of P45 through the proton beam. The dashed vertical bars represent pixel boundaries. The beam is at the center of P45 at position −9 mm, at the boundary between P45 and P37 at position −6 mm, and at the center of P37 at position −3 mm. Degrees of polish for the GS20 surfaces and a 3% level of electronic crosstalk are considered.

To reproduce measured spectra precisely, the simulation also needs to account for the electronic crosstalk that occurs in a MAPMT. Figure 2.5 shows data from a proton-beam scan as the beam is stepped vertically from the center of P45 to the center of P37 together with results of GEANT4 simulations for varying levels of GS20 surface polish with and without a 3% correction for electronic crosstalk. Clearly, both the level of polish and the level of electronic crosstalk have the same effect on the GEANT4 simulation, resulting in more signal being registered in the adjacent pixel.

Chapter 3

Data analysis

3.1 Tools

Analysis of the data was performed using the `ROOT` [42, 43] data-analysis framework and the `Python`-based [53] `pandas` [54] and `SciPy` [55] tools. Early `ROOT` code was gradually converted to `Python` for a more streamlined analysis. Measured datasets were read into the `pandas` DataFrame structure. DataFrames can be thought of as two-dimensional spreadsheets that can contain different datatypes. They allow easy indexing and slicing of datasets and provide powerful analysis methods. DataFrames were stored in the compact, binary, `Python`-specific `pickle` format for the fast loading of data. `Matplotlib` [56] and `seaborn` [57] packages provided the plotting functions. Illustrations and visual improvements to the plots were done with the open-source vector graphics software `Inkscape` [58].

3.2 Pedestal correction and gain matching of ADC spectra

In order to compare ADC spectra obtained with different pixels, pedestal corrections and gain matching must first be applied to the data. The pedestal corresponds to the zero value of the ADC connected to a given pixel. The gain corresponds to the size of the ADC signal. In general, each pixel will have a unique pedestal and a unique gain, so that given the exact same irradiation conditions, no two pixels will display the same spectra. Pedestals may be measured by triggering on one pixel and examining the signal in pixels not corresponding to the trigger. Gains may be established by systematically exposing the pixels to a constant source of irradiation. Figure 3.1 illustrates the overall procedure for three pixels (red, blue, green) with different gains and different pedestals. The original spectra are shown in the top panel. For each pixel, the location of the pedestal is determined, and a software correction

is applied to the data to shift the pedestals to the same location in the ADC (panel 2). Then, the means of the distributions corresponding to the constant source of irradiation (x_1, x_2, x_3) are determined using Gaussian fit functions (panel 3). Because the source of irradiation was constant, the relationship between the fitted peak means allows for the gain of each pixel to be matched in software (bottom panel).

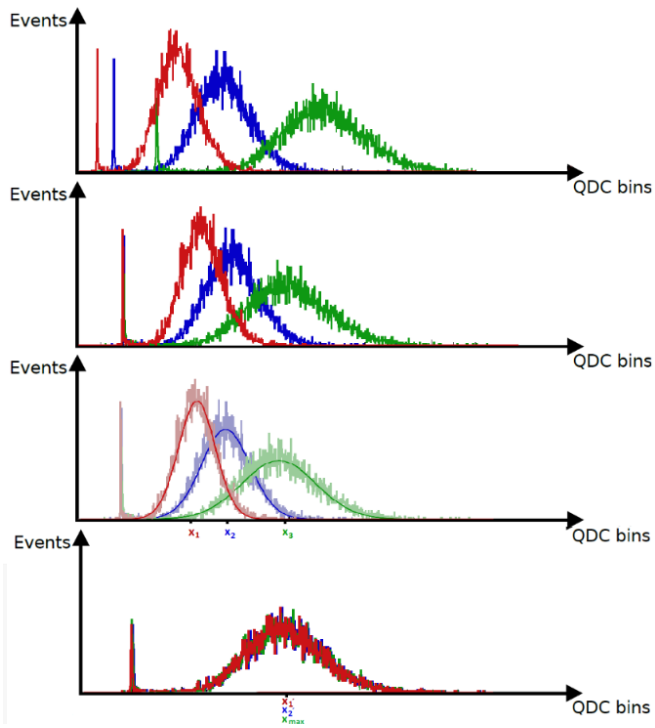

Figure 3.1: Pedestal correction and gain-matching procedure. The sharp spikes to the left correspond to the pedestals, while the broad bumps to the right correspond to the signals. Uncorrected, unmatched spectra (top). Pedestal-corrected, unmatched spectra (panel 2). Fitted functions identifying relative gains (panel 3). Pedestal-corrected, gain-matched spectra (bottom). Figure from [59], reproduced with the permission of the author.

A visualization of the gains for each MAPMT pixel resulted in a color-coded 8×8 gain map which illustrated which pixels produced larger signals if the source of irradiation was held constant, Fig. 3.2. The pixel gains have been normalized so that the pixel with the largest gain has been labeled 100. In general, the gains of the pixels were very sensitive to the source of irradiation chosen, and it was quickly determined that every investigation required a dedicated mapping of the relative gains of pixels using the particle beam in question. In the left panel, the unique gain map for the MAPMT in question supplied by Hamamatsu is shown. It was obtained using a tungsten lamp with a blue filter directly illuminating the MAPMT. In the right panel, a gain map measured with a low-flux, collimated, continuous, 3 mm FWHM thermal-neutron beam directed at pixel centers em-

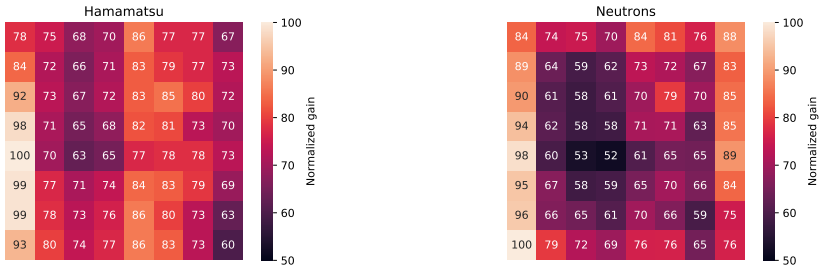

(a) Hamamatsu, tungsten lamp (blue filter)

(b) Thermal-neutron beam

Figure 3.2: Normalized gain maps. Tungsten lamp with a blue filter, no scintillator (a, left). Central-pixel irradiations of GS20 scintillator using a 3 mm FWHM thermal-neutron beam (b, right). The lighter the color the higher the gain.

ploying a dry-fitted 1 mm GS20 sheet is shown. The former may most closely represent the relative, pixel-to-pixel gain variations of the MAPMT. The latter is a more realistic convolution of the relative pixel-gain variations together with effects due to nonuniformities in the photocathode, nonuniformities in the scintillator, fast-scintillation pulses, and optical-scintillation photon transport through the apparatus, to name a few. In all of the results presented in Papers II–IV, gain maps were measured *in situ* using the particle beam in question and gain corrections were performed using these gain maps.

3.3 Scintillation-light sharing between pixels

Figure 3.3 presents a combination of proton data (Paper III) and GEANT4 simulation (Paper V) to illustrate the concept of signal division across pixels. Here, the proton beam is stepped towards the boundary between adjacent pixels. When the proton beam is located at the center of P38 (top panel), most of the scintillation light is registered in P38. Stepping the proton beam closer to the boundary between pixels (panels 2 and 3) results in more and more of the scintillation light reaching into P37, while the majority is still registered in P38. Finally, at the boundary between P37 and P38 (bottom panel), the signal division is close to 50/50. In the vicinity of pixel boundaries and especially near corners, the size of the scintillation-light cone can lead to a substantial amount of charge produced in pixels adjacent to the pixel corresponding to the event.

Regardless of the source of irradiation, the fraction of the scintillation light collected by a given pixel is highly dependent upon where the scintillation light is produced in relation to the pixel grid. Geometry correctly predicts that the signal amplitude is largest when the scintillation light is produced at the center of a pixel. When the scintillation light is produced at the vertical or horizontal boundary between pixels, $\sim$50% of the light registers

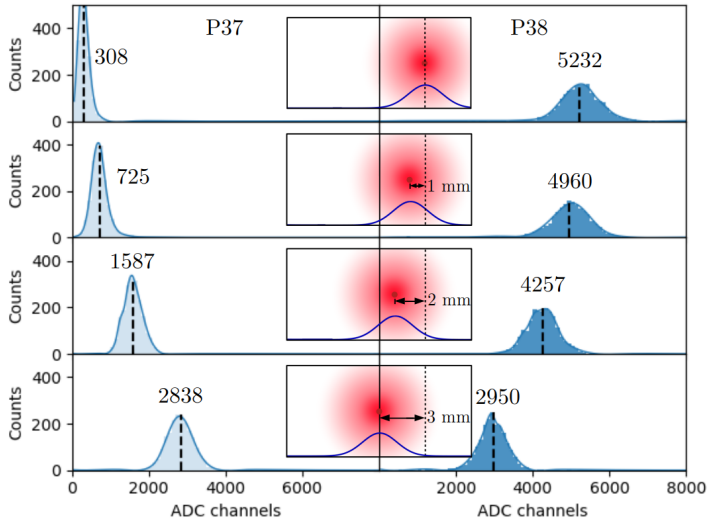

Figure 3.3: Measured and simulated proton-beam boundary scan leading to signal division across adjacent pixels. The vertical line in the center of the figure represents the boundary between P37 (left) and P38 (right). Incident $\sim$100 µm diameter proton beams (dark red dots, not to scale) strike the SoNDe module at four locations (one per panel) corresponding to a horizontal scan in 1 mm steps from the center of P38 to the boundary between P37 and P38. The fuzzy red circles correspond to the GEANT4-simulated 2D scintillation-photon yields ($\sim$2 mm FWHM) at the MAPMT photocathode. The Gaussian distributions at the bases of the insets correspond to the X-projections of the light yields. The shaded histograms correspond to the measured, pedestal- and gain-corrected charge distributions (P37, light blue, left column; P38 dark blue, right column.

in each pixel and when the scintillation light is produced at the corner of a pixel, $\sim$25% of the light registers in each of the four bounding pixels. That said, in the region between the center of the pixel and the pixel edges, the light collection drops in a very non-linear fashion. As an example, Fig. 3.4 (Paper II) shows the charge distributions obtained from a horizontal scan in 1 mm steps of the 1 mm FWHM α-particle beam across the vertical boundary between P37 and P36 from position A to position F, see the inset to panel 2. The curves shown are splines fitted to the distributions. When the beam is located at A, the scintillation light is collected overwhelmingly by P37. When the beam is located 1 mm closer to the vertical boundary at B, a small amount of scintillation light is collected by adjacent P36, but the majority is still collected by P37. When the beam is located $\sim$1 mm from the vertical boundary at C, $\sim$30% of the scintillation light is collected by adjacent P36. And finally, when the beam is located very close to the boundary, the scintillation light is shared roughly equal between P37 and P36.

Studies of the nature of the scintillation-light sharing between adjacent pixels as a function of the distance from the pixel edge or pixel corner were facilitated by the measurements using the highly focused beams of protons and deuterons. As an example, Fig. 3.5 (Paper III) shows the results obtained from a horizontal scan of the SoNDe module through the deuteron beam across the vertical boundary between P37 and P38. Recall the the distributions shown in Fig. 3.4. In this figure, the data points are the means of the charge distributions

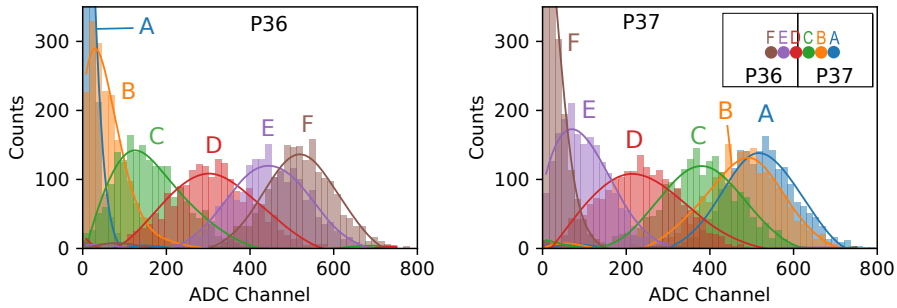

Figure 3.4: α-particle spectra from a boundary scan. Pedestal- and gain-corrected ADC spectra measured in pixels P36 and P37 as the $\sim$1 mm FWHM α-particle beam was scanned across the vertical boundary between pixels in 1 mm steps. The inset in panel 2 shows the irradiation positions.

corresponding to the scintillation-light yields for the different deuteron-irradiation locations. The non-linearity of the falloff of the registered scintillation-light yield as the point of irradiation moves away from the center of the pixel is evident, as is the roughly constant behavior of the sum of the total light yield. In fact, the summed distribution is slightly convex and centered at the boundary between the pixels. This may be explained by the outscattering of scintillation photons to pixels other than P37 and P38. While scintillation light produced at the center of a pixel is collected predominantly by the pixel, a small portion can scatter into adjacent unconsidered pixels. Similarly, scintillation light produced at the boundary between two pixels is collected predominantly by both the pixels, with thus a smaller proportion is able to scatter into adjacent unconsidered pixels. The curves shown are spline fits to GEANT4 simulations (Paper V) of the scintillation-light yield performed for each point of irradiation. The simulations do a reasonable job of explaining the qualitative behavior of the scintillation-light yield, but struggle to reproduce the light-loss gradient in the off-central pixel regions 0.5–2.0 mm from the center of the pixel.

The light-loss gradient in the off-central pixel regions is well illustrated in Fig. 3.6 (Paper IV). Here, a thermal-neutron beam has been employed to form the light-sharing ratio (P33 – P34)/(P33 + P34) from the mean positions of the charge distributions (similar to those illustrated in Fig. 3.5, data points) as a function of neutron-beam irradiation location. By plotting the results in this fashion, the difference between the data and the simulation is emphasized, showing clearly that the current GEANT4 model did not reproduce the light-loss gradient in the off-central pixel regions 0.5–2.0 mm from the center of the pixel. Inclusion of the crosstalk model detailed in Sec. 2.5.3 at the 5% level enables the GEANT4 model to better address the behavior of the charge distributions in the shoulder region.

Detailed studies of the hit multiplicity M as a function of the beam-spot location were also performed. A hit occurred whenever the amplitude of the signal in a pixel exceeded threshold. Increasing the pixel threshold favors the detection of events leaving a large sig-

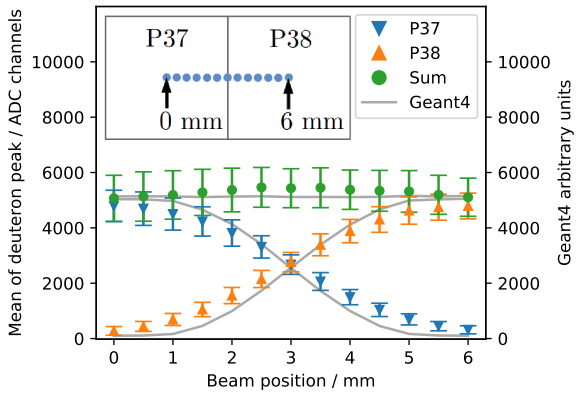

Figure 3.5: Mean scintillation-light yields from a deuteron boundary scan. Means of Gaussian-fitted, pedestal- and gain-corrected charge distributions measured in P37 and P38 as the SoNDe module was scanned horizontally through the $\sim$100µm diameter deuteron beam in 0.5 mm steps. The inset shows the irradiation positions. The error bars correspond to $\pm 1\sigma$ of the fitted functions.

nal in a single pixel ($M = 1$). It also hinders the detection of higher multiplicity events ($M > 1$), as signal division across multiple pixels can lead to none of the pixels receiving a signal large enough to exceed threshold. As previously discussed, signal division occurs most often when the edges and corners of pixels are irradiated. Thus, a high threshold leads to the detector producing a dataset that is predominantly $M = 1$ at the cost of creating dead areas near the edges and corners of the pixels which are not capable of registering events. In contrast, a low threshold leads to the detector producing a dataset that is predominantly $M > 1$ at the cost of potentially creating large areas near the edges and corners of the pixels which are not capable of localizing events with sufficient precision. A lower threshold also results in more background in the dataset. Figure 3.7 (Paper III) shows the spatial distributions of hit multiplicities for P37 (and nearest neighbors) to a 26 $\times$26 grid of proton-beam irradiations performed using a stepsize of 0.5 mm in X and Y for a relatively low ADC threshold of 600 channels. This threshold corresponds to 8% of the mean of the pixel-centered 2.5 MeV full-deposition proton peak. $M = 1$ events are detected in a region within $\sim$1 mm of the center of P37. $M = 2$, 3, and 4 events are all confined to regions of 5 mm or smaller. Raising the threshold increases the size of the region corresponding to $M = 1$ events at the expense of decreasing the sizes of the regions corresponding to $M = 2$, 3, and 4 events. Increasing the threshold further and further will result in dead regions appearing first in the corners and then spreading along the horizontal and vertical boundaries between the pixels.

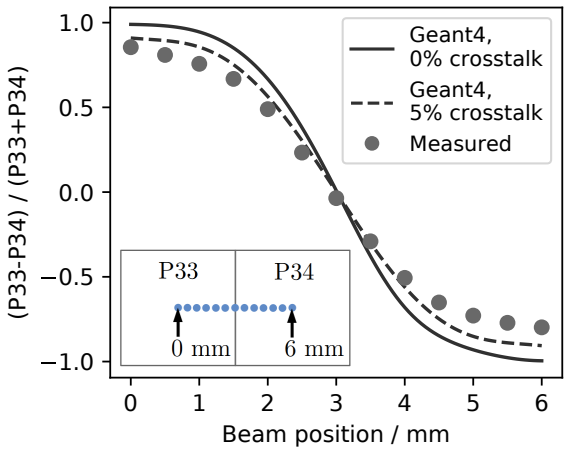

Figure 3.6: Light-sharing ratio formed from the Gaussian-fitted means of the pedestal- and gain-corrected charge distributions measured in P33 and P34 as the SoNDe module was scanned horizontally through a 1 mm FWHM thermal-neutron beam in 0.5 mm steps. The inset shows the irradiation positions. Uncertainties are smaller than the points and lines.

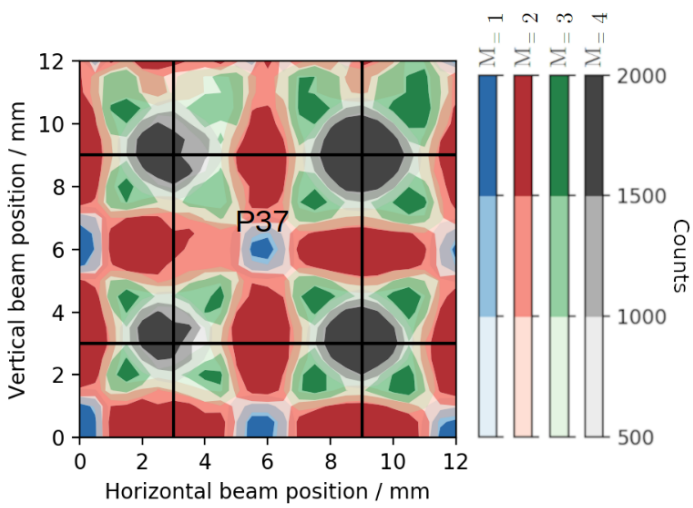

Figure 3.7: Proton-beam multiplicity map. Distributions for a $\sim$100 µm diameter proton-beam scan of P37 and neighbors in 0.5 mm steps. The threshold is set to 600 ADC channels. Blue, red, green, and gray indicate regions dominated by events of $M = 1$, 2, 3, and 4 (see key). The darker the shade of the color, the greater the number of events.

The multiplicity distributions are highly dependent on the threshold setting. Figure 3.8 presents the results of a study of the fraction of thermal-neutron events displaying a particular multiplicity as a function of applied threshold (Paper IV). As the curves corresponding to the various M values all have clear maxima, a threshold may be selected to result in the majority of events in the dataset having a given M. As an illustration, a threshold

corresponding to 50% of the thermal-neutron full-deposition peak (4545 ADC channels) will result in a dataset with ∼78% $M = 1$, ∼4% $M = 2$, and a negligible number of $M = 3, 4$ events. This relatively high threshold will result in ∼18% of the events not exceeding threshold in any pixel and being lost. In contrast, a threshold corresponding to 15% of the thermal-neutron full-deposition peak (1360 ADC channels) will result a loss of ∼2% of the events, and a dataset with ∼22% $M = 1$ and ∼76% $2 \leq M \leq 4$ events. Most importantly, all the surviving events may be localized to ∼5 mm, within the 6 mm experimental design specification for the operation of a SoNDe module at the SKADI instrument at ESS.

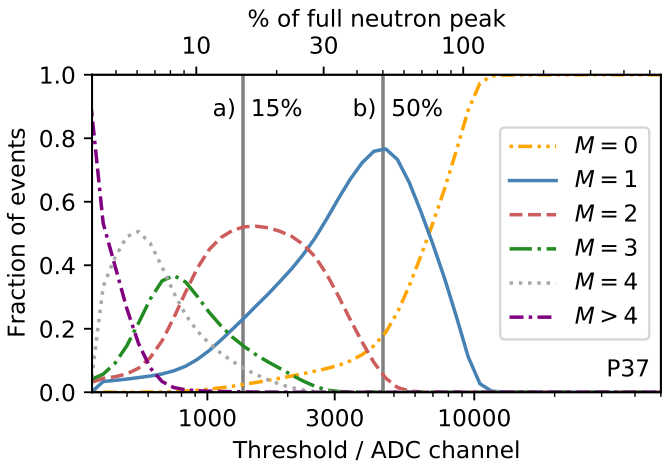

Figure 3.8: Event multiplicity as a function of applied threshold. The fraction of events registered in P37 as a function of threshold applied to all pixels for a scan of the 1 mm FWHM diameter 2.0 Å thermal-neutron beam incident on P37 and adjacent pixels. The vertical lines at 15% and 50% of the neutron full-deposition peak correspond to 1360 and 4545 ADC channels, respectively.

Chapter 4

Results and outlook

4.1 Results

In this thesis, the "as-built" response of a SoNDe module to incident radiation has been mapped and a broad database of results has been established. In the process, five scientific publications have been produced (Papers I–V), with the thesis author being primary on three of the five, see Part II of this document. Each Paper represents a piece of the puzzle that is SoNDe, and the interested reader is directed to the individual papers for specific details. With each Paper came a better understanding of the behavior of the detector. The complementary nature of the sub-projects has resulted in a global understanding of the device that is larger than the sum of the individual investigations. Here, the most important results within the context of the entire project are presented. The following goals were attained:

1. beams of thermal neutrons, α-particles, protons and deuterons were used to map the response of the device to different types of radiation. In the process, it was determined that gain matching is optimally performed using the beams in question.

2. methods for constraining the scintillation signal to a single pixel corresponding to the $M = 1$ mode of operation envisioned for ESS were investigated. Here it was determined that grooving the scintillator was unnecessary, that dry fitting the scintillator to the MAPMT was sufficient, and that reflective coatings were not needed.

3. the "ideal" threshold that maximizes the number of single-pixel events was determined. The surprisingly straightforward algorithm involves locating the mean channel of the full-deposition peak for each pixel and ensures $\sim$80% $M = 1$ data. In the process, events are localized to within $6 \times 6\,\mathrm{mm}^2$.

4. threshold-dependent studies of the position-sensitive response of the device with a precision of better than 1 mm for events triggering multiple pixels was completed. This allowed for the identification of regions of acceptance where $M > 1$ events can be localized to better than 6 mm. This can in principle increase the geometric acceptance of the SoNDe detector while maintaining the critical SKADI instrument design requirement of 6 mm position-reconstruction accuracy, at the cost of increasing the sensitivity of the device to γ-ray background.

In the process of realizing the project goals, several milestones were realized. While these milestones were unrelated to thesis benchmarks, each represented a clear step forward towards the development of a working, well-understood device. The following milestones were achieved:

1. a precision GEANT4 model of the detector on the level of individual scintillation photons was developed. This model facilitates detailed data interpretation and the testing of new detector configurations "in software" and will greatly facilitate upcoming commissioning of the SoNDe detector at ESS.
2. the functionality of the dedicated SoNDe electronics was confirmed using industry-standard VME electronics, and the SoNDe electronics were successfully employed independently in both ACS and TOF modes.
3. the ESS software for event formation (EFU) and visualization tool `Daquiri` were successfully used for the first time with a SoNDe module.
4. a flexible control system, MAPMT Scanner GUI, was developed to precisely control multiple DAQs for data readout and setups of stepping motors used to translate the SoNDe module through a beam (or a beam across the SoNDe module).

In closing, it has been demonstrated that the SoNDe-module concept is a highly functioning substitute for ^{3}He-based thermal-neutron detector technology that meets the requirements for the SKADI instrument at ESS.

4.2 Outlook

While much has been accomplished, tasks remain. The following proposed investigations are intended to take the development of the device to the next level, but are beyond the scope of this thesis.

1. surface finish for both the GS20 and the MAPMT window contributes to signal broadening in the same fashion as electronic crosstalk. Further studies are needed

to decouple the phenomena. Precise knowledge of the mechanisms leading to signal broadening are essential to the $M > 1$ operation of the SoNDe detector.

2. GS20 uniformity has been assumed throughout this thesis. First measurements of the level of uniformity have commenced using a highly focused deuteron beam and Nuclear-Reaction Analysis (NRA) and Particle-Induced X-ray Emission (PIXE) techniques. NRA may be used to determine the uniformity of the ^{6}Li enhancement of the GS20. PIXE may be used to determine the uniformity of the Ce content. Preliminary results are anticipated in the near future.

3. the datasets obtained during this thesis can facilitate the determination of Birks parameter for GS20. Scintillation-light yields for the proton and deuteron beams can likely be extrapolated to triton beams. Scintillation-light yields for α-particle beams and thermal-neutron beams can also facilitate the determination of the scintillation-light yield for triton beams. Measured scintillation-light yields for electrons are desirable. Precise knowledge of Birks parameter for GS20 will improve the precision of the simulation of the γ-ray response of GS20, of critical importance to backgrounds and operating thresholds at ESS.

4. advances in MAPMT technology have occurred, and Hamamatsu now provides model H13700 with $3{\times}3\,\mathrm{mm}^2$ pixels. Further study is warranted to determine if the behavior of the newer MAPMT with the smaller pixels emulates the behavior of the older MAPMT with the larger pixels, or has the further miniaturization affected the behavior in some manner?

5. substantial effort has been expended to define a mode of operation for the SoNDe module where data is predominantly $M = 1$ so that the position resolution is restricted to roughly the size of a MAPMT pixel. By purposefully spreading the scintillation light with a diffuser as in an Anger camera [60, 61], the position resolution for the scintillation could be improved to sub-pixel resolutions on the $\sim$1 mm level [61]. The tradeoff is in reduced DAQ speed and increased instrumentation costs.

6. feeding the SoNDe GEANT4 model with "pre-cooked", well-understood SANS distributions with and without known γ-ray backgrounds would allow investigation of the potential *in situ* behavior of the SoNDe module in both $M = 1$ (higher threshold) and $M > 1$ (lower threshold) modes in software. Exploiting the extended knowledge of the Birks parameter (see above), the effect of the increased γ-ray sensitivity at lower threshold on the data could be studied.

Acknowledgements

Home office, Malmö, Sweden 2020-11-09

I can't really believe that 4.5 years have passed and the PhD time is coming to an end. It's been a truly amazing time and I've gotten to meet a lot of amazing people that I'm thankful to, more than can be listed here but I'll try!

First and foremost I must thank Kevin. If every PhD student could have half as good a supervisor as you have been I think we'd have, well too many good PhDs out there so that wouldn't be good for me now that I'm looking for postdocs..! But seriously though, deepest of thanks for all you've taught and for your door that's always been open. From my first completely over-scribbled pages that met your red marker during my Master, to now handing in my PhD thesis. I owe a big thanks to my co-supervisor Hanno as well, your help has been invaluable and I bring many of the methods you've taught me with me.

At the division I've shared many good times both on and off work. Nata and Pico, good (adventurous) times are guaranteed when you two are around, also many thanks for your help with proof-reading this thesis. Nicholai, my trusty companion since we both were summer students at ESS, it's a pleasure working (and hanging out) with you, best of luck for your remaining PhD time. Big thanks to Kristina for your support and advice! Thank you Ulrika for helping me keep my head straight in stressful times. Mikael, Per, Jan, Rob, Markus – thanks for all and hope to collaborate some more in the future. Playing with the accelerator with you all was one of my favourite parts of the PhD. Markus our lunch guru, thanks for being such a positive influence all the time and dreaming away about skiing was always a welcome little escape. Thank you FraMe for your pedagogical ways and support (and pizza!). Thank you Julius for all you taught me in the beginning of my PhD and your thesis that I might have looked at once or twice (or 100 times). Thank you Göran for your support and to Dirk for all you've taught. Thanks Joachim for your encouragements and advice as well as fun discussions about anything under the sun. For administrative help and smiles that spread around you, thank you Anneli, Yulia, Katarina and Jane. Thanks to all the lovely people at Glasgow University, especially John, Laura, Ken, Ramsey, Rachel,

and Bjorn. John has offered a tremendous amount of help with simulations, experiments, writing, and some good stories over beers, thank you! It's been nice to share the PhD journey with you Laura, thanks for all the good times. Ramsey, the man with many names. I have so fond memories of us pulling our hair through late evenings in the lab or last-minute presentation preparations that were still fun to do together. Thanks for your help, lessons and a good friendship.

To all my colleagues at ESS many thanks for great times and all I've learned. Richard and Kelly, you've been a big help and your support has been very much appreciated. Thank you Morten for always having a solution at hand when it comes to software issued I run into. Same goes to you Martin, good luck at your new work!

Thanks to all the great people in the SoNDe collaboration. Special thanks to Sebastian, Ralf, Codin, Arne and Sylvain. It's been a good 4,5 years and I hope we'll meet more in future projects.

Isabel and Saima at IFE, it was a pleasure coming to do measurements there with your help and support, thank you.

To the people I haven't directly worked with but who have been a valuable counter-weight when research challenges could seem overwhelming – thank you Hussam, Renata, Guillaume (finally learned to spell your name!), Dani, Oscar, Anton, Alex, Jason, Yulia, Eszter, Milan, Nataša, Pearl, and Vero. Thanks for nice lunches and fun discussions with the nano group! To the master students who have joined me on my ventures and contributed with ideas, work, and many laughs – thank you Backis, Vendula, Rasmus, Javier, and Amanda. Special thanks to Amanda who've had to continue dealing with discussions with me from her position at Hamamatsu. To the home crew, who've helped keep my energy levels high, thank you Anton, Teo, Dennis, Helena, Victorya, Anders, Malcolm, and Viktor (I've lived with quite a few last years now that I list you hehe!). Jessica you have helped, supported and inspired me and I'm very grateful for meeting you. Thank you Fredrik and Elin for support through surprise breakfasts, old food, games, and laughs. I feel I can always rely on you.

Thank you Sven for creating a world of wonder, creativity and inventiveness that stuck with me and for letting be borrow your "gubbe" for the cover of the thesis!

For their endless support, encouragements, and love I thank my family – mom, dad, Hilda, Hanna, Annette and Thomas.

Thank you,

Emil

Bibliography

[1] The European Spallation Source (ESS). Lund, Sweden: European Spallation Source ERIC, https://europeanspallationsource.se/.

[2] S. Peggs et al. ESS Technical Design Report. 2013.

[3] M. Lindroos, S. Bousson, R. Calaga, et al. The European spallation source. In *Nucl. Instr. Meth. Phys. Res. B*, volume 269, pages 3258–3260. North-Holland, 12 2011.

[4] Roland Garoby, H. Danared, I. Alonso, et al. The European Spallation Source Design, 1 2018.

[5] Richard T. Kouzes. The 3He Supply Problem. Technical report, Pacific Northwest National Laboratory (PNNL), Richland, WA, 5 2009.

[6] Oliver Kirstein, Richard Hall-Wilton, Irina Stefanescu, et al. Neutron Position Sensitive Detectors for the ESS. *Proceedings of Science*, 15-19-September-2014, 11 2014.

[7] Karl Zeitelhack. Search for alternative techniques to helium-3 based detectors for neutron scattering applications. *Neutron News*, 23(4):10–13, 11 2012.

[8] D. A. Shea and D. Morgan. The Helium-3 Shortage: Supply, Demand, and Options for Congress. Technical report, Congressional Research Service, 2010.

[9] Sebastian Jaksch, Ralf Engels, Günter Kemmerling, et al. Cumulative Reports of the SoNDe Project July 2017. Technical report, Jülich Research Centre, 7 2017.

[10] Scintillation detector with a high count rate. Patent no. PCT/EP2015/074 200, 2015.

[11] James chadwick - facts, 2014. http://www.nobelprize.org/nobel_prizes/physics/laureates/1935/chadwick-facts.html Accessed 2020-10-20.

[12] M. Klaus, Ch Haberstroh, H. Quack, Y. Beßler, and M. Butzek. Conceptual design of the liquid hydrogen moderator cooling circuit for the European Spallation Source. In *Physics Procedia*, volume 67, pages 147–152. Elsevier B.V., 1 2015.

[13] Nicholai Mauritzson. Design, construction and characterization of a portable fast-neutron detector. Master's thesis, Lund University, 2017.

[14] Maria Monica Castellanos, Arnold McAuley, and Joseph E. Curtis. Investigating Structure and Dynamics of Proteins in Amorphous Phases Using Neutron Scattering, 1 2017.

[15] K. H. Andersen, D. N. Argyriou, A. J. Jackson, et al. The instrument suite of the European Spallation Source. *Nucl. Instr. Meth. Phys. Res. A*, 957:163402, 3 2020.

[16] S. Jaksch, D. Martin-Rodriguez, A. Ostermann, et al. Concept for a time-of-flight Small Angle Neutron Scattering instrument at the European Spallation Source. *Nuclear Instruments and Methods in Physics Research, Section A: Accelerators, Spectrometers, Detectors and Associated Equipment*, 762:22–30, 10 2014.

[17] The SKADI Diffractometer: Enlarging the Field of Small-Angle Neutron Scattering, 2020, `https://europeanspallationsource.se/instruments/skadi#instrument-description`.

[18] Victor Gavron, Daniela Henzlova, Malcolm Joyce, et al. The IAEA workshop on requirements and potential technologies for replacement of 3He detectors in IAEA safeguards applications. *Journal of Nuclear Materials Management*, 41(2):14–29, 2013.

[19] Glenn F. Knoll. *Radiation detection and measurement*. John Wiley and Sons, 2010.

[20] William R. Leo. *Techniques for nuclear and particle physics experiments: a how-to approch*. Springer science and business media, 1994.

[21] R.J. Ginther and J.H. Schulman. Glass Scintillators. *IRE Trans. Nucl. Sci.*, NS-5(3):92–undefined, 12 1958.

[22] Scintactor, market leading 6-lithium glass bespoke to your application, 2020. `https://scintacor.com/products/6-lithium-glass/`.

[23] A.R. Spowart. Neutron scintillating glasses: Part 1 activation by external charged particles and thermal neutrons, 1976. Nucl. Instr. Meth. Phys. Res. A 135(3):441-453. ISSN 0029-554X. doi:10.1016/0029-554X(76)90057-4.

[24] William R. Leo. *Techniques for Nuclear and Particle Physics Experiments*. Springer Berlin Heidelberg, 1994.

[25] Photomultiplier tube schematic - Wikimedia Commons, 2020, `https://commons.wikimedia.org/wiki/File:PhotoMultiplierTubeAndScintillator.jpg`.

[26] T. Hakamata (Editor). Photomultiplier tubes basics and applications (third edition), 2006. http://www.hamamatsu.com/resources/pdf/etd/PMT_handbook_v3aE.pdf.

[27] Ray Optics Simulation. https://ricktu288.github.io/ray-optics/.

[28] Blair Jamieson and Lori Ann Rebenitsch. Determining the 6Li doped side of a glass scintillator for ultra cold neutrons. *Nucl. Instr. Meth. Phys. Res. A*, 790:6–9, 8 2015.

[29] S Agostinelli, J Allison, and K Amako. Geant4-a simulation toolkit. *Nuclear Instruments and Methods in Physics Research A*, 506:250–303, 2003.

[30] S. Agostinelli, J. Allison, K. Amako, et al. GEANT4 - A simulation toolkit. *Nucl. Instr. Meth. Phys. Res. A*, 506(3):250–303, 7 2003.

[31] J Allison, K Amako, J Apostolakis, et al. Geant4 Developments and Applications. *IEEE TRANSACTIONS ON NUCLEAR SCIENCE*, 53(1), 2006.

[32] John B. Birks. Scintillations from organic crystals: Specific fluorescence and relative response to different radiations. *Proceedings of the Physical Society. Section A*, 64(10):874–877, 10 1951.

[33] John B Birks. *The Theory and Practice of Scintillation Counting*. Pergamon Press, New York, 1964.

[34] F. Gargano, N. Arnaud, A. Yu Barnyakov, et al. Study of H-8500 MaPMT for the FDIRC detector at SuperB. *Nucl. Instr. Meth. Phys. Res. A*, 718:563–565, 2013.

[35] Integrated Detector Electronics AS, 2020, http://ideas.no/.

[36] Heinz Maier-Leibnitz Zentrum. https://mlz-garching.de/englisch/neutron-research/neutron-source.html.

[37] Laboratorie Léon-Nrillouin, 2020, http://www-llb.cea.fr/.

[38] Forschungszentrum Jülich, 2020, https://www.fz-juelich.de/.

[39] Nuclear and Hadron Physics, University of Glasgow, 2020, http://nuclear.gla.ac.uk/.

[40] R.A. Montgomery, E.N. Cowie, M. Hoek, T. Keri, and B. Seitz. Multianode photomultiplier tube studies for imaging applications. *Nucl. Instr. Meth. Phys. Res. A*, 695:326–329, 12 2012.

[41] R.A. Montgomery. Investigation of hamamatsu h8500 phototubes as single photon detectors, 2015. Nucl. Instr. Meth. Phys. Res. A, 790(1):28-41 ISSN 01689002. doi:10.1016/j.nima.2015.03.068.

[42] Rene Brun and Fons Rademakers. ROOT - An object oriented data analysis framework. *Nucl. Instr. Meth. Phys. Res. A*, 389(1-2):81–86, 4 1997.

[43] ROOT Data Analysis Framework, 2020, `https://root.cern.ch`.

[44] Lund Ion Beam Analysis Facility (LIBAF) | Kärnfysik. `http://www.nuclear.lu.se/forskning/tillaempad-kaernfysik/libaf/`.

[45] M. J. Christensen, M. Shetty, J. Nilsson, et al. Software-based data acquisition and processing for neutron detectors at European Spallation Source - Early experience from four detector designs. *Journal of Instrumentation*, 13(11):T11002, 11 2018.

[46] A. H.C. Mukai, M. J. Clarke, M. J. Christensen, et al. Architecture of the data aggregation and streaming system for the European Spallation Source neutron instrument suite. *Journal of Instrumentation*, 13(10):T10001, 10 2018.

[47] IFE, Institute for Energy Technology. `https://ife.no/en/`.

[48] JJ X-ray A/S Neutron Slits product page. `https://www.jjxray.dk/p/ib-c80-air/`.

[49] HeBoSint sintered Boron Nitride Component. `https://www.henze-bnp.com/en/hebosint-boron-nitride-components.php`.

[50] Mirrobor flexible radio protective material neutrophage absorbent neutron. `http://positechnics.fr/index.adml?r=229&f_fam=275&f=267`.

[51] Martin Shetty, Afonso Mukai, and Jonas Nilsson. ess-dmsc/daquiri: brightness-software-deliverable-MS35, 6 2018.

[52] M. Calvi, P. Carniti, L. Cassina, et al. Characterization of the Hamamatsu H12700A-03 and R12699-03 multi-anode photomultiplier tubes. *Journal of Instrumentation*, 10(9):P09021, 9 2015.

[53] Guido Van Rossum and Fred L. Drake. *Python 3 Reference Manual*. CreateSpace, Scotts Valley, CA, 2009.

[54] Jeff Reback, Wes McKinney, jbrockmendel, et al. pandas-dev/pandas: Pandas 1.0.1, 2 2020.

[55] Wes McKinney. Data Structures for Statistical Computing in Python. In *Proceedings of the 9th Python in Science Conference*, pages 56–61. SciPy, 2010.

[56] J. D. Hunter. Matplotlib: A 2d graphics environment. *Computing in Science & Engineering*, 9(3):90–95, 2007.

[57] M. Waskom, O. Botvinnik, J. Ostblom, et al. mwaskom/seaborn: v0.10.0, 1 2020. https://zenodo.org/record/3629446.

[58] Inkscape Project, 2020. https://inkscape.org/.

[59] Amanda Jalgén, Kevin Fissum, and Hanno Perrey. Initial Characterization of a Pixelated Thermal-Neutron Detector. Master's thesis, Lund University, 2017.

[60] Hal O. Anger. Scintillation camera. *Review of Scientific Instruments*, 29(1):27–33, 1 1958.

[61] R. A. Riedel, C. Donahue, T. Visscher, and C. Montcalm. Design and performance of a large area neutron sensitive anger camera. *Nucl. Instr. Meth. Phys. Res. A*, 794:224–233, 7 2015.

Part II

Scientific publications

Author contributions

Contributions are taken from the CRediT authorship contribution statements.

Paper I: Recent Developments SoNDe High-Flux Detector Project

E. Rofors: Investigation, Validation, Writing – review & editing

Paper II: Response of a Li-glass/multi-anode photomultiplier detector to α-particles from ^{241}Am

E. Rofors: Conceptualization, Methodology, Software, Validation, Formal analysis, Investigation, Data curation, Writing - original draft, Writing - review & editing, Visualization

Paper III: Response of a Li-glass/multi-anode photomultiplier detector to focused proton and deuteron beams

E. Rofors: Conceptualization, Methodology, Software, Validation, Formal analysis, Investigation, Data curation, Writing - original draft, Writing - review & editing, Visualization, Project administration

Paper IV: Response of a Li-glass/multi-anode photomultiplier detector to collimated thermal-neutron beams

E. Rofors: Conceptualization, Methodology, Software, Validation, Formal analysis, Investigation, Data Curation, Writing – original draft, Writing – review & editing, Visualization, Project administration

Paper V: Simulation of the Response of the Solid State Neutron Detector for the European Spallation Source

E. Rofors: Methodology, Software, Validation, Investigation, Data Curation, Writing – review & editing

Paper I

Proc. Int. Conf. Neutron Optics (NOP2017)
JPS Conf. Proc. **22**, 011019 (2018)
https://doi.org/10.7566/JPSCP.22.011019

Recent Developments SoNDe High-Flux Detector Project

Sebastian Jaksch[1], Ralf Engels[2], Günter Kemmerling[2], Uwe Clemens[3], Sylvain Désert[4], Hanno Perrey[5,6], Codin Gheorghe[7], Arne Fredriksen[7], Petter Øya[7], Henrich Frielinghaus[1], Kevin Fissum[6], Amanda Jalgén[6], Emil Rofors[6], Kalliopi Kanaki[5], Richard Hall-Wilton[5,8], Ramsey al Jebali[5]

[1]*FZ Jülich GmbH, Jülich Centre for Neutron Science JCNS at Heinz Maier-Leibnitz Zentrum, D-85747 Garching, Germany*
[2]*FZ Jülich GmbH, Jülich Centre for Neutron Science JCNS, D-52428 Jülich, Germany*
[3]*FZ Jülich GmbH, Zentralinstitut für Engineering, Elektronik und Analytik (ZEA-2), D-52428 Jülich, Germany*
[4]*LLB, CEA, CNRS, Universtité Paris-Saclay, CEA Saclay, F-91191 Gif-sur-Yvette, France*
[5]*European Spallation Source ESS ERIC, P.O. Box 176, SE-221 00 Lund, Sweden*
[6]*Division of Nuclear Physics, Lund University, SE-221 00 Lund, Sweden*
[7]*Integrated Detector Electronics AS IDEAS, NO-0484 Oslo, Norway*
[8]*Mid-Sweden University, SE-851 70 Sundsvall, Sweden*

E-mail: s.jaksch@fz-juelich.de

(Received September 6, 2017)

New high-flux and high-brilliance neutron sources demand a higher count-rate capability in neutron detectors. In order to achieve that goal, the Solid-State Neutron Detector (SoNDe) project is developing a scintillation-based neutron detector. It will be capable of fully exploiting the available flux at small-angle neutron scattering (SANS) instruments at high brilliance sources, such as SKADI at the European Spallation Source (ESS). The read-out of the scintillator is based on a pixelized multi-anode PMT (MaPMT), where each pixel is treated separately. In addition to enabling higher achievable count-rates, one of the design goals was to develop a modular and scalable solution that can also be used in other instruments or even contexts, such as for laboratory setups. This has been achieved by combining the complete read-out electronics along with the MaPMT into modules that can be controlled and read-out individually via a network without additional any infrastructure. An overview of the present state of development and current test results is presented, highlighting the results of previously published project reports.

KEYWORDS: detector, neutron, scintillation, scintillator, SANS, reflectometer, neutron instrumentation, neutron detector

1. Introduction

The development of ever brighter and more brilliant neutron sources [1, 2] calls for a concurrent development in detector technology to be able to fully exploit the better sources to capacity. Along high rate capability, other key parameters include position resolution, detection efficiency, low sensitivity to backgrounds, time resolution, ease of use, reliability and maintainability and the accessibility of necessary materials. The detector technology discussed here is based on the requirements of the SANS instrument SKADI [3] to be constructed at the ESS.

In order to address these issues, the SoNDe detector technology has been developed based upon the following design criteria:

- count-rate capability of at least 20 MHz over a 1×1 m^2 detector area, quadrupling the rate capabilities of existing technologies [4]

- Pixel resolution of 3×3 mm^2, and even better by using Anger interpolation
- Neutron-detection efficiency higher than 80% with good γ-discrimination
- ^{3}He independence
- μs time resolution
- Consisting of individual modules, that can operate independently

Achieving these capabilities simultaneously will allow a high-performance neutron detector. Apart from the ability to use this detector in large-scale facilities where count-rate capability is the principal concern, the other design criteria allow for use in different fields, e.g. bench-top laboratory experiments or even mobile applications, such as scanning for fissionable material in shipped goods [5]. Additional background information on the tests described here can be found in the previously published project reports [5].

2. Basic Concept

The basic concept of the SoNDe design is the pixelization of the detector area, both to distribute a high local count-rate over several analogue channels as well as to increase the resulting spatial resolution. This is coupled with the idea of having black-box electronics for the read-out located directly behind the MaPMT to facilitate the read-out. Such a setup facilitates upscaling when larger areas are to be equipped with modules next to each other, which also leads to the requirement, that the electronics be no larger than the preceeding MaPMT in order to allow for a close packaging and therefore avoid dead space between the individual modules. A sketch of the dense packing is shown in Fig. 1.

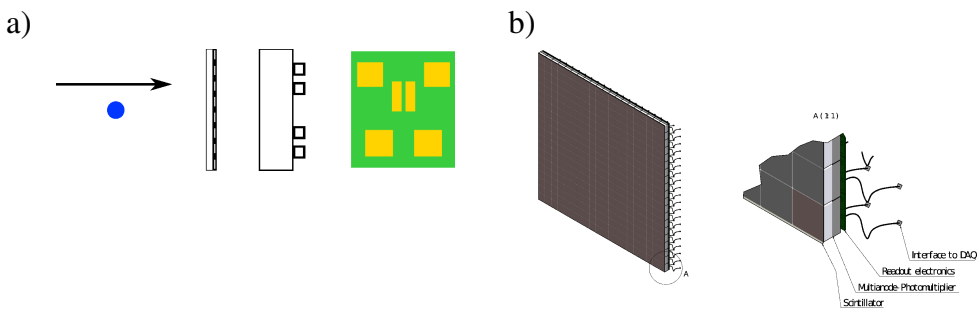

Fig. 1. a) Sketch of the basic concept of a SoNDe detector module. The neutrons (blue) are coming from the left hand side and then impinge on the scintillation material, which is pixelized in this case. The following MaPMT converts the scintillation light into an electronic signal, which is then processed by the read-out electronics. As shown here, all components have an identical footprint, facilitating dense packaging. b) Possible large-scale arrangements

Specific challenges to this design include the prevention of cross-talk between the pixels, which here is inhibited by grooving the scintillator, as well as the packing density of the electronics behind the MaPMT.

As stated earlier, such a setup can be used to create larger surface area detectors as shown in Fig.1 b). It is important that the single modules can be packed as closely as possible. This packaging simultaneously fulfills the requirement of ease of maintenance, as each single module can be serviced individually, while the large-scale setup is not impacted in any major way. This allows also arrangements with different geometries that can be used to improve the performance of neutron-scattering

instruments. One such example might be the arrangement of the modules on a surface of a sphere to cover the entire scattering solid angle without any detector movement.

In the following sections, scintillation material, MaPMT and electronics are discussed individually. A performance overview for the modules will then be presented.

2.1 Components of the detector modules

2.1.1 Scintillator

The scintillator used for the SoNDe modules is a ^{6}Li GS20 glass scintillator purchased from Scintacor®. A general description of such scintillators can be found in Refs. [6–9]. A 6.6% ^{6}Li content leads to a thermal neutron efficiency of ≈75% in a 1 mm thick sample, higher for cold neutrons. With the current setup each neutron-event results in approximately 6600 scintillation photons with a peak wavelength of 390 nm . Approximately 10% of the scintillation light reaches the photocatode corresponding to a MaPMT pixel. The decay time of the light emission is about 60 ns, which does not impede the overall dead-time in our setup. [5].

The γ-sensitivity of GS20 Li-glass is strongly dependent on the γ-energy. For γ-energies of less than 1 MeV, the γ-detection can be suppressed by pulse-height discrimination. Higher γ-energies, suppression is an issue, as these γ cannot be distinguished from neutrons using pulse height discrimination.

In order to assess the cross-talk between pixels we investigated possibilities for a physical separation between the pixels of the scintillator. A method for doing so is attaching the scintillator glass onto a carrier glass and then grooving the scintillator glass with a wafer saw. By doing so, the cross-talk was reduced drastically (see Fig.2). Note that channels 0-7 and 55-63 are at the top and bottom of the MaPMT, which results in a slightly different gain values. Hence, the cross-talk in those channels deviates from the overall average. It also should be noted that the contributions of the other components to the cross-talk, such as the MaPMT and potential electronic cross-talk, are always contained in the results given. Since we only varied the scintillator, these other contributions can be considered to be constant and are not relevant for an optimization of the scintillator.Finally we note that the carrier glass may improve the light yield per pixel by total internal reflection [5].

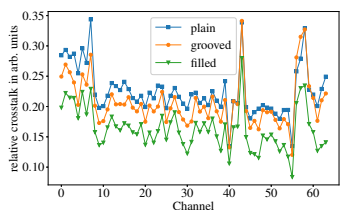

Fig. 2. Relative cross-talk between the MaPMT pixels for a plain scintillator, a grooved scintillator with 200 μm wide grooves and the same grooves filled with reflecting correction fluid. In both cases, the grooves penetrated the entire scintillator (1 mm). The cross-talk is normalized to the amount of neighbours per pixel.

2.1.2 Multi-anode Photomultiplier

The MaPMT used for these detector modules is the Hamamatsu H8500 with 64 channels, each $6 \times 6\,\mathrm{mm}^2$, and a total active area of $52 \times 52\,\mathrm{mm}^2$. The later H12700 series MaPMTs are also technically compatible, as well as the H9500 and their successors with a $3 \times 3\,\mathrm{mm}^2$ pixel size [10]. MaPMTs are vacuum tubes containing a photosensitive cathode and several dynode stages, where multiplication of the initial charge occurs. The choice of these devices over silicon based photomultipliers

(SiPMs) was deliberate, in order to avoid radiation damage by doping the silicon with neutrons. The electronics behind the MaPMT seem to be protected from neutron radiation by the boron in the front glass [5,11]. While the detailed tests in the manuscript focus on the H8500 MaPMTs, the others were only examined in preliminary tests.

2.1.3 Read-out electronics

In order to confine the read-out electronics to the preceding scintillator and MaPMT, they are logically divided into a front-end board and a controller board. The front-end board houses the ASICS used for reading out the MaPMT channels directly. The controller board houses the FPGA module, power supply and an Ethernet port for communication with the back-end computer. A block diagram is shown in Fig.3. This is a direct representation of the schematic given in Fig.1 a).

Depending on the setting, either the analogue event energy or a trigger signal indicating a detected event can be forwarded to the controller board. There, appropriate data treatment (time stamping, channel allocation) is performed and the data are then fed to the Ethernet interface. The module itself can be reached via its own IP address and is thus directly controllable. Programming of the FPGA for further logic operations and the inclusion of external data into the data stream is also possible.

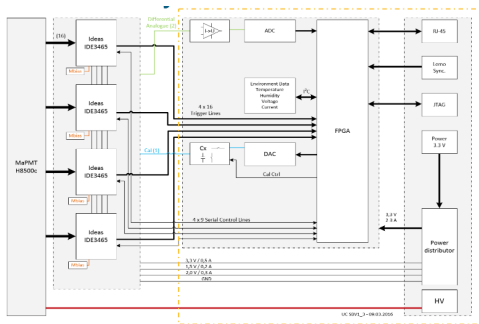

Fig. 3. Schematic diagram of the circuits in the SoNDe detector module. From left to right: The scintillation photons are converted into a current in the MaPMT, which is then registered by the 16 channel ASIC Ideas IDE3465. Here four of them are shown to support a 64 channel photomultiplier.

This setup has the advantage that each single module can be addressed using a computer via standard protocols (TCP and UDP). Therefore, no additional hardware is needed to operate the module, aside from a power source and a HV source for the MaPMT. Operations such as sensitivity calibrations and error messaging can be done online, either with an array of modules connected to a network or with a module directly attached to a PC.

3. Assembled Array

A 3D CAD model and a photograph of a fully assembled SoNDe module are shown in Fig.4. Apart from the Ethernet connection and a power supply for the modules and the MaPMT, there is no additional infrastructure necessary to read out incoming data from the modules. The different settings for the different function modes can be programmed using the PC software. The modules fully support the Ethernet standard and the TCP/UDP protocol and conventional network hardware can be used to connect.

a) b)

Fig. 4. a) Schematic of a fully assembled SoNDe module. The Trenz module (proprietary FPGA module) containing the FPGA (green), the controller board with ETHERNET, JTAG, LEMO and power connectors (blue) and the front-end board, housing the ASICs (yellow) can all be seen. Between the controller and the front-end board there is an aluminum heat sink, which also protects the bonding wires of the ASICs. The HV cable (red) is channeled past the PCBs. b) Photograph of four fully assembled modules configured in a 2×2 detector array. Edgeless packing allows the construction of large scale detectors with a tiled array.

4. Performance

In this section, the performance of the SoNDe detector modules is presented.

4.1 Initial Module

The first module was based on the IDEAS ROSMAP system [5]. Tests at the Laboratoire Léon Brillouin (LLB) were performed. Both the basic feasibility and the radiation hardness of the prototype were in the focus of the investigation.

As a full white beam was available at the beam line G3.2 [12], the flux capabilities of the module could be tested. In order to do so, a fully absorbing slit system was positioned in front of the module and the beam size was increased until the response became non-linear. The corresponding data is shown in Fig.5. The count-rate increases linearly with the irradiated area until 250 kHz, which is the

a) b)

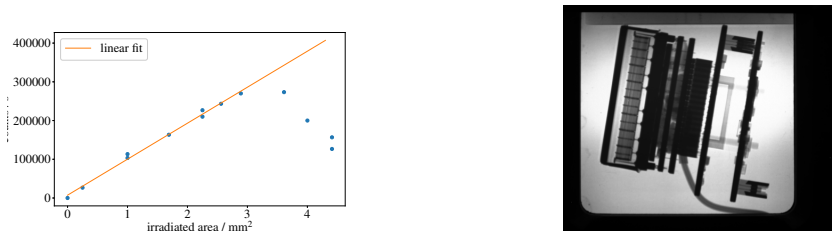

Fig. 5. a) Relation between irradiated area and count-rate. b) Radiograph of the first generation SoNDe Module. It is visible that the boron glass at the front of the MaPMT is nearly intransparent to neutrons. With an additional scintillator in front of the module, the combined shielding effect of the scintillator and the boron glass effectively protect the electronics from radiation damage.

rate-limit for this module. At higher count-rates, double counting below the dead-times occurs. 250 kHz on a single $52 \times 52\,\mathrm{mm}^2$ module correspond to 100 MHz on a full square meter detector. Here, it has to be taken into account that the signal was simply detected and that no data treatment inside the module was performed. Also, for a clear separation between each neutron-event, a buffer-time

between events is usually inserted into the logic of the modules. This was omitted here and trigger settings could only be adjusted manually by increasing the threshold until a sufficient background suppression was reached. Thus, this has to be seen as the maximum achievable count-rate with that setup. This is also illustrated by the fact that the physical dead-time of the scintillator (60 ns) corresponds to a maximum possible count-rate of 16.67 MHz in the same location, which here is alleviated by using a non infinitesimally small surface area, however the hard physical limit is nearly in the same order of magnitude.

In order to test the radiation hardness the module was kept in continuous operation under the maximum achievable neutron flux for 10 days, during that time only one single event upset occurred after nine days. A restart and subsequent electronic test showed that no permanent damage was inflicted upon the module. The module electronics, seem to be inherently stable under high radiation conditions. This is likely due to the fact that direct exposure to the neutron beam is blocked by both the scintillator itself and the subsequent boron glass in the MaPMT. We estimate that between them, they attenuate the neutron flux to less than 1% of its initial value. This effect can also be seen in the radiography image of the module shown in Fig. 5.

4.2 Second-Generation SoNDe module

The second generation module was described in detail in Ref. [5]. The test was performed at the TREFF instrument at Heinz Maier-Leibnitz Zentrum (MLZ), Garching, at a neutron wavelength of 4.7 Å. During these tests, both the performance under actual experimental conditions as well as the status of the software were tested. While the electronics were demonstrated to handle high count-rates with a pulse generator on the benchtop, it was important to make sure that this was also true for statistically distributed pulses generated by the MaPMT. The control software, which will be needed for the ongoing testing, was also tested.

The test beam was tailored by two blinds to yield a vertical stripe of neutrons on the detector. This was done to make sure that in the non-irradiated areas no event could be triggered. This could lead to background in later application of the module. An image of the detected neutron-events on the demonstrator surface is shown in Fig.6. There is no visible saturation. The recorded pulse-height spectrum allows for a clear discrimination between neutron and γ-events.

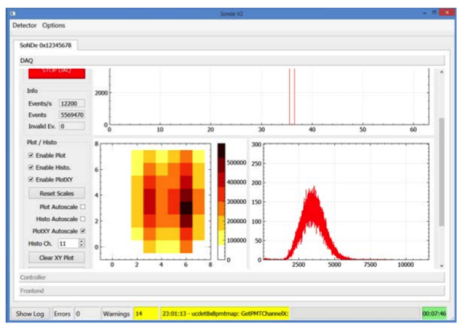

Fig. 6. Screenshot of the SoNDe control software during operation.

All information was visualized and recorded using the control software (screenshot Fig.6). There, distribution of the events across the face of the MaPMT as a function of pixel together with the corresponding pulse-height spectrum is shown. Additionally, each submodule of the 2×2 demonstrator can be accessed via a separate register card. Only one submodule was connected. These tests showed

that the performance of the 2×2 demonstrator under actual experimental conditions achieved the expectations. The integrated flux in the primary beam of the TREFF instrument is $\approx 10^8$ neutrons/s and no saturation effects of any kind are visible. Confirmation of these results by future tests on higher flux instruments is foreseen. The development of SoNDe can now proceed to the upscaling to larger areas.

4.3 Electronic performance

The second-generation SoNDe module was tested with a pulse generator. Dynamic range, maximum count-rate and single-event detection were evaluated [5]. The dynamic range was determined by examining the linearity of the relationship between input charge and ADC signal. The results are shown in Fig.7 a). Between 9.4 and 80 pC, the ADC signal was completely linear as a function of the integrated input charge. Saturation effects become visible above 80 pC, a dynamic range of about one order of magnitude. This linearity allows for a reliable discrimination of the signal.

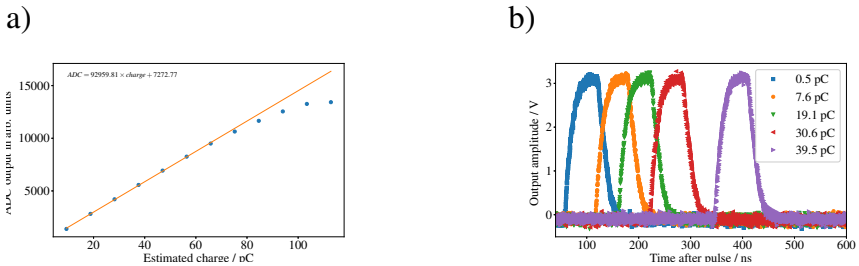

Fig. 7. a) Relationship between integrated input charge and ADC value. b) Time delay between the initial pulse at the input of the module and the resulting digital trigger signal. The time delay varies depending on the pulse charge and the threshold setting.

In order to assess the maximum achievable count-rate, the system was fed with an increasing frequency of pulses from the generator until a loss was observed. While the system exhibited stable behaviour up to 2.22 MHz, at 2.23 MHz some pulses were lost. In the case of statistical pulses, a counting frequency of about 10% is assumed, hence translating the maximum frequency into ≈ 220 kHz for stable operation. Achieving this for a 1 m^2 detector area would translate into 400×220 kHz= 88 MHz as the maximum stable event rate.

Finally, an evaluation of single events revealed that the processing delay through the front-end board was 110 ns for each detected event, completely independent of the irradiated pixel. The charge required to trigger the system rises along with the trigger threshold. The time to trigger the system increases with the threshold. The corresponding behaviour of the trigger signals can be seen in Fig.7. Lower thresholds lead to a faster detection of the signal. This is expected as lower input charges need to be integrated over longer times in order to exceed a given threshold value. Both the fixed delay and the relation between threshold and event charge have to be taken into account for the later time stamping of events. The accuracy of the time stamp delivered by the module is approximately $\pm$150ns.

5. Conclusion

We have presented an overview of the present state of the SoNDe detector technology. The results show that the construction of a high-flux neutron detector with $6 \times 6\,mm^2$ resolution is possible. An upgrade path to $3 \times 3\,mm^2$ resolution has already been identified as feasible. Maximum obtainable

count-rates could exceed 20 MHz per square meter. In terms of maintenance and operation, both the radiation hardness of the single modules as well as their ease of operation has been established. The modular design facilitates any repair and maintenance work in later assemblies.

Acknowledgments

The work on the SoNDe project is funded by the European Union within the Horizon 2020 framework under project number 654124. The financial support by the European Union is gratefully acknowledged. We also gratefully acknowledge beam-time both at Laboratoire Léon Brillouin (LLB) and Heinz Maier-Leibnitz Zentrum (MLZ).

References

[1] S. Peggs, R. Kreier, C. Carlile, R. Miyamoto, A. Påhlsson, M. Trojer, J. G. Weisend, *et al.*, eds., *ESS technical design report*. European Spallation Source, 2013.

[2] O. Kirstein, R. Hall-Wilton, I. Stefanescu, M. Etxegarai, M. Anastasopoulos, K. Fissum, A. Gulyachkina, C. Höglund, M. Imam, K. Kanaki, *et al.*, "Neutron position sensitive detectors for the ess," *arXiv preprint arXiv:1411.6194*, 2014.

[3] S. Jaksch, D. Martin-Rodriguez, A. Ostermann, J. Jestin, S. D. Pinto, W. Bouwman, J. Uher, R. Engels, and H. Frielinghaus, "Concept for a time-of-flight small angle neutron scattering instrument at the european spallation source," *Nuclear Instruments and Methods in Physics Research Section A: Accelerators, Spectrometers, Detectors and Associated Equipment*, vol. 762, pp. 22–30, 2014.

[4] A. Radulescu, N. K. Szekely, and M.-S. Appavou, "Kws-2: Small angle scattering diffractometer," *Journal of large-scale research facilities JLSRF*, vol. 1, p. 29, 2015.

[5] S. Jaksch, R. Engels, G. Kemmerling, C. Gheorghe, P. Pahlsson, S. Désert, and F. Ott, "Cumulative reports of the sonde project july 2017," *arXiv preprint arXiv:1707.08679*, 2017.

[6] F. Firk, G. Slaughter, and R. Ginther, "An improved li6-loaded glass scintillator for neutron detection," *Nuclear Instruments and Methods*, vol. 13, pp. 313–316, 1961.

[7] A. Spowart, "Neutron scintillating glasses: Part 1: Activation by external charged particles and thermal neutrons," *Nuclear Instruments and Methods*, vol. 135, no. 3, pp. 441–453, 1976.

[8] A. Spowart, "Neutron scintillating glasses: Part ii: The effects of temperature on pulse height and conductivity," *Nuclear Instruments and Methods*, vol. 140, no. 1, pp. 19–28, 1977.

[9] E. Fairley and A. Spowart, "Neutron scintillating glasses part iii pulse decay time measurements at room temperature," *Nuclear Instruments and Methods*, vol. 150, no. 2, pp. 159–163, 1978.

[10] . H. P. K.K, "Flat panel type multianode pmt assembly h8500 series / h10966 series," 2011.

[11] M. Andreotti, W. Baldini, R. Calabrese, G. Cibinetto, A. C. Ramusino, C. Dedonato, M. Fiorini, E. Luppi, R. Malaguti, A. Montanari, *et al.*, "Radiation damage effects in silicon photo-multipliers," in *Nuclear Science Symposium and Medical Imaging Conference (NSS/MIC), 2013 IEEE*, pp. 1–4, IEEE, 2013.

[12] A. Menelle, "www-llb.cea.fr/fr-en/pdf/description-g3bis-g32-g5bis-v3.pdf," tech. rep., CEA Saclay, 2011.

Paper II

Nuclear Inst. and Methods in Physics Research, A 929 (2019) 90–96

Contents lists available at ScienceDirect

Nuclear Inst. and Methods in Physics Research, A

journal homepage: www.elsevier.com/locate/nima

Response of a Li-glass/multi-anode photomultiplier detector to α-particles from ^{241}Am

E. Rofors [a], H. Perrey [a,b], R. Al Jebali [b,c], J.R.M. Annand [c], L. Boyd [c], U. Clemens [g], S. Desert [e], R. Engels [f], K.G. Fissum [a,b,*], H. Frielinghaus [f], C. Gheorghe [h], R. Hall-Wilton [b,d], S. Jaksch [f], A. Jalgén [a], K. Kanaki [b], G. Kemmerling [f], V. Maulerova [a], N. Mauritzson [a], R. Montgomery [c], J. Scherzinger [a,b,1], B. Seitz [c]

[a] Division of Nuclear Physics, Lund University, SE-221 00 Lund, Sweden
[b] Detector Group, European Spallation Source ERIC, SE-221 00 Lund, Sweden
[c] SUPA School of Physics and Astronomy, University of Glasgow, Glasgow G12 8QQ, Scotland, UK
[d] Mid-Sweden University, SE-851 70 Sundsvall, Sweden
[e] LLB, CEA, CNRS, Université Paris-Saclay, 91191 Gif-sur-Yvette, France
[f] Jülich Centre for Neutron Science JCNS, Forschungszentrum Jülich, D-52425 Jülich, Germany
[g] Zentrum für Anwendungsentwicklung und Elektronik ZEA-2, Forschungszentrum Jülich, D-52425 Jülich, Germany
[h] Integrated Detector Electronics AS, Gjerdrums vei 19, NO-0484 Oslo, Norway

ARTICLE INFO

Keywords:
SoNDe thermal neutron detector
GS20 scintillating glass
Multi-anode photomultiplier
Position-dependent α-particle response
H12700A

ABSTRACT

The response of a position-sensitive Li-glass scintillator detector to α-particles from a collimated ^{241}Am source scanned across the face of the detector has been measured. Scintillation light was read out by an 8 × 8 pixel multi-anode photomultiplier and the signal amplitude for each pixel has been recorded for every position on a scan. The pixel signal is strongly dependent on position and in general several pixels will register a signal (a hit) above a given threshold. The effect of this threshold on hit multiplicity is studied, with a view to optimize the single-hit efficiency of the detector.

1. Introduction

The European Spallation Source (ESS) [1] will soon commence operations as the most powerful neutron source in the world. Highly efficient, position-sensing neutron detectors are crucial to the scientific mission of ESS. The worldwide shortage of ^{3}He [2–4] has resulted in considerable effort being undertaken to develop new neutron-detector technologies. One such effort is the development of Solid-state Neutron Detectors SoNDe [5–7] for high-flux applications, motivated by the desire for two-dimensional position-sensitive systems for small-angle neutron-scattering experiments [8–17]. The SoNDe concept features individual neutron-detector modules which may be easily configured to instrument essentially any experimental phase space. The specification for the neutron interaction position reconstruction accuracy for the SoNDe technology is 6 mm.

The core components of a SoNDe module are the neutron-sensitive Li-glass scintillator and the pixelated multi-anode photomultiplier tube (MAPMT) used to collect the scintillation light. The response of MAPMTs to scintillation-emulating laser light has been extensively studied [18–26]. Similar Li-glass/MAPMT detectors have been tested with thermal neutrons [27] and a SoNDe detector prototype has been evaluated in a reactor-based thermal-neutron beam [6]. In this paper, we present results obtained for the response of a SoNDe detector prototype to α-particles from a collimated ^{241}Am source scanned across the face of the scintillator. Our goal was to examine methods to optimize the localization of the scintillation signal with a view to optimizing the position resolution of the detector, under constraints imposed by envisioned readout schemes for the detector. We were particularly interested in the behavior of the SoNDe detector prototype at the vertical and horizontal boundaries between the pixels and the corners where four pixels meet.

2. Apparatus

2.1. Collimated α-particle source

Fig. 1 shows a sketch of the assembly used to produce a beam of α-particles. It consisted of a ^{241}Am α-particle source mounted in a 3D-printed holder/collimator assembly.

* Corresponding author at: Division of Nuclear Physics, Lund University, SE-221 00 Lund, Sweden.
E-mail address: kevin.fissum@nuclear.lu.se (K.G. Fissum).
[1] present address: Dipartimento di Fisica, Universit di Pisa, I-56127 Pisa, Italy and INFN Sezione di Pisa, I-56127 Pisa Italy.

https://doi.org/10.1016/j.nima.2019.03.014
Received 29 December 2018; Received in revised form 1 March 2019; Accepted 6 March 2019
Available online 7 March 2019

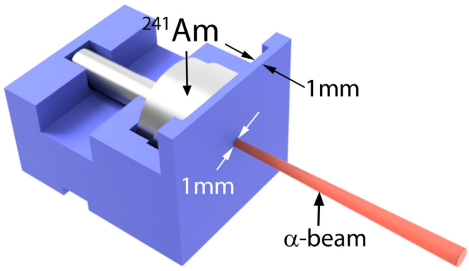

Fig. 1. ^{241}Am α-particle source mounted in the holder/collimator assembly used to define a beam of α-particles. The radioactive source fit sungly in the blue holder/collimator. The assembly shown has a 1 mm thick face plate and a 1 mm diameter hole, resulting in the diverging red beam of α-particles. (For interpretation of the references to color in this figure legend, the reader is referred to the web version of this article.)

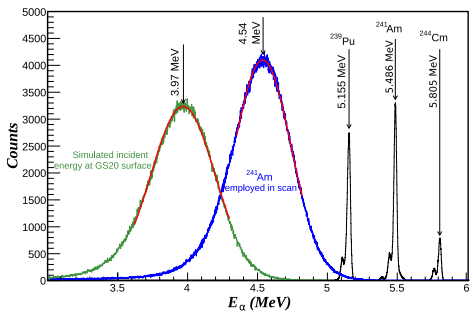

Fig. 2. Uncollimated α-particle spectrum (in vacuum) emitted by the ^{241}Am source employed in the suite of measurements reported on here (broad blue distribution) together with a red fitted Gaussian function (indicating peaking at 4.54 MeV) and a triple α-particle spectrum emitted by a very thin-windowed three-actinide calibration source (sharp black primary peaks at 5.155 MeV, 5.486 MeV, and 5.805 MeV). The spectrum depicted in green is a GEANT4 simulation of the α-particle spectrum incident on the GS20 wafer, peaking at 3.97 MeV. (For interpretation of the references to color in this figure legend, the reader is referred to the web version of this article.)

The α-particle emission energies of ^{241}Am are 5.5 MeV (~85%) and 5.4 MeV (~15%). The gamma-ray background from the subsequent decay of excited states of ^{237}Np has an energy of ~60 keV and has a negligible effect on the α-particle response of the SoNDe detector prototype. The α-particle spectrum from the present source was measured (Fig. 2) using a high-resolution passive-implanted planar silicon (PIPS) detector system in vacuum, where the PIPS detector was calibrated using a three-actinide calibration source. The average energy of the α-particles emitted by the presently employed source was ~4.5 MeV, corresponding to an energy loss of ~1 MeV in the source window.

Holder/collimator assemblies for the ^{241}Am source were 3D-printed from polyactic acid using the fused deposition modeling technique. For our measurements, we used 1 mm thick collimators with either 3 mm (for gain mapping) or 1 mm (for border scanning) diameter apertures, resulting in uniform 3 mm or 1 mm irradiation spots at the upstream face of the scintillator. The distance from the ^{241}Am source to this upstream face was 6 mm of air. GEANT4 simulation showed that the mean α-particle energy at the surface of the GS20 wafer was ~4.0 MeV, in excellent agreement with the results of Ref. [28].

2.2. SoNDe detector prototype

The SoNDe detector prototype investigated in this paper is being developed for large-area arrays to detect thermal to cold neutrons with energies of ≲25 meV. It consists of a 1 mm thick lithium-silicate scintillating glass wafer coupled to a H12700A MAPMT.

2.2.1. Li-glass scintillator

Cerium-activated lithium-silicate glass scintillator GS20 [29–32] purchased from Scintacor [33] was chosen for this application. GS20 has been demonstrated to be an excellent scintillator for the detection of thermal and cold neutrons and arrays of scintillator tiles can be arranged into large area detector systems [8–11,13]. The lithium content is 6.6% by weight, with a 95% ^{6}Li isotopic enhancement, giving a ^{6}Li concentration of 1.58 × 10^{22} atoms/cm^3. ^{6}Li has a thermal-neutron capture cross section of ~940 b at 25 meV, so that a 1 mm thick wafer of GS20 detects ~75% of incident thermal neutrons. The process produces a 2.05 MeV α-particle and a 2.73 MeV triton which have mean ranges of 5.3 μm and 34.7 μm respectively [34] in GS20. Using the present α-particle source, scintillation light was generated overwhelmingly within ~15 μm of the upstream face of the scintillating wafer. The large stopping power of 4.0 MeV α-particles prohibited the use of a reflector on the upstream side of the scintillating wafer. We note that the scintillation light-yield outputs for 1 MeV protons is ~5 times higher than that of 1 MeV α-particles [35]. Thus, after thermal-neutron capture, the triton will produce a factor of ~5 more scintillation light than the α-particle. Tests by van Eijk [36] indicate ~6600 scintillation photons per neutron event with a peak at a wavelength of 390 nm, which corresponds to ~25% of the anthracene benchmark. The sensitivity of GS20 to gamma-rays is energy dependent. A threshold cut will eliminate the low-energy gamma-rays, but higher-energy gamma-rays can produce large pulses if the subsequent electrons (from Compton scattering or pair production) traverse sufficient thickness of GS20.

Our glass wafer was 1 mm thick and 50 mm × 50 mm in area. The glass faces, apart from the edges, were polished and the wafer was fitted to the MAPMT window without any optical coupling medium and held in place with tape along the thin wafer edges. The index of refraction of GS20 is 1.55 at 395 nm. We have assumed that the ^{6}Li distribution in our scintillating wafer was uniform.

2.2.2. Multi-anode photomultiplier tube

The Hamamatsu type H12700A borosilicate glass MAPMT employed in the SoNDe detector prototype is an 8 × 8 pixel device with outer dimensions 52 mm × 52 mm and an active cathode area of 48.5 mm × 48.5 mm, resulting in a packing density of 87%. The bialkali photocathode produces a peak quantum efficiency of ~33% at ~380 nm wavelength, which is well matched to the GS20 scintillation. Compared to its predecessor type H8500 MAPMT, the H12700A MAPMT achieves similar overall gain, but with 10 as opposed to 12 dynode stages. The H12700A MAPMT employed for the present tests had a gain of 2.09 × 10^6 and a dark current of 2.67 nA at an anode–cathode potential of −1000 V. Each of the 64 ~6 × 6 mm^2 pixels in the Hamamatsu H12700A MAPMT has a slightly different gain, which is measured and documented by the supplier. A typical H12700A MAPMT has a factor 2 variation in pixel gain (factor 3 worst case) [37]. The datasheet provided by Hamamatsu for the H12700A MAPMT used in this study had a worst case anode-to-anode gain difference of a factor 1.7. Fig. 3 shows a photograph of the device together with a pixel map.

3. Measurement

The SoNDe detector prototype was irradiated using the collimated beams of α-particles (Section 2.1) where the center of the beam was directed perpendicular to the face of the GS20 wafer. The total flight distance of α-particles through air to the surface of the GS20 wafer was 6 mm (Fig. 1). The downstream face of the source holder/collimator assembly was translated parallel to the surface of the scintillator wafer on

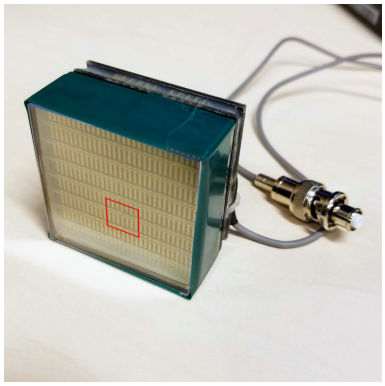

(a) MAPMT with scintillator

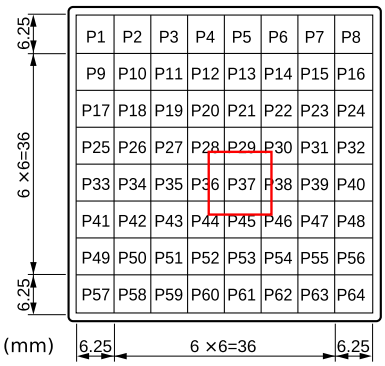

(b) MAPMT pixel map

Fig. 3. The Hamamatsu H12700A MAPMT. 3(a): Photograph of the MAPMT together with the GS20 scintillator wafer. 3(b): Numbering of the 64 MAPMT pixels (front view). Pixel 1 (P1) is located in the top left-hand corner of the MAPMT looking into it from the front. Sketch from Ref. [37]. The red boxes indicate the region of irradiation reported on in detail in this paper. (For interpretation of the references to color in this figure legend, the reader is referred to the web version of this article.)

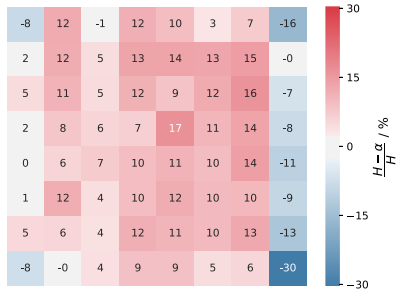

(a) Gain differences, areal

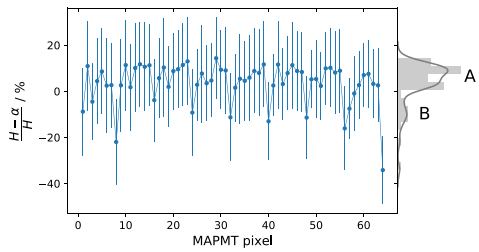

(b) Gain differences, projected

Fig. 4. Differences between the α-scan gain-map and the Hamamatsu gain-map normalized to the Hamamatsu gain-map in percent. 4(a): 2D representation in which the top-left corner corresponds to P1. 4(b): 1D representation of the same as a function of pixel. Error bars are derived from fit widths. The values have been joined with a line to guide the eye. A histogram of the gain differences is projected in gray on the right vertical axis. Cluster A of that histogram corresponds to red pixels in 4(a) while cluster B corresponds to blue pixels. (For interpretation of the references to color in this figure legend, the reader is referred to the web version of this article.)

an XY-coordinate scanner powered by a pair of Thorlabs NRT150 stepping motors [38]. This was programmed to scan a lattice of irradiation points uniformly distributed across the face of the device. The entire assembly was located within a light-tight box and the temperature (~25°), pressure (~101.3 kPa), and humidity (~30%) within the box were logged at the beginning and end of each measurement position. The anode signals from each of the pixels in the MAPMT were recorded using standard NIM and VME electronics. The positive polarity dynode-10 signal was shaped and inverted using an ORTEC 454 NIM timing filter amplifier producing a negative polarity signal with risetime ~5 ns, falltime ~20 ns, and amplitude some tens of mV, which was fed to an ORTEC CF8000 constant-fraction discriminator set to a threshold of −8 mV. The resulting NIM logic pulses with a duration of 150 ns provided a trigger for the data-acquisition system and a gate for the CAEN V792 VME charge-to-digital converters (QDCs) used to record the 64 anode pixel charges. A CAEN V2718 VME-to-PCI optical link bridge was used to sense the presence of a trigger signal and to connect the VMEbus to a Linux PC-based data-acquisition system. The digitized signals were recorded on disk and subsequently processed using ROOT-based software [39]. Data were recorded for ~120 s at each point on a scan, so that in total a scan could take several hours.

4. Results

The gain-calibration datasheet provided by Hamamatsu may be used to correct for non-uniform response. However, previous work [18–23,25] has clearly suggested that mapping of pixel gains is highly dependent upon the irradiation conditions. Since our α-particle beam results in very short (~10 s of ns) pulses of highly localized scintillation light which are in sharp contrast to the steady-state irradiation measurement employed by Hamamatsu, we re-measured the gain-map of our MAPMT *in situ* using the equipment described previously. For each pixel, the 3 mm diameter α-particle collimator was centered on the XY position of the pixel center of the MAPMT photocathode and 2200 α-particle events were recorded. The resulting anode-charge distributions were well fitted with Gaussian functions (average χ^2 per degree of freedom 1.50 with a variance of 0.14) and the means, μ, and standard deviations, σ, were recorded. The largest measured μ-value

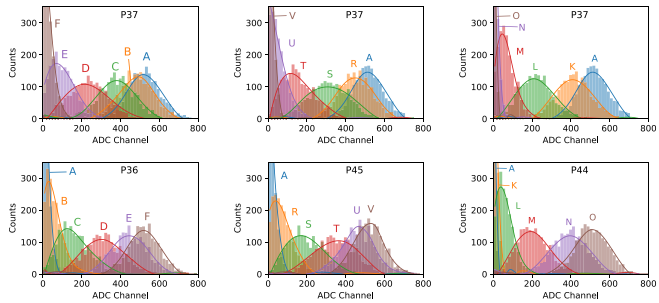

(a) Horizontal scan F ← A (b) Vertical scan A ↓ V (c) Diagonal scan O ↙ A

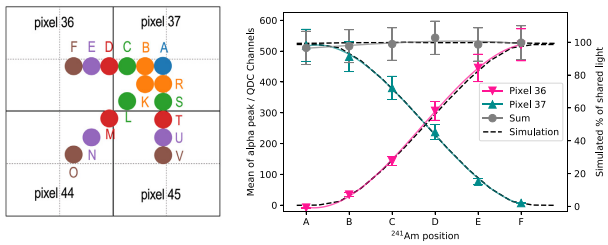

(d) Key (e) Light sharing horizontal scan F ← A

Fig. 5. 5(a)–5(c) Measured charge distributions for four adjacent pixels as the α-particle beam was translated in 1 mm horizontal and vertical steps across the pixel boundaries. (a): horizontal scan from P37 to P36. (b): vertical scan from P37 to P45. (c): diagonal scan from P37 to P44. 5(d): Key. The solid (dashed) black lines indicate the pixel boundaries (centers). 5(e): Gain-corrected means of the collected charge distributions corresponding to 5(a). The curves are splines drawn to guide the eye. Error bars correspond to $\sigma/10$. (For interpretation of the references to color in this figure legend, the reader is referred to the web version of this article.)

(corresponding to the pixel with the highest gain) was normalized to 100. The relative difference between the Hamamatsu gain-map values, H, and the α-scanned gain-map values, α, was calculated as $\frac{H-\alpha}{H}$ on a pixel-by-pixel basis. Fig. 4 shows the results of our gain-map measurement, where the present results show significant differences to the Hamamatsu measurement. General trends in regions of high and low gain agree. Measurements of a sample of 30 H12700A MAPMTs revealed that the window face is not flat and was systematically ∼80 μm lower at the center compared to the edges. The non-uniformity of the air gap between the GS20 and MAPMT window may be a partial cause of the gain discrepancy displayed in Fig. 4, as may reflections at the edges of the GS20 wafer. In the following, we use the present α-scintillation generated gain-map, which in principle will embody non-uniform light-collection effects. Nonetheless, scintillation-light propagation through the SoNDe detector prototype is being studied in a GEANT4-based simulation [40,41] in order to better understand these effects.

Fig. 5 shows the positions of the 1 mm collimated α-particle source employed for the horizontal, vertical, and diagonal XY scans. The positions are labeled A–V and color coded (5(d)). The α-particle pulse-height spectra recorded at each of the scan positions are displayed in 5(a)–5(c) for pixels P36, P37, P44, and P45 which encompass the scan coordinates. The QDC pulse-height distributions have been pedestal subtracted and corrected for non-uniform pixel gain (Fig. 4). It is obvious that the efficiency of scintillation light collection in a single pixel is strongly dependent on the position of the α-particle interaction. The signal amplitude is maximized when light is produced at the center of the pixel. This variation in amplitude with position may be seen more clearly in 5(e), which shows the mean of the pulse-height distributions as a function of interaction position for the horizontal scan (5(a)). The full curves are splines to guide the eye, while the dashed curves display the predictions of a ray-tracing simulation of light propagation [42]. The simulation is in good agreement with the measured data. After gain correction, these distributions should be symmetric about the pixel boundary locations. The system was aligned such that position D should have corresponded to the boundary between P36 and P37. However, the fits to the data suggest that the scan positions were offset by 0.2 mm to the left (Fig. 5(e)). Corresponding fits to the vertical-scan data show a 0.4 mm vertical offset. The sum of the means of the two adjacent pixels scanned is also displayed. This shows that the amount of light collected by the two pixels over which the scan is performed is independent of position.

In general, several pixels adjacent to the target pixel will collect some scintillation light and in principle, this could be used to better localize the position of the scintillation as in an Anger camera [43,44]. While possible, this will not be the standard mode of operation for SoNDe modules running at ESS due to data-volume limitations. For production running at ESS, MAPMT pixels will be read and time-stamped on an event-by-event basis as lying either above or below per-pixel discriminator thresholds.

The multiplicity of pixels with a signal above discriminator threshold (the hit multiplicity denoted $M = 1$, $M = 2$, etc.) has been investigated as a function of the scintillation position and also the discrimination level. The investigation involved a 10×10 measurement matrix (100 runs total) of collimated α-particle irradiations, with 2000 events in each run. Fig. 6 displays regions in the vicinity of P37 where

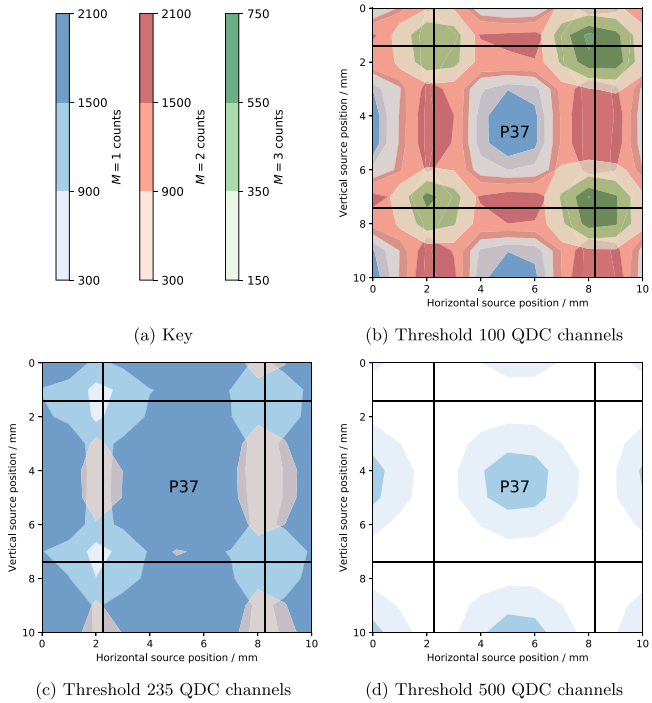

Fig. 6. Contour plots of the multiplicity distributions for pixels lying near P37 for different thresholds as a function of α-particle beam irradiation location. The black lines denote the pixel boundaries. In all three contour plots, blues indicate $M = 1$ events, reds indicate $M = 2$ events, and greens indicate $M = 3$ events. The lighter the shade of the color, the fewer the counts. (For interpretation of the references to color in this figure legend, the reader is referred to the web version of this article.)

$M = 1$, 2, and 3 predominate. Hits have been determined according to the pulse heights (Fig. 5) exceeding discrimination levels of 100 (6(b)), 235 (6(c)), and 500 (6(d)) QDC channels. At the 100-channel threshold, $M = 1$ events are confined to the center of a pixel. At the edges, events are predominantly $M = 2$, while in the corners, $M = 3$. To see any considerable $M = 4$ contributions around the pixel corners, lower thresholds are required as seen in Fig. 7. Raising the threshold to 235 channels extinguishes $M = 2$ and $M = 3$ almost completely. Raising even further to 500 channels serves merely to reduce the number of $M = 1$ events. The threshold level obviously affects the relative efficiency with which the SoNDe detector prototype registers $M = 1$, $M = 2$, etc. events, and Fig. 6 clearly shows that there is an optimum threshold value to maximize the number of $M = 1$ events detected and also to maximize the area of the detector where the $M = 1$ efficiency is high.

Fig. 7 illustrates the trend in M as a function of QDC threshold cut when a series of 36 α-particle beam measurements were performed in a 6 × 6 grid covering the face of P37. Variable thresholds have been applied to the data, but in each case, the same cut has been applied to all pixels. Two "extreme" curves are shown in 7(a): the $M = 0$ curve and the $M > 4$ curve. The $M = 0$ curve corresponds to events which do not exceed the applied threshold in any pixel. $M = 0$ events start to register at a threshold of ∼30 channels and rise steeply after channel ∼200 to ∼95% at channel 600. The $M > 4$ curve corresponds to events which exceed the applied threshold in four or more pixels. At a threshold of ∼4 channels, ∼90% of events are $M > 4$, falling essentially to zero at channel ∼50. Four other curves are shown in 7(b): $M = 1$, $M = 2$, $M = 3$, and $M = 4$, corresponding to events which exceed the applied threshold in one, two, three, and four pixels, respectively. Each of these curves demonstrate clear maxima so that the analysis procedure may be "tuned" to select an event multiplicity by applying the appropriate threshold. The detection efficiency for $M = 1$ events peaks at ∼75% at a threshold of 235 channels, where $M = 2$, 3, and 4 have negligible efficiency as they peak at channels 65, 25, and 18, respectively.

5. Summary and discussion

The position-dependent response of a SoNDe detector prototype, which consists of a 1 mm thick wafer of GS20 scintillating glass read out by an 8 × 8 pixel type H12700A MAPMT has been measured using a collimated ^{241}Am source. The spreading of the scintillation light and the resulting distributions of charge on the MAPMT anodes were studied as a function of α-particle interaction position by scanning the collimated α-particle beam across the face of the MAPMT using a high precision XY coordinate translator.

Initially, pixel gain non-uniformity across the 64 MAPMT anodes was measured using a 3 mm collimated source positioned at each pixel center, which produced uniform illumination of the pixel centers. The results, which differ from relative gain data provided by the MAPMT manufacturer on the 10% level (Fig. 4), were used to correct all subsequent 1 mm scan data.

Anode charge distributions collected from each MAPMT pixel at each scanned coordinate show a strong position dependence of the

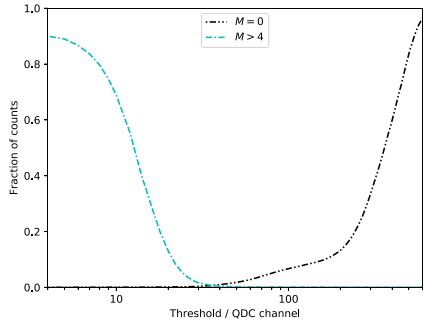

(a) Extreme multiplicities

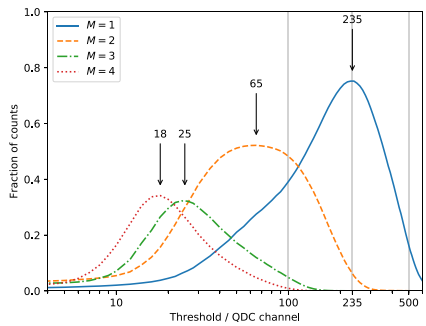

(b) Practical multiplicities

Fig. 7. Tuning the analysis using a single QDC threshold. Relationships between the relative number of events and threshold. Top Panel: $M = 0$ (black dot–dot-dashed line) and $M > 4$ (light blue dot-dashed line). Bottom Panel: $M = 1$ (dark blue solid line), $M = 2$ (orange dashed line), $M = 3$ (green dot-dashed line), and $M = 4$ (red dotted line). The gray vertical lines at QDC channel 100, 235, and 500 represent three of the QDC threshold cuts employed in Fig. 6. Arrows indicate the optimal values for QDC threshold cuts for tuning the resulting data set for a specific value of M. (For interpretation of the references to color in this figure legend, the reader is referred to the web version of this article.)

signal amplitude. The single-pixel signal is strongest when the source is located at the pixel center, and falls away as the pixel boundaries are approached (Fig. 5). At the pixel center, the signal tends to be concentrated in that pixel, while at pixel boundaries, the signal is shared between the adjacent pixels.

Rate and data-volume considerations for operation of SoNDe modules at ESS will require a relatively simple mode of operation for the SoNDe data-acquisition system. It will not be possible to read out multiple pixels to construct a weighted-mean interaction position as in an Anger Camera. Instead, it will be necessary to identify the pixel where the maximum charge occurs and record only the identity (P1–P64) of that pixel. To this end, we studied the effect of signal amplitude thresholds on the multiplicity of pixel hits (that is, the number of signals above threshold) as a function of the α-particle interaction position (Fig. 6). This study showed that there is an optimum discrimination level which maximizes the number of single-pixel or $M = 1$ hits. Below this level, multi-pixel hits start to dominate, while above this level, the single-pixel efficiency drops (Fig. 7). At the optimum discrimination level, which under the present operating conditions was channel 235, ~75% of the α-particle interactions were registered as single pixel.

Further work pertaining to the characterization of the SoNDe detector prototype is progressing in parallel to the project reported here. This includes the development of a simulation within the GEANT4 framework to complement and extend the ray-tracing simulation mentioned in this work. This GEANT4 model fully simulates the interactions of ionizing radiation in the GS20 and tracks the produced scintillation photons to the MAPMT cathode. It is being used to study the effects of optical coupling, surface finish, and partial pixelation (by machining grooves) of the GS20 wafer on the response of the detector. The present results, along with other measurements of the scintillator response will be used to test the predictions of the GEANT4-based model of the SoNDe detector prototype. The relative response of a SoNDe detector prototype to different incident particle species is also being studied. Irradiation of a SoNDe detector prototype with a collimated beam of thermal neutrons has been performed and data analysis is nearing completion. An extension of these studies for possible non-ESS applications of the SoNDe detector prototype, where an optical diffuser is inserted between the GS20 and the MAPMT, is planned to examine a possible Anger camera mode of operation. And further position-dependence studies will be made using fine needle-like beams of a few MeV protons and deuterons produced by an accelerator. This will allow determination of the scintillation signal as a function of interacting particle species and will be complemented by work with fast-neutron and gamma-ray sources.

Acknowledgments

We thank Prof. David Sanderson from the Scottish Universities Environmental Research Centre for providing α-spectroscopy facilities for the calibration of our ^{241}Am source. We acknowledge the support of the European Union via the Horizon 2020 Solid-State Neutron Detector Project, Proposal ID 654124, and the BrightnESS Project, Proposal ID 676548. We also acknowledge the support of the UK Science and Technology Facilities Council (Grant nos. STFC 57071/1 and STFC 50727/1) and UK Engineering and Physical Sciences Research Council Centre for Doctoral Training in Intelligent Sensing and Measurement (Grant No. EP/L016753/1).

References

[1] The European Spallation Source, https://europeanspallationsource.se/.
[2] R.T. Kouzes, PNNL-18388 Pacific Northwest National Laboratory, Richland, WA, 2009.
[3] D.A. Shea, D. Morgan, Congressional Research Service, Technical Report R41419, 2010.
[4] K. Zeitelhack, Neutron News 23 (4) (2012) 1013.
[5] Solid-State Neutron Detector, https://cordis.europa.eu/project/rcn/194934_en.html.
[6] S. Jaksch, et al., Proc int. conf. neutron optics (NOP2017), JPS Conf. Proc. 22 (2018) 011019, http://dx.doi.org/10.7566/JPSCP.22.011019.
[7] G. Kemmerling, S. Jaksch, Forschungszentrum Jülich, Solid-State Neutron Detector INFRADEV-1-2014/H2020, Grant Agreement Number: 654124.
[8] M. Heiderich, et al., Nucl. Instrum. Methods Phys. Res. A 305 (1991) 423, http://dx.doi.org/10.1016/0168-9002(91)90562-5.
[9] G. Kemmerling, et al., IEEE Trans. Nucl. Sci. 48 (2001) 1114, http://dx.doi.org/10.1109/23.958733.
[10] G. Kemmerling, et al., IEEE Trans. Nucl. Sci. 51 (2004) 1098, http://dx.doi.org/10.1109/TNS.2004.829576.
[11] G. Kemmerling, et al., IEEE Nucl. Sci. Symp. Conf. (2003) 722, Rec 03CH37515, http://dx.doi.org/10.1109/NSSMIC.2003.1351801.
[12] S. Jaksch, et al., Nucl. Instrum. Methods Phys. Res. A 762 (2014) 22, http://dx.doi.org/10.1016/j.nima.2014.04.024.
[13] A.V. Feoktystov, et al., J. Appl. Crystallogr. 48 (2015) 61, http://dx.doi.org/10.1107/S1600576714025977.
[14] R. Engels, et al., IEEE Trans. Nucl. Sci. 44 (3) (1997) http://dx.doi.org/10.1109/23.603701.
[15] R. Engels, et al., IEEE Trans. Nucl. Sci. 45 (3) (1998) http://dx.doi.org/10.1109/NSSMIC.1997.672706.

[16] R. Engels, et al., IEEE Trans. Nucl. Sci. 46 (4) (1999) http://dx.doi.org/10.1109/23.790694.
[17] R. Engels, et al., IEEE Trans. Nucl. Sci. 49 (3) (2002) http://dx.doi.org/10.1109/23.790694.
[18] S. Korpar, et al., Nucl. Instrum. Methods Phys. Res. A 442 (2000) 316, http://dx.doi.org/10.1016/S0168-9002(99)01242-5.
[19] K. Rielage, et al., Nucl. Instrum. Methods Phys. Res. A 463 (2001) 149, http://dx.doi.org/10.1016/S0168-9002(01)00448-X.
[20] T. Matsumoto, et al., Nucl. Instrum. Methods Phys. Res. A 521 (2004) 367, http://dx.doi.org/10.1016/j.nima.2003.11.384.
[21] K. Lang, et al., Nucl. Instrum. Methods Phys. Res. A 545 (2005) 852, http://dx.doi.org/10.1016/j.nima.2005.02.041.
[22] P. Abbon, et al., Nucl. Instrum. Methods Phys. Res. A 595 (2008) 177, http://dx.doi.org/10.1016/j.nima.2008.07.074.
[23] R.A. Montgomery, et al., Nucl. Instrum. Methods Phys. Res. A 695 (2012) 326, http://dx.doi.org/10.1016/j.nima.2011.11.026.
[24] Rachel Ann Montgomery, Nucl. Instrum. Methods Phys. Res. A 732 (2013) 732, http://dx.doi.org/10.1016/j.nima.2013.08.012.
[25] R.A. Montgomery, et al., Nucl. Instrum. Methods Phys. Res. A 790 (2015) 28, http://dx.doi.org/10.1016/j.nima.2015.03.068.
[26] X. Wang, et al., Chin. Phys. C 40 (2016) 086003, http://dx.doi.org/10.1088/1674-1137/40/8/086003.
[27] F. Zai-Wei, et al., Chin. Phys. C 36 (2012) 1095, http://dx.doi.org/10.1088/1674-1137/36/11/010.
[28] K.N. Yu, et al., Appl. Radiat. Isot. 59 (2003) http://dx.doi.org/10.1016/S0969-8043(03)00201-X.
[29] F.W.K. Firk, et al., Nucl. Instrum. Methods 13 (1961) 313, http://dx.doi.org/10.1016/0029-554X(61)90221-X.
[30] A.R. Spowart, Nucl. Instrum. Methods 135 (1976) 441, http://dx.doi.org/10.1016/0029-554X(76)90057-4.
[31] A.R. Spowart, Nucl. Instrum. Methods 140 (1977) 19, http://dx.doi.org/10.1016/0029-554X(77)90059-3.
[32] E.J. Fairley, et al., Nucl. Instrum. Methods 150 (1978) 159, http://dx.doi.org/10.1016/0029-554X(78)90360-9.
[33] Scintacor, https://scintacor.com/products/6-lithium-glass/.
[34] B. Jamieson, et al., Nucl. Instrum. Methods Phys. Res. A 790 (2015) 6, http://dx.doi.org/10.1016/j.nima.2015.04.022.
[35] A.W. Dalton, Nucl. Instrum. Methods Phys. Res. A 254 (1987) 361, http://dx.doi.org/10.1016/0168-9002(87)90685-1.
[36] C.W.E. van Eijk, et al., Nucl. Instrum. Methods Phys. Res. A 529 (2004) 260, http://dx.doi.org/10.1016/j.nima.2004.04.163.
[37] Hamamatsu Photonics, https://www.hamamatsu.com/resources/pdf/etd/H12700_TPMH1348Epdf.
[38] Thorlabs, Inc., http://www.thorlabs.com.
[39] R. Brun, et al., Nucl. Instrum. Methods Phys. Res. A 389 (1997) 81, See also http://root.cern.ch/.
[40] S. Agostinelli, et al., Nucl. Instrum. Methods Phys. Res. A 506 (2003) 250, http://dx.doi.org/10.1016/S0168-9002(03)01368-8.
[41] J. Allison, et al., IEEE Trans. Nucl. Sci. 53 (2006) 270, http://dx.doi.org/10.1109/TNS.2006.869826.
[42] Ray optics simulation, an open-source web application to simulate reflection and refraction of light. https://ricktu288github.io/ray-optics/.
[43] H.O. Anger, Rev. Sci. Instrum. 29 (1958) 27, http://dx.doi.org/10.1063/1.1715998.
[44] R.A. Riedel, et al., Nucl. Instrum. Methods Phys. Res. A 794 (2015) 224, http://dx.doi.org/10.1016/j.nima.2015.05.026.

Paper III

Nuclear Inst. and Methods in Physics Research, A 984 (2020) 164604

Contents lists available at ScienceDirect

Nuclear Inst. and Methods in Physics Research, A

journal homepage: www.elsevier.com/locate/nima

Response of a Li-glass/multi-anode photomultiplier detector to focused proton and deuteron beams☆

E. Rofors [a], J. Pallon [a], R. Al Jebali [b,d], J.R.M. Annand [d], L. Boyd [d], M.J. Christensen [c], U. Clemens [h], S. Desert [f], M. Elfman [a], R. Engels [g], K.G. Fissum [a,b,*], H. Frielinghaus [g], R. Frost [a], S. Gardner [d], C. Gheorghe [i], R. Hall-Wilton [b,e], S. Jaksch [g], K. Kanaki [b], G. Kemmerling [g], P. Kristiansson [a], K. Livingston [d], V. Maulerova [a,b], N. Mauritzson [a], R. Montgomery [d], H. Perrey [a], T. Richter [c], J. Scherzinger [a,b,1], B. Seitz [d], M. Shetty [c]

[a] Division of Nuclear Physics, Lund University, SE-221 00 Lund, Sweden
[b] Detector Group, European Spallation Source ERIC, SE-221 00 Lund, Sweden
[c] Data Management and Software Centre, European Spallation Source, Ole Maaløes Vej 3, 2200 Copenhagen, Denmark
[d] SUPA School of Physics and Astronomy, University of Glasgow, Glasgow G12 8QQ, Scotland, UK
[e] Dipartimento di Fisica "G. Occhialini", Università degli Studi di Milano-Bicocca, Piazza della Scienza 3, 20126 Milano, Italy
[f] LLB, CEA, CNRS, Université Paris-Saclay, CEA-Saclay 91191 Gif-sur-Yvette, France
[g] Jülich Centre for Neutron Science JCNS, Forschungszentrum Jülich, D-52425 Jülich, Germany
[h] Zentrum für Anwendungsentwicklung und Elektronik ZEA-2, Forschungszentrum Jülich, D-52425 Jülich, Germany
[i] Integrated Detector Electronics AS, Gjerdrums vei 19, NO-0484 Oslo, Norway

ARTICLE INFO

Keywords:
SoNDe thermal-neutron detector
GS20 scintillator
Li-glass
H12700A multi-anode photomultiplier
Position-dependent response
Protons
Deuterons

ABSTRACT

The response of a position-sensitive Li-glass based scintillation detector being developed for thermal-neutron detection with 6 mm position resolution has been investigated using focused beams of 2.5 MeV protons and deuterons. The beams were scanned across the detector in 0.5 mm horizontal and vertical steps perpendicular to the beams. Scintillation light was registered using an 8 × 8 pixel multi-anode photomultiplier tube. The signal amplitudes were recorded for each pixel on an event-by-event basis. Several pixels generally registered considerable signals at each beam location. To optimize planned detector operation at the European Spallation Source, the number of pixels above set thresholds was investigated, with the maximization of the single-hit efficiency over the largest possible area as the primary goal. For both beams, at a threshold of ~50% of the mean of the full-deposition peak, ~80% of the events were registered in a single pixel, resulting in an effective position resolution of ~5 mm in X and Y. Lower thresholds resulted in higher pixel multiplicities. These events could also be localized with the same effective position resolution.

1. Introduction

Position-sensitive ^{3}He-free [1–4] thermal-neutron detectors with high counting-rate capability are essential to the scientific program to be carried out at the European Spallation Source (ESS) [5–8]. Solid-state Neutron Detectors SoNDe (patent EP000003224652A1) [9–11] with two-dimensional position sensitivity will be employed for small-angle neutron-scattering experiments [12–21]. The modular SoNDe concept will facilitate the instrumentation of large areas with a position-reconstruction accuracy of ~6 mm for the detected neutron. A SoNDe "module" consists of a thin Li-glass scintillator sheet (GS20) that is sensitive to thermal neutrons coupled to a 64-pixel multi-anode photomultiplier tube (MAPMT) used to collect the scintillation light. Signals are read out using custom electronics which will time stamp all pixels with signals above threshold when any pixel-amplitude threshold is exceeded. Thus, while events where only a single pixel fired (multiplicity $M = 1$ events) will be straightforward to interpret, in the pixel-boundary regions, double or even higher-order counting can occur. The behavior of adjacent pixels when scintillation is registered in two or more of them (multiplicity $M > 1$ events) is thus of interest. Laser light and LEDs have previously been employed to study the responses of several different MAPMTs in detail [22–31]. Thermal neutrons have been used to perform first tests both on similar detectors [32] and on SoNDe modules [11,33]. A thermal-neutron interaction with the ^{6}Li of the Li-glass results in an α-particle

☆ The data set doi:10.5281/zenodo.3992851 is available for download from https://zenodo.org/record/399285.

* Corresponding author at: Division of Nuclear Physics, Lund University, SE-221 00 Lund, Sweden.
E-mail address: kevin.fissum@nuclear.lu.se (K.G. Fissum).

[1] Present address: Thermo Fisher Scientific Messtechnik GmbH, Frauenauracher Str. 96, 91056 Erlangen Germany.

https://doi.org/10.1016/j.nima.2020.164604
Received 25 May 2020; Received in revised form 26 August 2020; Accepted 30 August 2020
Available online 3 September 2020

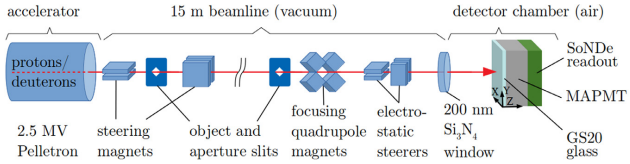

Fig. 1. A schematic view of the experimental setup (not to scale). The accelerator (left) produced continuous beams of protons or deuterons with currents in the ~nA range. The beams were transported and reduced in intensity via a beamline (middle) ending in a thin vacuum window. A detector chamber (right) operated at room temperature and pressure was positioned downstream of this window. The detector chamber contained a SoNDe module mounted on a motorized platform.

(2.05 MeV) and a triton 2.73 MeV). Scans of a collimated beam of ~ 4 MeVα-particles from a ^{241}Am source have been used to study the position-dependent response of a SoNDe detector prototype [34]. Here, beams of 2.5 MeV protons and deuterons have been scanned across the face of a SoNDe module. Apart from slightly lower scintillation-light output at a given energy, tritons are expected to behave in a manner very similar to protons and deuterons. The goals were to:

1. complement the existing α-particle studies on the position-sensitive response of the detector for events triggering up to four pixels to establish more precisely the response of a SoNDe module at the vertical and horizontal boundaries between pixels and the corners where four pixels meet
2. provide data with precision of better than 1 mm on the position sensitivity of the detector, primarily for events triggering only one pixel (Sections 2.2.3 and 4) as $M = 1$ mode of operation has been envisioned as the default for ESS
3. map the detector as a function of threshold and beam position when counting events which trigger only one pixel
4. determine the optimal detector threshold that maximizes this number of single-pixel events
5. identify regions, if any, where an event position-reconstruction accuracy better than 6 mm may be obtained for $M > 1$ events.

2. Apparatus

2.1. Proton and deuteron beams

The Lund Ion Beam Analysis Facility [35] of the Division of Nuclear Physics at Lund University employs a single-ended 3 MV (max) Pelletron electrostatic accelerator supplied by the National Electrostatics Corporation (NEC) [36]. This machine was used to deliver continuous beams of protons and deuterons with energies of 2.5 MeV to the module under investigation.

Fig. 1 shows the experimental setup. A 15 m long beamline between the Pelletron and the end station consisted of dipole magnets for energy selection and steering, object and aperture slits for adjusting the beam size and intensity, quadrupole magnets for focusing, and electrostatic steerers for fine tuning of the beam position [37,38]. A ~200 nm thick Si_3N_4 vacuum window [39] separated the high-vacuum beamline from the detector chamber operated at room pressure and temperature. The detector chamber contained a motorized XYZ translator on which a SoNDe module (Fig. 3(b)) was mounted. The beam spots at the location of the SoNDe module were estimated to be ~100 μm in diameter using a fluorescent glass plate. The sizes of the beam spots were due largely to multiple scattering in the vacuum window. Beam intensity was adjusted using the aperture slits so that the average counting rate on the SoNDe module was 5 kHz.

Fig. 2 shows a GEANT4 simulation [40] (Section 2.3) of the proton and deuteron energy loss in the vacuum window and air when the traversed air gap between the vacuum window and the GS20 was increased in 1 mm steps up to 6 mm. It predicts that a 2.5 MeV proton loses ~6 keV in the window and 14 keV/mm in air, while for deuterons the equivalent numbers are ~11 keV and 23 keV/mm. These results have been replicated using SRIM [41–43].

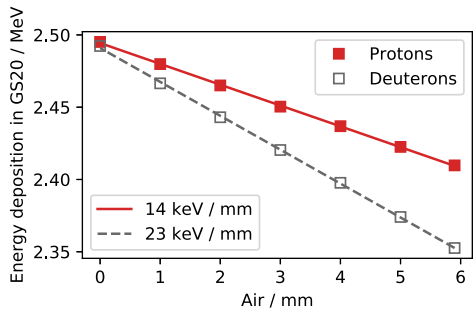

Fig. 2. GEANT4 predictions for the energy deposited in the scintillator by 2.5 MeV proton and deuteron beams after passing through the vacuum window and traversing increasing distances of room air before striking the Li-glass scintillator. The leftmost points correspond to the Li-glass scintillator being in contact with the vacuum window.

2.2. SoNDe module

As described in the following sections, the core components of a SoNDe module (Fig. 3) are:

1. a thin, lithium-silicate, scintillating-glass sheet
2. a MAPMT
3. purpose-built SoNDe readout electronics

2.2.1. Li-glass scintillator

GS20 [45–48] is cerium-activated lithium-silicate glass scintillator developed for the detection of thermal neutrons. The 50 mm × 50 mm × 1 mm sheet from Scintacor [49], had polished front and rear surfaces and rough cut 1 mm edges. The sheet was held in place on the MAPMT window using tape along the thin edges. Consistent with the planned configuration at ESS, no optical coupling medium was employed between the GS20 and MAPMT and no optical reflector was placed over the front face of the GS20. Facilitated by the abundance of scintillation light, this approach is due to the desire to minimize light spread to adjacent pixels and obtain stable long-term optical performance of the device. The density of ^{6}Li in GS20 (assumed to be uniform) is 1.58×10^{22} atoms/cm^3. At thermal energies (25 meV), the n + ^{6}Li → ^{3}H + α capture cross section is 940 b, resulting in a detection efficiency of ~75% for a 1 mm sheet. The capture process produces a 2.73 MeV ^{3}H (average range in GS20 of 34.7 μm) and a 2.05 MeV α-particle (average range in GS20 of 5.3 μm) [50]. The 6600 photon scintillation-light yield [11] corresponding to a thermal-neutron interaction (4.78 MeV) is quoted as 20%–30% of anthracene and the emission spectrum peaks at 390 nm [51]. For 2.48 MeV protons and 2.47 MeV deuterons, the GEANT4 simulation predicts ~118 and ~94 scintillation photons reaching the photocathode, respectively. Light transport from the GS20 (refractive index 1.55 at 395 nm) through a ~100 μm concave air

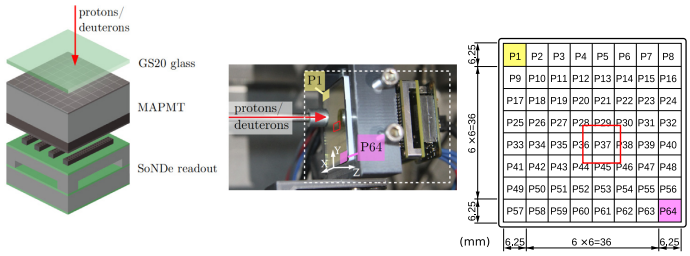

(a) SoNDe module (oblique view) (b) SoNDe module (side view) (c) MAPMT pixel map (front view)

Fig. 3. The SoNDe module. 3(a): 3D rendering of the SoNDe module. From the top, scintillator, MAPMT, and readout electronics. Beams of protons and deuterons (red arrow) arrive from the top. 3(b): Photograph of the SoNDe module (dashed white box — from the left, scintillator, MAPMT, and readout electronics) mounted on the motorized platform within the detector chamber downstream of the vacuum window. Beams of protons and deuterons (red arrow) arrive from the left. 3(c): Numbering scheme for the MAPMT pixels (front view) [44]. For orientation, Pixel 1 (P1, yellow), Pixel 64 (P64, pink), and the region of systematic irradiation (red box) are indicated both in panel 3(b) and 3(c). (For interpretation of the references to color in this figure caption, the reader is referred to the web version of this article.)

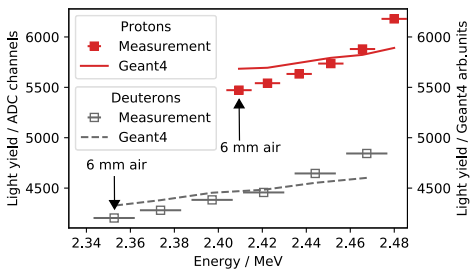

Fig. 4. Measured and GEANT4-simulated scintillation-light yields in GS20 produced by proton and deuteron beams of systematically decreasing energies. Note the suppression of zero on the y axis. Horizontal error bars are due to the uncertainty in the distance of air traversed while the vertical error bars are smaller than the symbols.

gap (refractive index 1) into the MAPMT borosilicate glass window (refractive index 1.53) is rather inefficient.

2.2.2. Multi-anode photomultiplier tube

Fig. 3(b) shows a photograph of the SoNDe module mounted in the detector chamber, while Fig. 3(c) shows a MAPMT pixel map. The 8 × 8 pixel Hamamatsu H12700A MAPMT chosen for the SoNDe module employs a borosilicate glass window. The outer dimensions of the MAPMT are 52 mm × 52 mm, while the active area of the photocathode is 48.5 mm × 48.5 mm. Thus 87% of the MAPMT surface is active. Each of the 64 pixels has an area of ∼6 mm × ∼6 mm. The peak quantum efficiency of the bialkali photocathode, ∼33% at ∼380 nm, is well matched to the scintillation emission spectrum from GS20, which peaks at ∼390 nm. The Hamamatsu data sheet for the H12700A MAPMT used in this study gives a gain of 2.09×10^6 and a dark current of 2.67 nA at a cathode-to-anode voltage of −1000 V and a factor 1.7 (worst-case) pixel-to-pixel gain difference. Electronic crosstalk between pixels is stated by Hamamatsu to be ∼2%. Calvi et al. [29] report that it is both pixel dependent and position dependent within a pixel and varies differently in the vicinity of horizontal (∼2%) and vertical (∼6%) pixel boundaries. The operating voltage employed was −900 V. Corrections for pixel-to-pixel variations in gain were performed [34] using the average values obtained from central-pixel proton and deuteron irradiations and applied offline.

2.2.3. Readout electronics

Produced by IDEAS [52], the readout electronics for the SoNDe module [11] consist of a front-end board and a controller board. The front-end board accommodates four 16-channel IDE3465 ASICs which digitize the MAPMT signals with 14-bit precision. The controller board houses an FPGA and a MiniIO port for communication via ethernet. Two modes of operation are "Time-of-Flight" mode (TOF), envisioned for production running at ESS at average rates of 20 MHz/m^2 and "All-Channel Spectroscopy" mode (ACS), used in this work, with a rate limitation of ∼10 kHz for one SoNDe module, equivalent to ∼4 MHz/m^2. In TOF mode, when any pixel-amplitude threshold is exceeded, the controller board is signaled to time stamp all of the pixels exceeding threshold with a precision of ∼150 ns and a resolution of 10 ns, and then pass the resulting time-stamped pixel addresses (IDs) to the ethernet interface. In ACS mode, when any pixel-amplitude threshold is exceeded, the digitized signals from all 64 pixels are read out. In the ACS-mode investigations, a low hardware threshold of 750 ADC channels was employed, which corresponds to 12.5% of the mean channel of the distribution of the full energy deposition of 2.48 MeV protons (Fig. 5). A threshold of at least 2500 ADC channels is necessary to completely discriminate against ∼ 1 MeV γ-rays (from a ^{60}Co source). γ-rays of a few MeV are typical backgrounds at accelerator facilities such as ESS, which is why a lower threshold may not be feasible. Higher thresholds were applied offline, as were corrections for differing pixel gains.

2.3. GEANT4 simulation

A detailed computer model of a SoNDe module is under development [53]. It uses the GEANT4 Monte Carlo toolkit [40] version 4.10.5 [54] and is coded in C++. The model includes the GS20 sheet, the MAPMT glass window and photocathode, and allows for optional optical coupling media between the GS20 and the MAPMT window. It simulates the interactions of ionizing radiation in the GS20 (scintillation emission) and tracks the resulting scintillation photons to the MAPMT cathode (scintillation transport). The model has greatly aided in the interpretation of the data. Fig. 4 shows the measured scintillation-light yield from the GS20 as the air gap between the vacuum window and the GS20 is varied, along with results from the simulation. For 2.5 MeV protons and deuterons, the GEANT4 simulation predicts ∼118 and ∼94 scintillation photons reach the photocathode, respectively. The light yield predicted by the simulation was normalized to the measured data so the deviation between measurements and simulations was minimized (at most 5%). It fits the data best when the Birks constant [55,56] for GS20 is set to 0.021 mm/MeV.

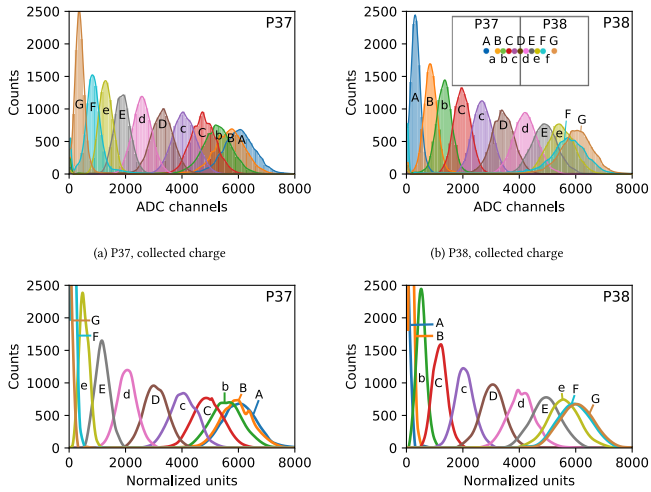

(a) P37, collected charge

(b) P38, collected charge

(c) P37, GEANT4

(d) P38, GEANT4

Fig. 5. Horizontal scan, proton beam. The colors and beam locations defined in the key (inset, top right panel) apply to the spectra of gain-corrected charge distributions (filled histograms, top panels) and GEANT4 simulations of the scintillation-light yield (open histograms, bottom panels). Spectra taken at positions a and f have been omitted for clarity, as they substantially overlap the results from the adjacent measurements. The normalized units were chosen to match the simulated distributions to the ADC spectra for the proton measurements at the pixel centers. (For interpretation of the references to color in this figure caption, the reader is referred to the web version of this article.)

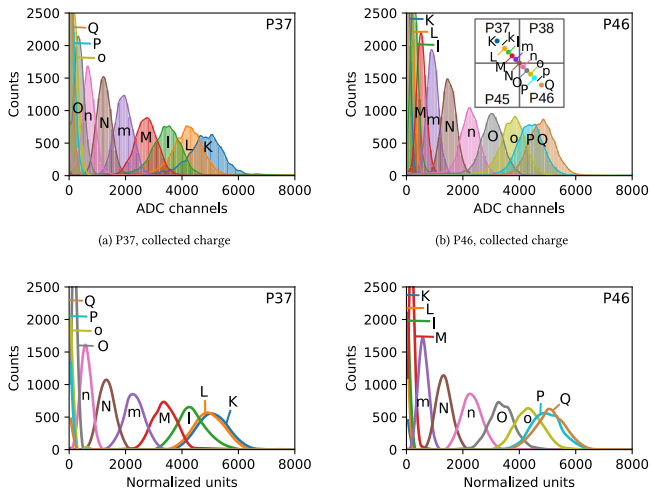

(a) P37, collected charge

(b) P46, collected charge

(c) P37, GEANT4

(d) P46, GEANT4

Fig. 6. Diagonal scan, deuteron beam. The colors and beam locations defined in the key (inset, top right panel) apply to the spectra of gain-corrected charge distributions (filled histograms, top panels) and GEANT4 simulations of the scintillation-light yield (open histograms, bottom panels). Spectra taken at positions k and p have been omitted for clarity, as they substantially overlap the results from the adjacent measurements. The normalized units were again chosen to match the simulated distributions to the ADC spectra for the proton measurements at the pixel centers. (For interpretation of the references to color in this figure caption, the reader is referred to the web version of this article.)

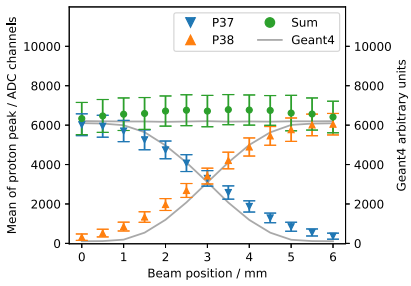

(a) Proton beam

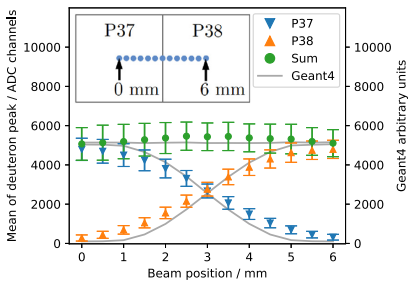

(b) Deuteron beam

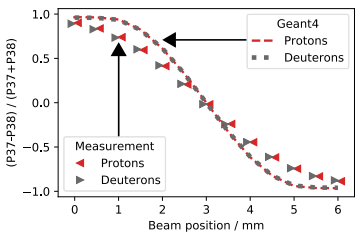

(c) Normalized

Fig. 7. Scintillation-light sharing. 7(a): proton beam. 7(b): deuteron beam. Points are gain-corrected means of the charge distributions corresponding to the division of scintillation light between P37 and P38 for a horizontal scan of the incident beam between pixel centers in 0.5 mm steps. The scan positions are indicated in the inset to 7(b). The uncertainties in the means of the fitted Gaussian distributions are smaller than the symbols. The error bars correspond to $\pm 1\sigma$ of these fitted distributions. The curves come from the corresponding GEANT4 simulations of the scintillation light. The simulations have been normalized to the measurements as before. 7(c): Light-sharing ratios (P37−P38)/(P37+P38) derived from the plots 7(a) and 7(b). The uncertainties are smaller than the widths of the lines.

The deviation may stem from effects such as electronic cross talk not yet covered in the simulation. The correlation between the data and simulations confirms that protons of all energies produce more scintillation light than deuterons of the same energy. This is because for a given energy, the specific ionization density of deuterons is higher than that of protons, resulting in a higher level of saturation of the local scintillation-production mechanisms.

3. Measurement

Proton and deuteron beams were used to systematically irradiate the SoNDe module at well-defined positions. After leaving the vacuum window, the beams passed through ∼1.0 mm of air before striking the upstream face of the GS20 sheet at normal incidence. The SoNDe module was translated with its face perpendicular to the direction of the beams using an XYZ-coordinate scanner instrumented with Physik Instrumente M-111 micro translation stages and C-862 motor controllers [57]. The scanning assembly was configured to allow for regular scans in two dimensions with a stepsize of 0.5 mm in both the X and Y directions. The assembly could also move in the Z direction away from the vacuum window. The temperature (∼25 °C), pressure (∼101.3 kPa), and humidity (∼30%) within the detector chamber that housed the scanning assembly were logged at the beginning and end of each scan.

The anode signals from each of the pixels in the MAPMT were processed using the purpose-built SoNDe electronics. The negative polarity analog pulses for each event with at least one pixel showing a signal above the threshold were measured. The threshold setting corresponded to an ADC value of about 750 channels. The data were recorded on disk using an ESS Event Formation Unit (EFU) [58–60] running on a Centos 7 PC connected through the MiniIO port to Ethernet using the UDP protocol [61]. The EFU data-acquisition system is designed for use by ESS instruments and the acquisition closely resembles the mode of operation anticipated at ESS. Data were recorded for ∼2 s (10000 events) at each point on a scan, followed by a motor translation, so that a complete scan of 2×2 pixels with 0.5 mm spacing took several hours. The data were subsequently analyzed using the `Python`-based [62] `pandas` [63] and `SciPy` [64] analysis tools.

4. Results

Previous work [22–27,30,34] clearly indicates that MAPMT pixel-gain maps are highly dependent upon the method of photon production. Thus, all of the results presented below have been pedestal and gain corrected with pixel-gain maps generated from the average of the proton- and deuteron-beam irradiations of the pixel centers.

Fig. 5 shows results from a horizontal scan of the SoNDe module across the proton beam from the center of P37 to the center of P38 in steps of 0.5 mm. Also shown are GEANT4 simulations. For 11 scan positions, the proton pulse-height spectra are displayed in Figs. 5(a) (P37) and 5(b) (P38) and the corresponding GEANT4-simulated scintillation-light yields are displayed in Figs. 5(c) (P37) and 5(d) (P38). The amount of scintillation light collected in a single pixel is clearly dependent upon the location of the proton beam. The amplitude of the signal is largest when scintillation light is produced at the center of the pixel and smallest when produced at the edge. Light produced at the boundary between two pixels is shared equally by both pixels. The simulations underestimate the amount of scintillation light spreading to the adjacent pixel closest to the particle interaction point by up to 15% depending on the beam position.

Fig. 6 shows results from a diagonal scan of the SoNDe module across the 2.47 MeV deuteron beam from the center of P37 to the center of P46 together with GEANT4 simulations. The scan was performed in a series of 0.5 mm horizontal and vertical steps, for an effective diagonal stepsize of 0.71 mm. For 13 scan positions, the deuteron pulse-height spectra are displayed in Fig. 6(a) (P37) and Fig. 6(b) (P46) and the corresponding GEANT4-simulated scintillation-light yields are displayed in Fig. 6(c) (P37) and Fig. 6(d) (P46). As anticipated, for a given pixel, the amplitude of the signal is largest when scintillation light is produced at the center of the pixel, and smallest when produced at the corner. Light produced at the corner of four pixels is shared equally by all four pixels. As before, the simulations underestimate the amount of scintillation light spreading to the pixels in close vicinity.

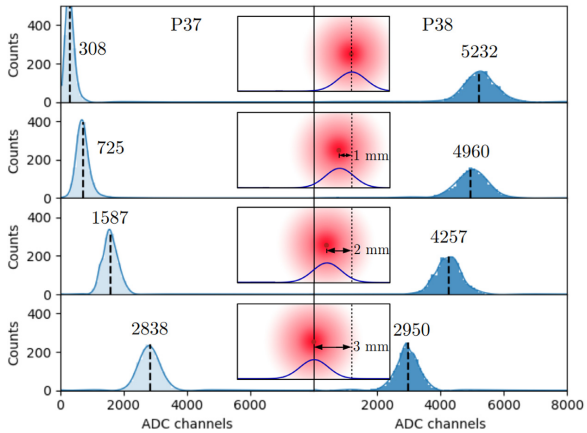

Fig. 8. Division of signal across adjacent pixels, proton beam. Central insets: GEANT4-simulated scintillation-photon distributions at the MAPMT photocathode (fuzzy red circles) resulting from incident proton beams (dark red dots) striking the SoNDe module at the four locations shown lying on the line of the horizontal scan from P37 to P38. The Gaussian curves are the X-projections of the simulated 2D distributions. The vertical line in the center of each inset represents the boundary between P37 and P38. Filled histograms: measured gain-corrected charge distributions for P37 (lighter blue, left column) and P38 (darker blue, right column). (For interpretation of the references to color in this figure caption, the reader is referred to the web version of this article.)

Fig. 7 shows how the scintillation light was shared by adjacent pixels P37 and P38 as the SoNDe module was scanned horizontally across the proton (Fig. 7(a)) and deuteron beams (Fig. 7(b)). Figs. 7(a) and 7(b) show the means of the pulse-height distributions displayed as a function of beam position. The curves are spline fits to the corresponding GEANT4 simulations. The sum distributions show that the proton beam produced a factor of ∼1.28 more scintillation light than the deuteron beam. The scan from P37 to P38 shows that light leakage to neighboring pixels is relatively low close to pixel centers. Moving the particle beam from the center of P37 towards P38, ∼4% of the total light yield is lost to P38 in the first mm. Across the boundary between the pixels, the light-loss gradient increases to 35%/mm. Based upon the α-particle scan results [34], it was anticipated that the sums of the gain-corrected charge distributions would be flat across the pixels and the boundary regions. Instead, the results have a slightly convex distribution centered at the pixel edge. This is because P37 and P38 together collect slightly more of the scintillation light produced from an event at the boundary between them than they collect from an event at the center of either pixel and the missing scintillation light is collected by the surrounding pixels. Fig. 7(c) shows the light-sharing ratio between P37 and P38 (defined as the difference between the means of the signal distributions in the pixels divided by the sum) for both protons and deuterons. The overlap between the proton and deuteron data indicates that the light-spreading mechanism is very similar for both particles. The absolute difference between the data and the simulation is up to 20%, greatest in the region in the middle of the center of a pixel and the edge. This difference could be due to scintillation-light spreading mechanisms which are not yet addressed in the simulation or electronic crosstalk.

The TOF mode of operation of SoNDe at ESS will result in a data set of time-stamped pixel IDs lacking the underlying ADC information. While $M = 1$ events will be straightforward to interpret, knowledge of the behavior of $M > 1$ events where adjacent pixels register scintillation is also important. Fig. 8 shows the division of the signal in the SoNDe module as the proton beam was stepped across the boundary between adjacent pixels. The ∼100 µm diameter proton beam was simulated using GEANT4 to produce a distribution of scintillation light incident on the photocathode with a FWHM of ∼2 mm. Given the 0.5 mm mapping stepsize, this means that the majority of the scintillation light corresponding to irradiations at the center of a pixel or the first two horizontal steps towards a boundary is detected by the irradiated pixel. Due to the width of the photon distribution, an increasing amount of signal is registered by the adjacent pixel as the boundary is approached. In the top panel, the beam was centered on P38 resulting in a ∼(94/6) P38/P37 division of the gain-corrected charge. In the second panel, the beam was translated 1 mm towards the boundary between P38 and P37, resulting in a ∼(87/13) signal division. In the third panel, another 1 mm shift closer to the P38/P37 boundary resulted in a ∼(73/27) division. In the bottom panel, the beam is incident on the boundary between pixels, resulting in a ∼(49/51) signal division. It is thus possible that in the regions near the boundaries between pixels, a triggering event may result in a large amount of charge in adjacent pixels, especially near corners.

This could be used to improve the position resolution for the scintillation as in an Anger camera [65,66]. While possible in principle, this will not be the standard mode of operation for SoNDe modules at ESS due to electronic, heat-load, and data-rate limitations. The TOF mode of operation which will be employed will result in a data set of time-stamped pixel IDs. Thus, while $M = 1$ events are preferable, knowledge of the behavior of the adjacent pixels when scintillation is registered in both as a function of threshold could be use to retain data which may otherwise be discarded.

In previous work [34] determining responses to scans of ∼1 mm FWHM beams of α-particles, the hit multiplicity ($M = 1$, $M = 2$, etc.) for adjacent pixels as a function of the beam-spot position was measured. A hit was registered if a pixel amplitude exceeded a threshold which was variable. Here, the procedure was repeated with the proton beam. A 26 × 26 grid of proton-beam irradiations with a stepsize of 0.5 mm in X and Y was performed. Fig. 9 displays results in the neighborhood of P37. Spatial distributions of multiplicity for software thresholds of 600 (Fig. 9(a)) and 2950 (Fig. 9(b)) ADC channels are shown. These thresholds correspond to 8% and 49% of the mean of the pixel-centered full-deposition proton peak, respectively. For a threshold of 600 ADC channels, $M = 1$ events are tightly constrained to within ∼1 mm of pixel centers. The $M = 2$, 3, and 4 data could all be localized to better than 5 mm, which is within the 6 mm position resolution

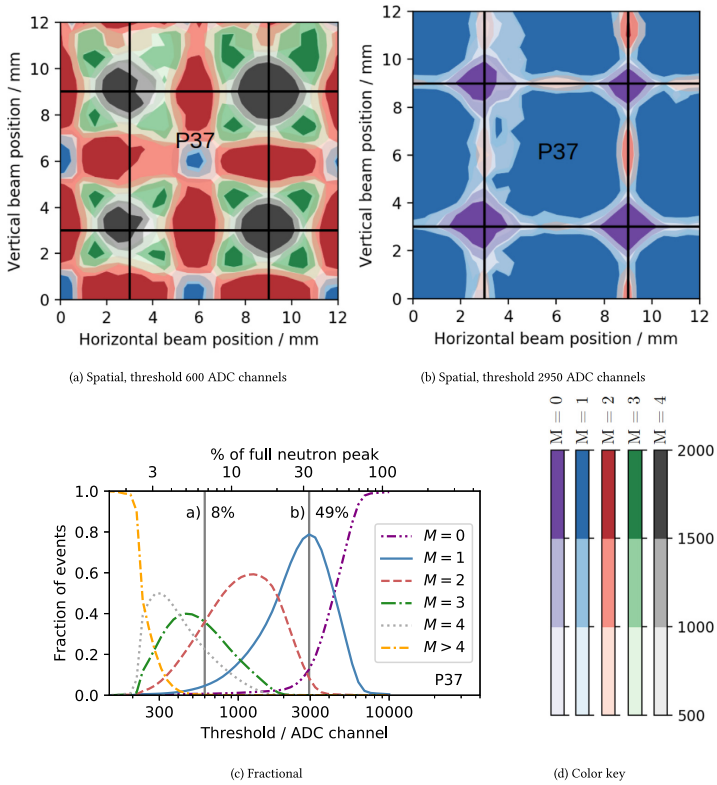

(a) Spatial, threshold 600 ADC channels

(b) Spatial, threshold 2950 ADC channels

(c) Fractional

(d) Color key

Fig. 9. Multiplicity distributions for the proton beam incident on P37 and the surrounding pixels. In 9(a) (threshold 600 ADC channels and 9(b) (threshold 2950 ADC channels, the black lines denote the pixel boundaries. Purple indicates $M = 0$ events, blue indicates $M = 1$ events, red indicates $M = 2$ events, green indicates $M = 3$ events, and gray indicates $M = 4$ events. The lighter the shade of the color, the fewer the number of events. 9(c) presents the fraction of events registered in P37 for each multiplicity as a function of threshold common to all pixels, with the 600 and 2950 ADC channel thresholds shown as vertical lines. 9(d) presents the color key for the spatial distributions. (For interpretation of the references to color in this figure caption, the reader is referred to the web version of this article.)

required for SoNDe operation at ESS. Raising the threshold to 2950 ADC channels results in the data being dominated by $M = 1$ events to within ∼1 mm of the pixel edges. The edges and particularly the corners are $M = 0$ zones where no events provide triggers. The threshold clearly affects the relative number of $M = 1$ events detected, and the 2950 ADC channel threshold maximizes both this number and the area of the detector where the $M = 1$ events are preferentially detected. The $M = 2$ data were confined to bands of width ∼2 mm centered on the pixel edges, well within the 6 mm position resolution required for SoNDe operation at ESS. Fig. 9(c) presents the threshold dependence of multiplicity for $M = 1$–4. Each of the curves demonstrate clear maxima so that the relative contribution of a given M can be maximized by suitable choice of threshold. For example, for the threshold of 2950 ADC channels optimized for $M = 1$ events, ∼79% of the events have $M = 1$, ∼9% have $M = 2$, and a negligible number have $M = 3,4$. The tradeoff is that ∼12% of events have $M = 0$, so that the consequence of operating the SoNDe module in $M = 1$ mode is a loss of ∼12% of events. A corresponding analysis of the deuteron data demonstrates the same behavior. The $M = 1$ optimal threshold cut for deuterons is ADC channel 2300 corresponding to 47% of the mean of the pixel-centered full-deposition deuteron peak.

5. Summary and discussion

The position-dependent response of a SoNDe module, which consists of a 1 mm thick sheet of GS20 scintillating glass coupled to a 64 pixel H12700A MAPMT has been measured using highly focused beams of protons and deuterons. The signal amplitudes from individual pixels were investigated as a function of beam position by stepping the module through the beams using a precision XY coordinate translator. The ∼100 μm diameter beams facilitated highly localized response mapping with a step size of 0.5 mm. A detailed GEANT4 model of the SoNDe module greatly aided in the interpretation of these data and facilitated the interpretation of the scintillation-light yield in GS20 (Fig. 4).

Gain-corrected signal amplitudes were highly dependent on the beam position (Figs. 5 and 6). The amount of light produced in the GS20 sheet by protons was a factor of ∼1.28 greater than that produced by deuterons. The spreading of light from protons and deuterons was indistinguishable. While overall agreement between the data and the simulations is very good, the simulations underestimated the scintillation light shared across a pixel boundary (Fig. 7). While not yet ready for the interpretation of ADC-free data corresponding to the operation of SoNDe in TOF mode, the simulation enables visualization

of the scintillation-photon distributions as a function of beam position (Fig. 8). The proton beam directed towards a central-pixel region resulted in little signal in an adjacent pixel. However, within ∼1 mm of the boundary, at least 40% of the scintillation light was registered in the adjacent pixel.

The effect of threshold on the hit multiplicity was studied as a function of beam position (Fig. 9). At a threshold of ∼50% of the mean of the proton full-deposition peak, ∼80% of the data had $M = 1$ and were localized to within 5 mm, ∼10% were $M = 2$, and ∼10% went undetected. The $M = 2$ data were confined to the pixel edges, and were thus within the 6 mm position resolution required for SoNDe operation at ESS. Increasing the threshold to higher than 50% of the mean of the proton full-deposition peak resulted in a reduction in the $M = 1$ event-detection efficiency and sensitive area of the detector. Decreasing the threshold to ∼8% of the mean of the proton full-deposition peak resulted in essentially no event loss, ∼5% $M = 1$ data localized to within 1 mm, and ∼ 95%$M > 1$ data. The $M = 2$, 3, and 4 data could all be localized to within 5 mm, again within the 6 mm position resolution required for SoNDe operation at ESS.

CRediT authorship contribution statement

E. Rofors: Conceptualization, Methodology, Software, Validation, Formal analysis, Investigation, Data curation, Writing - original draft, Writing - review & editing, Visualization, Project administration. **J. Pallon:** Investigation, Resources, Project administration, Supervision. **R. Al Jebali:** Conceptualization, Methodology, Investigation, Resources, Supervision. **J.R.M. Annand:** Conceptualization, Methodology, Software, Validation, Formal analysis, Investigation, Resources, Writing - original draft, Writing - review & editing, Visualization, Supervision. **L. Boyd:** Investigation. **M.J. Christensen:** Software. **U. Clemens:** Resources. **S. Desert:** Supervision. **M. Elfman:** Investigation, Resources. **R. Engels:** Supervision. **K.G. Fissum:** Conceptualization, Methodology, Validation, Formal analysis, Investigation, Resources, Writing - original draft, Writing - review & editing, Visualization, Supervision, Project administration, Funding acquisition. **H. Frielinghaus:** Resources. **R. Frost:** Investigation, Resources, Supervision. **S. Gardner:** Investigation. **C. Gheorghe:** Resources, Supervision. **R. Hall-Wilton:** Conceptualization, Resources, Supervision, Project administration, Funding acquisition. **S. Jaksch:** Conceptualization, Resources, Supervision, Project administration, Funding acquisition. **K. Kanaki:** Conceptualization, Resources, Supervision, Project administration, Funding acquisition. **G. Kemmerling:** Resources, Supervision. **P. Kristiansson:** Investigation, Resources, Supervision, Project administration, Funding acquisition. **K. Livingston:** Investigation. **V. Maulerova:** Investigation. **N. Mauritzson:** Investigation. **R. Montgomery:** Supervision. **H. Perrey:** Methodology, Software, Data curation, Visualization, Supervision. **T. Richter:** Software. **J. Scherzinger:** Supervision. **B. Seitz:** Supervision. **M. Shetty:** Software.

Declaration of competing interest

The authors declare that they have no known competing financial interests or personal relationships that could have appeared to influence the work reported in this paper.

Acknowledgments

The support of the European Union via the Horizon 2020 Solid-State Neutron Detector Project, Proposal ID 654124, and the BrightnESS Project, Proposal ID 676548 is acknowledged. The support of the Science and Technology Facilities Council, UK (Grant No. ST/P004458/1) and Engineering and Physical Sciences Research Council Centre for Doctoral Training in Intelligent Sensing and Measurement, UK (Grant No. EP/L016753/1) are also acknowledged, as is Strategic Accelerator Support from the Engineering Faculty (LTH) of Lund University, Sweden (Grant No. STYR 2019/1508).

References

[1] R.T. Kouzes, PNNL-18388 Pacific Northwest National Laboratory, Richland, WA, 2009, http://dx.doi.org/10.2172/956899.
[2] D.A. Shea, D. Morgan, Technical Report R41419, Congressional Research Service, 2010.
[3] K. Zeitelhack, Neutron News 23 (4) (2012) 10–13, http://dx.doi.org/10.1080/10448632.2012.725325.
[4] O. Kirstein, et al., PoS Proc. Sci. (Vertex2014), 029, 2014, arXiv:1411.6194 [physics.ins-det].
[5] M. Lindroos, et al., Nucl. Instrum. Methods Phys. Res. B 269 (2011) 3258, http://dx.doi.org/10.1088/1402-4896/aa9bff.
[6] S. Peggs, et al., ESS Technical Design Report, ISBN: 978-91-980173-2-8, 2013, https://europeanspallationsource.se/sites/default/files/downloads/2017/09/TDR_online_ver_all.pdf.
[7] R. Garoby, et al., Phys. Scr. 93 (2018) 014001, http://dx.doi.org/10.1016/j.nimb.2011.04.012.
[8] The European Spallation Source (ESS), European Spallation Source ERIC, Lund, Sweden, https://europeanspallationsource.se/. (Accessed 2020, Aug 19).
[9] Solid-State Neutron Detector – A new Neutron Detector for High-Flux Applications, EU Publications Office, https://cordis.europa.eu/project/id/654124. (Accessed 2020, Aug 19).
[10] S. Jaksch, et al., arXiv:1707.08679 [physics.ins-det].
[11] S. Jaksch, et al., in: Proc. Int. Conf. Neutron Optics, NOP2017, JPS Conf. Proc., vol. 22, 2018, p. 011019, http://dx.doi.org/10.7566/JPSCP.22.011019.
[12] M. Heiderich, et al., Nucl. Instrum. Methods Phys. Res. A 305 (1991) 423, http://dx.doi.org/10.1016/0168-9002(91)90562-5.
[13] R. Engels, et al., IEEE Trans. Nucl. Sci. 44 (3) (1997) http://dx.doi.org/10.1109/23.603701.
[14] R. Engels, et al., IEEE Trans. Nucl. Sci. 45 (3) (1998) http://dx.doi.org/10.1109/NSSMIC.1997.672706.
[15] R. Engels, et al., IEEE Trans. Nucl. Sci. 46 (4) (1999) http://dx.doi.org/10.1109/23.790694.
[16] G. Kemmerling, et al., IEEE Trans. Nucl. Sci. 48 (2001) 1114, http://dx.doi.org/10.1109/23.958733.
[17] R. Engels, et al., IEEE Trans. Nucl. Sci. 49 (3) (2002) http://dx.doi.org/10.1109/TNS.2002.1039590.
[18] G. Kemmerling, et al., IEEE Trans. Nucl. Sci. 51 (2004) 1098, http://dx.doi.org/10.1109/TNS.2004.829576.
[19] G. Kemmerling, et al., in: IEEE Nucl. Sci. Symp. Conf. Rec 03CH37515, 2003, p. 722, http://dx.doi.org/10.1109/NSSMIC.2003.1351801.
[20] S. Jaksch, et al., Nucl. Instrum. Methods Phys. Res. A 762 (2014) 22, http://dx.doi.org/10.1016/j.nima.2014.04.024.
[21] A.V. Feoktystov, et al., J. Appl. Crystallogr. 48 (2015) 61, http://dx.doi.org/10.1107/S1600576714025977.
[22] S. Korpar, et al., Nucl. Instrum. Methods Phys. Res. A 442 (2000) 316, http://dx.doi.org/10.1016/S0168-9002(99)01242-5.
[23] K. Rielage, et al., Nucl. Instrum. Methods Phys. Res. A 463 (2001) 149, http://dx.doi.org/10.1016/S0168-9002(01)00448-X.
[24] T. Matsumoto, et al., Nucl. Instrum. Methods Phys. Res. A 521 (2004) 367, http://dx.doi.org/10.1016/j.nima.2003.11.384.
[25] K. Lang, et al., Nucl. Instrum. Methods Phys. Res. A 545 (2005) 852, http://dx.doi.org/10.1016/j.nima.2005.02.041.
[26] P. Abbon, et al., Nucl. Instrum. Methods Phys. Res. A 595 (2008) 177, http://dx.doi.org/10.1016/j.nima.2008.07.074.
[27] R.A. Montgomery, et al., Nucl. Instrum. Methods Phys. Res. A 695 (2012) 326, http://dx.doi.org/10.1016/j.nima.2011.11.026.
[28] R.A. Montgomery, Nucl. Instrum. Methods Phys. Res. A 732 (2013) 732, http://dx.doi.org/10.1016/j.nima.2013.08.012.
[29] M. Calvi, et al., J. Instrum. 10 (2015) P09021, http://dx.doi.org/10.1088/1748-0221/10/09/p09021.
[30] R.A. Montgomery, et al., Nucl. Instrum. Methods Phys. Res. A 790 (2015) 28, http://dx.doi.org/10.1016/j.nima.2015.03.068.
[31] X. Wang, et al., Chinese Phys. C 40 (2016) 086003, http://dx.doi.org/10.1088/1674-1137/40/8/086003.
[32] F. Zai-Wei, et al., Chinese Phys. C 36 (2012) 1095, http://dx.doi.org/10.1088/1674-1137/36/11/010.
[33] E. Rofors, et al., Nucl. Instrum. Methods Phys. Res. A. (2020) in preparation.
[34] E. Rofors, et al., Nucl. Instrum. Methods Phys. Res. A. 929 (2019) 90, http://dx.doi.org/10.1016/j.nima.2019.03.014.
[35] Lund Ion Beam Analysis Facility (LIBAF), Division of Nuclear Physics, Lund, Sweden, http://www.nuclear.lu.se/forskning/tillaempad-kaernfysik/libaf/. (Accessed 2020, Aug 19).
[36] Electrostatic ion beam accelerator systems, National Electrostatics Corporation, 2020, https://www.pelletron.com/. (Accessed 2020, Aug 19).
[37] A. Shariff, et al., Nucl. Instrum. Methods Phys. Res. B 231 (2005) 7, http://dx.doi.org/10.1016/j.nimb.2005.01.027.
[38] M. Elfman, et al., Nucl. Instrum. Methods Phys. Res. B 231 (2005) 14, http://dx.doi.org/10.1016/j.nimb.2005.01.028.
[39] Silson Limited, Southam England, http://silson.com/. (Accessed 2020, Aug 19).

[40] S. Agostinelli, et al., Nucl. Instrum. Methods Phys. Res. A. 506 (2003) 250, http://dx.doi.org/10.1016/S0168-9002(03)01368-8.
[41] J.F. Ziegler, Nucl. Instrum. Methods Phys. Res. B. 219 (2004) 1027, http://dx.doi.org/10.1016/j.nimb.2004.01.208.
[42] J.F. Ziegler, et al., Nucl. Instrum. Methods Phys. Res. B. 268 (2010) 1818, http://dx.doi.org/10.1016/j.nimb.2010.02.091.
[43] J.F. Ziegler, Interactions of ions with matter, 2020, http://www.srim.org/. (Accessed 2020, Aug 19).
[44] Flat panel type multianode PMT assembly H12700 series/H14220 series, Hamamatsu Photonics K.K., Iwata City Japan, https://www.hamamatsu.com/resources/pdf/etd/H12700_H14220_TPMH1379E.pdf. (Accessed 2020, Aug 19).
[45] F.W.K. Firk, et al., Nucl. Instrum. Methods 13 (1961) 313, http://dx.doi.org/10.1016/0029-554X(61)90221-X.
[46] A.R. Spowart, Nucl. Instrum. Methods 135 (1976) 441, http://dx.doi.org/10.1016/0029-554X(76)90057-4.
[47] A.R. Spowart, Nucl. Instrum. Methods 140 (1977) 19, http://dx.doi.org/10.1016/0029-554X(77)90059-3.
[48] E.J. Fairley, et al., Nucl. Instrum. Methods 150 (1978) 159, http://dx.doi.org/10.1016/0029-554X(78)90360-9.
[49] 6-Lithium Enriched Glass Scintillators, Scintacor, Cambridge, England, https://scintacor.com/products/6-lithium-glass/. (Accessed 2020, Aug 19).
[50] B. Jamieson, et al., Nucl. Instrum. Methods Phys. Res. A 790 (2015) 6, http://dx.doi.org/10.1016/j.nima.2015.04.022.
[51] C.W.E. Van Eijk, et al., Nucl. Instrum. Methods Phys. Res. A 529 (2004) 260, http://dx.doi.org/10.1016/j.nima.2004.04.163.
[52] Integrated Detector Electronics AS, Oslo, Norway, https://ideas.no/. (Accessed 2020, Aug 19).
[53] J.R.M. Annand, et al., Nucl. Instrum. Methods Phys. Res. A. (2020) in preparation.
[54] J. Allison, et al., IEEE Trans. Nucl. Sci. 53 (2006) 270, http://dx.doi.org/10.1109/TNS.2006.869826.
[55] J.B. Birks, Proc. R. Soc. Lond. Ser. A Math. Phys. Eng. 64 (1951) 874, http://dx.doi.org/10.1088/0370-1298/64/10/303.
[56] J.B. Birks, The Theory and Practice of Scintillation Counting, Pergamon Press, New York, U.S.A., ISBN: 978-0-08-010472-0, 1964.
[57] PI – Solution for precision motion and positioning, Karlsruhe, Germany, https://www.physikinstrumente.com/. (Accessed 2020, Aug 19).
[58] A.H.C. Mukai, et al., J. Instrum. 13 (2018) T10001, http://dx.doi.org/10.1088/1748-0221/13/10/T10001.
[59] M.J. Christensen, et al., J. Instrum. 13 (2018) T11002, http://dx.doi.org/10.1088/1748-0221/13/11/T11002.
[60] M.J. Christensen, et al., Brightness Deliverable Report 5.6, Software Neutron Event Data Processing, 2018, http://dx.doi.org/10.17199/brightness.d5.6.
[61] M.J. Christensen, et al., arXiv:1706.00333 [physics.ins-det].
[62] G. van Rossum, F.L. Drake (Eds.), Python Reference Manual, PythonLabs, 2001, Available at https://www.python.org/.
[63] The Pandas development team, 2020, http://dx.doi.org/10.5281/zenodo.3964380, Pandas 1.1.0 available at https://pandas.pydata.org/. (Accessed 2020, Aug. 19).
[64] W. McKinney, in: Proceedings of the 9th Python in Science Conference, vol. 445, 2010, p. 56, http://dx.doi.org/10.25080/Majora-92bf1922-00a.
[65] H.O. Anger, Rev. Sci. Instrum. 29 (1958) 27, http://dx.doi.org/10.1063/1.1715998.
[66] R.A. Riedel, et al., Nucl. Instrum. Methods Phys. Res. A. 794 (2015) 224, http://dx.doi.org/10.1016/j.nima.2015.05.026.

Paper IV

Paper IV is available at arXiv:2010.06347 .

Paper V

Simulation of the Response of the Solid State Neutron Detector for the European Spallation Source

L. Boyd[a], E. Rofors[b], J. R. M. Annand[a], K. G. Fissum[b,c], R. Hall-Wilton[c,a,d], R. Al Jebali[a,c], K. Kanaki[c], K. Livingston[a], V. Maulerova[b,c], N. Mauritzson[b], R. Montgomery[a], H. Perrey[b,c], B. Seitz[a]

[a] *School of Physics and Astronomy, University of Glasgow G12 8QQ, Scotland, UK*
[b] *Division of Nuclear Physics, Lund University, SE-221 00, Lund, Sweden*
[c] *Detector Group, European Spallation Source ERIC, SE-221 00 Lund, Sweden*
[d] *Universita degli Studi di Milano-Bicocca, Piazza della Scienza 3, 20126, Milan, Italy*

Abstract

The characteristics of the Solid-state Neutron Detector, under development for neutron-scattering measurements at the European Spallation Source, have been simulated with a Geant4-based computer code. The code models the interactions of thermal neutrons and ionising radiation in the ^{6}Li-doped scintillating glass of the detector, the production of scintillation light and the transport of optical, scintillation photons through the the scintillator, en route to the photocathode of the attached multi-anode photomultiplier. Factors which affect the optical-photon transport, such as surface finish, pixelation of the glass sheet, provision of a front reflector and optical coupling media are compared. Predictions of the detector response are compared with measurements made with neutron and gamma-ray sources, a collimated alpha source and finely collimated beams of 2.5 MeV protons and deuterons.

1. Introduction

The European Spallation Source (ESS) [1, 2] based in Lund, Sweden is currently developing a number of instruments [3] for neutron science, one of which is the Small-K Advanced DIfractometer (SKADI) [4]. This small-angle neutron-scattering instrument will be used to investigate the properties of materials used in a broad range of scientific and medical research. The detector associated with the SKADI instrument is the Solid-state Neutron Detector (SoNDe) [5, 6, 7] which has a total area of $\sim$ 1040 $\times$ 1040 mm^2, and is constructed from 400 52 $\times$ 52 mm^2 elements. Each element consists of a 50 $\times$ 50 $\times$ 1 mm^3

*Corresponding author
Email address: john.annand@glasgow.ac.uk (J. R. M. Annand)

sheet of GS20 [8] ^{6}Li-doped glass scintillator coupled optically to a Hamamatsu H12700A 8×8 pixel, multi-anode photomultiplier tube (MAPMT) [9]. With this optical sensor, it is envisioned that the neutron-interaction position resolution will be ~ 6 mm, the dimension of a single MAPMT pixel. The module is designed to detect thermal neutrons through neutron capture within the scintillator $n+^6\mathrm{Li} \rightarrow ^3\mathrm{H} + ^4\mathrm{He}$. The alpha particle and triton, with a total energy of 4.78 MeV, produce optical scintillation photons which are detected by the MAPMT. A small self-contained data-acquisition (DAQ) system [10], attached directly to the rear of the MAPMT, digitises the MAPMT anode signals to produce a data set containing the amplitude, position and timing of the scintillation signal.

Various configurations of the module including:

- the use of a pixelated GS20 sheet
- the use of optical coupling medium
- the provision of a front reflector
- imperfect surface finish of the GS20 sheet

have been simulated to gauge their effect on the transport of optical photons. The response of the detector module has been measured using collimated beams of protons and deuterons [11], alpha particles [12], thermal neutrons [13] and uncollimated fast-neutron and gamma-ray sources. These measurements are compared with the predictions of the computer model described in this paper.

2. The Computer Model

The computer model of a SoNDe module uses the Geant4 Monte Carlo toolkit, version 4.10.6, [14] and is coded in C++. Included in the model are the GS20 sheet, the glass of the MAPMT window, the photocathode, optional optical coupling media between the scintillator and MAPMT and optional front reflectors.

2.1. Module Geometry

A rendering of the geometry encoded in the computer model is displayed in Fig. 1. This shows the scintillator, with optional grooving etched into the surface of the glass. Also displayed is the borosilicate glass of the MAPMT window and the tracks of optical photons (red lines) started at the mid point of pixel P28. The origin of the coordinate system, shown by the cross in Fig. 1A, is the centre of the cuboid volume which defines the GS20 sheet.

The dimensions of the GS20 sheet have been set to $50.0 \times 50.0 \times 1.0$ mm^3 to match the size of the piece used in test measurements. A thickness of 1 mm produces a thermal-neutron detection efficiency of $\sim 76\%$. The effectiveness of dividing the

GS20 sheets into pixels to reduce the spread of signal was investigated. Grooves in the glass surface, following the pixel boundaries of the MAPMT with variable depth and width, could be introduced optionally. The default surface finish of the GS20 sheet was polished and optional polished Al or matt TiO_2 reflector were included at the external front face of the sheet.

The dimensions of the H12700A MAPMT were taken from Ref. [9]. Only the glass window, dimensions $52.0 \times 52.0 \times 1.5$ mm^3, and the bialkalai photocathode, dimensions 48.5×48.5 mm^2, deposited on the back side of the window are modelled. Metalic side walls and internal electrode structures were not included in the model.

Although nominally flat, the borosilicate glass window of the MAPMT surface is slightly depressed at the center with respect to the edge. Measurements were made of 35 MAPMT windows, yielding a mean depression of 0.08 mm with a standard deviation $\sigma = 0.02$ mm. The exact shape of the window surface was not determined, but where there was no coupling medium between GS20 and MAPMT in the simulation, a small air gap of thickness 0.08 mm was introduced between the GS20 and MAPMT (Fig. 2(A)). Where a coupling medium (e.g. optical epoxy) was introduced it also had a thickness of 0.08 mm. Most of the calculations described in Sec. 3 have been made with a constant-thickness air gap. However the effect of a non-flat MAPMT was modelled by introducing a trapesoidal depression (Fig. 2(B)) to the window surface. Comparisons of flat and non-flat windows are given in Sec. 3.1.

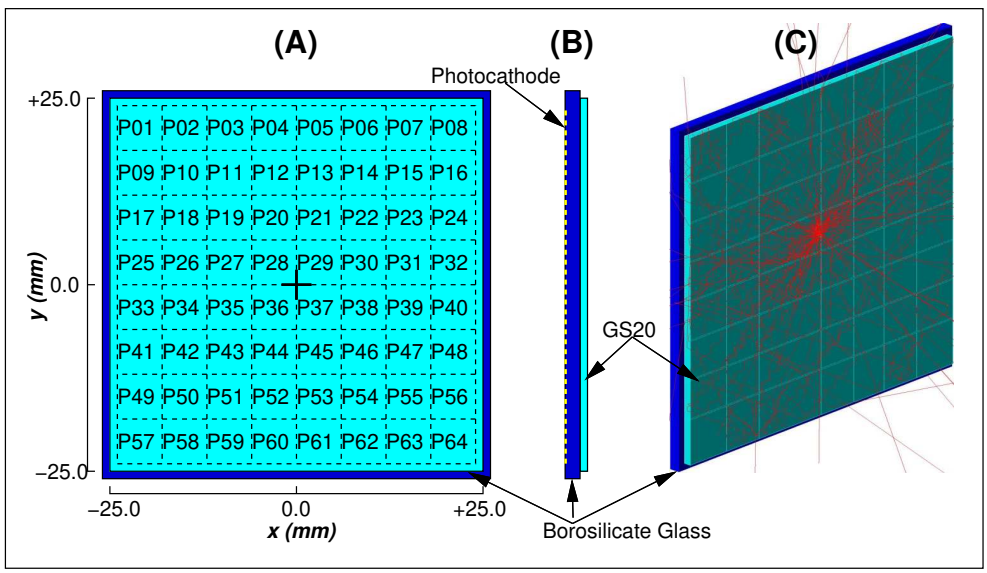

Figure 1: Rendering of the Geant4 model of a SoNDe module. (A) Front view where the cross denotes the x-y coordinate origin and the dashed lines show the photocathode pixel boundaries. The z origin is at the centre of the GS20 sheet. (B) Side view showing the photocathode (dashed yellow line) attached to the rear face of the glass window of the MAPMT. (C) 3D view where the red tracks show the scattering of 100 optical photons in the glass components.

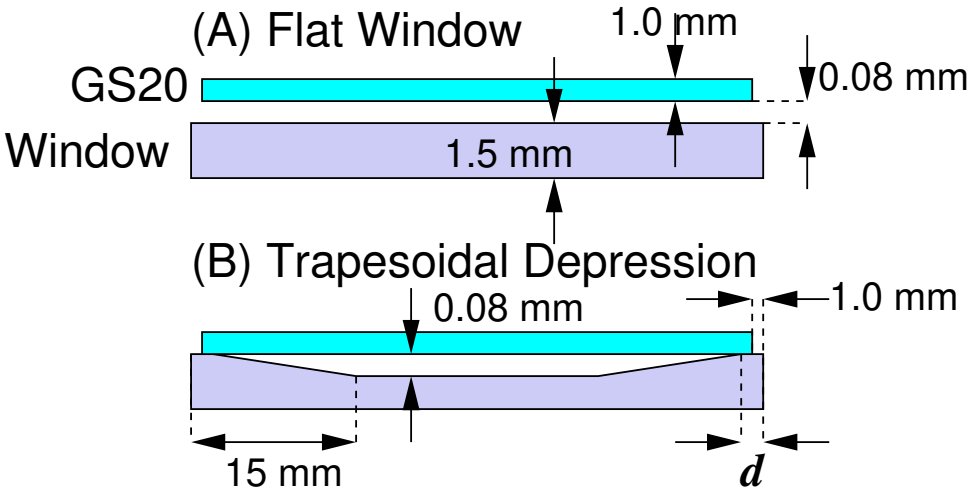

Figure 2: MAPMT window detail (not to scale).

2.2. Optical Properties

Optical photons were tracked [15] through the glass components of the detector as they undergo Rayleigh scattering, absorption and medium-boundary processes. Boundary processes, which were simulated using the 'glisur model' of Geant4, include:

1. dielectric to dielectric where the photon is refracted, ie transmitted through the boundary or reflected at the boundary.
2. dielectric to metal where the photon is absorbed in the 'metal' or reflected at the boundary.
3. dielectric to black where the photon is absorbed at the boundary.

The surfaces of the GS20, borosilicate PMT glass and any optional coupling medium were assumed to be polished, so that reflection was specular, but the effect of small surface irregularities was also calculated via the 'polish' parameter incorporated in the glisur model [16, 17]. This is also investigated in Sec. 4.2.

The optical properties of each material such as refractive index, $1/e$ attenuation length and reflectivity have been entered, for photon energies in the range 2.066 eV (600 nm) to 4.133 eV (300 nm), into the properties tables linked to particular materials. Some of the employed optical parameters are displayed in Fig. 3. EJ500 [18], the optional optical-coupling epoxy, was given a constant refractive index of 1.57.

A light output of 20% of anthracene (3500 photons/MeV), and a Birks parameter [19] $k_B = 0.01$ mm/MeV has been used for GS20 scintillator. The Birks parameter models the non-linear (with respect to energy deposit) response of the scintillator, which is due to increased quenching of the scintillation signal when dE/dx and the ionisation density along a charged track are large (see Eq. 2).

The optional outer reflector scintillator coatings were either matt TiO_2 paint [20] or polished Al foil. The former has $\sim 91\%$ reflectance at 390 nm, falling to 28% at 350 nm, while the latter has a reflectance of 92% at 390 nm, with a small wavelength dependence.

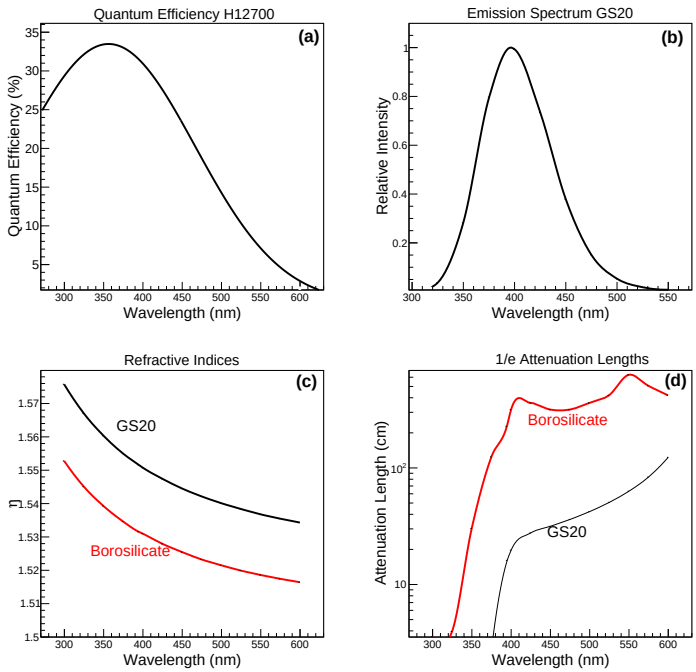

Figure 3: Optical properties employed in the simulation: (a) the quantum efficiency of the bialkalai cathode of the H12700 PMT [9], (b) the scintillation emission spectrum of GS20 [21], (c) refractive indices of GS20 [21] and borosilicate glass [22], (d) $1/e$ attenuation lengths of GS20 [21] and borosilicate glass [22].

2.3. Modes of operation

The code may be run in three different modes which are described below. In all cases information has been recorded event-by-event in ROOT TTree format [23] and then analysed using a ROOT C++ macro.

2.3.1. Optical Photon Transport

Optical photons were generated isotropically at a wavelength of 395 nm (3.15 eV), at a chosen point inside the GS20 sheet, using the General Particle Source tool of Geant4 . The wavelength corresponds to the peak of the scintillation emission spectrum of GS20. When a photon impinged on the photocathode, where it was absorbed, the photon wavelength, direction and interaction position were recorded. Otherwise if absorbed outside the photocathode or scattered outside of the detector volume the photon was lost.

2.3.2. Interactions of Ionising Radiation in GS20

The interactions of ionisating radiation within the sheet of GS20 have been modelled using the high-precision hadronic interaction class FTFP_Bert_HP and electromagnetic interaction classes G4EmStandardPhysics and G4EmExtraPhys For incident neutron energies below 4.0 eV the interaction class G4NeutronHPThermalScattering with data base G4NeutronHPThermalScatteringData was employed.

Primary and secondary (from gamma rays or neutrons) charged particles were tracked and the energy losses through ionisation recorded. At each discrete step along a charged-particle track the energy loss along the step, the time with respect to particle production at source and the mean step position were recorded in the ROOT TTree.

2.3.3. Full Calculation

This mode proceeded as in Sec. 2.3.2, but included the production of scintillation photons along the charged-particle tracks. Cherenkov radiation was also produced if the charged-particle velocity was above threshold for a particular optical medium. The optical photons were then tracked as in Sec. 2.3.1. In this mode, information for both the charged-particle track in the GS20 sheet and the optical photon impinging on the photocathode was recorded.

3. Optical Photon Transport Simulations

The transport of optical photons was simulated, for a variety of configurations of the SoNDe module, to calculate their spreading away from the point of origin before detection at the MAPMT photocathode. Parameters such as the grooving, optical coupling between scintillator and borosilicate glass, and reflective coatings for the scintillator were varied in various combinations. The optical photons were started at a random $x - y - z$ position within the GS20 and assigned a random direction of polarisation.

The 1 mm thick Li-glass sheet in front of the 4 pixels (P27, P28, P36, P37) bounding the center of the MAPMT was seeded uniformly with scintillation photons. The volume seeded was a cuboid centred at coordinate (0,0,0) (see cross in Fig. 1(A)) and the photon starting coordinates were constrainted to be within $-6 < x < +6$ mm, $-6 < y < +6$ mm, and $-0.5 < z < +0.5$ mm. The configuration of the SoNDe module was as in Run R_{11} (introduced and described below). Each scintillation photon with a unique, randonly-generated (x, y, z) start coordinate was then tracked until it struck a photocathode pixel, where it was recorded. Fig. 4 shows the results of this tracking, illustrating the correlation between the start coordinates of a photon and the pixel where the photon was finally detected. Each panel corresponds to single photocathode pixel and has been populated with the (x, y) start coordinates of the photons which are detected in that pixel. The 16 pixels P5 – 8, P13 – 16, P21 – 24

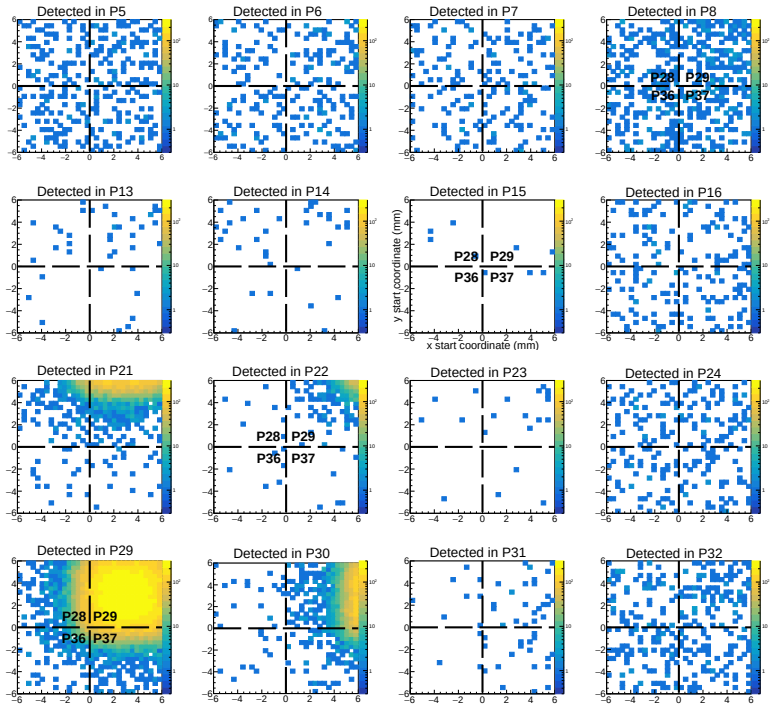

Figure 4:
Starting (x, y) coordinates for photons registered in the top-right quadrant of MAPMT pixels. Dashed lines show pixel boundaries between P28, P29, P36 and P37. Pixel numbering is given in Fig. 1.

and P29 – 32 correspond to the top right-hand 4×4 quadrant of the MAPMT (Fig. 1(A))

Evidently, hits in P29 were overwhelmingly due to photons seeded in front of P29, but a significant number of photons seeded in front of P28, P36 and P37, mostly within ~ 2 mm of the boundary to P29, were also registered in P29. Similarly for hits in the nearest neighbours to P29: P21 (vertical), P30 (horizontal) and P22 (diagonal), the start coordinates are clustered close to the neighbour's boundary with P29. MAPMT edge pixels P5 – 8, P16, P24 and P32 record more photons than P13 – 15, P23 and P31, which are closer to the photon source, due to reflections at the thin side edge of the GS20 sheet. In these edge pixels, there is no obvious correlation between the start position and the pixel where the photon is detected.

Further runs were made with the $x-y$ start coordinates covering the entire GS20 sheet: $-25 < x < +25$ mm, $-25 < y < +25$ mm and again the z coordinate was constrained to be within the 1 mm thickness. The simulation was split into 28 runs, each starting 8×10^7 optical photons, with direction sampled from an isotropic angular distribution. They were arranged in 4 groups of 7. The 4

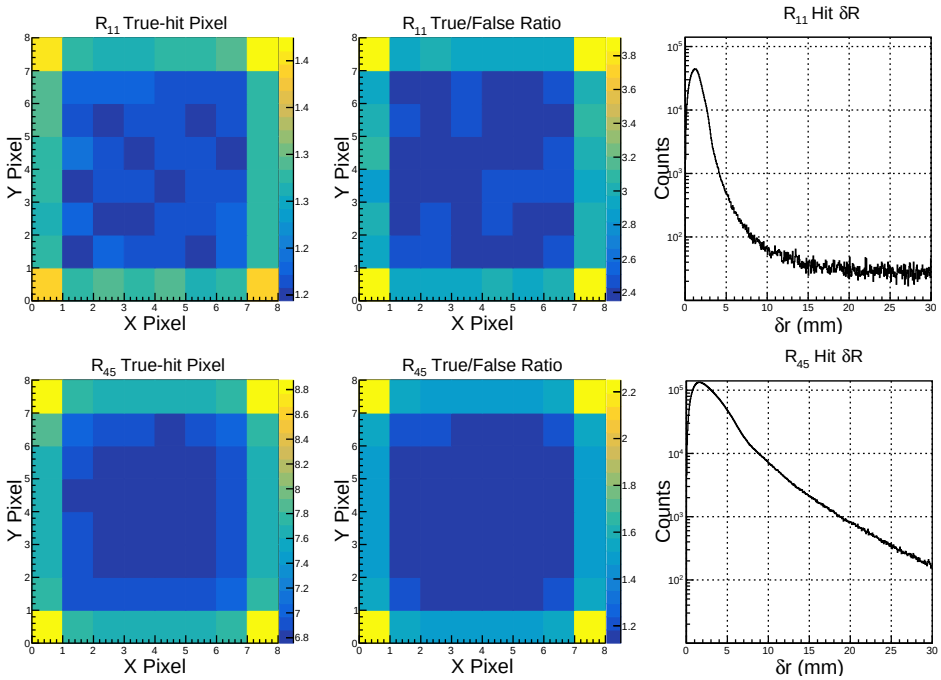

Figure 5: Top row R_{11} results, left ϵ_T for each illuminated pixel, centre R_{TF} for each illuminated pixel, right δr for entire illuminated region. Bottom row R_{45} results, order as in top row. Note that the colour vertical scales are different for each 2D pixel plot.

groups corresponded to conditions:

1. No grooving of the GS20 sheet.
2. Grooving 0.5 mm deep and 0.2 mm wide, cut on the outside face of the GS20 sheet.
3. Grooving 0.5 mm deep and 0.2 mm wide, cut on the inside face of the GS20 sheet.
4. Grooving 1.0 mm deep (i.e. all the way through the sheet) and 0.2 mm wide.

Within each group, the 7 sub-groups correspond to conditions:

1. No external reflector on the outside face of the GS20 sheet and no optical coupling between the GS20 and MAPMT window.
2. TiO_2 reflector on the outside face of the GS20 and no optical coupling.
3. Polished Al reflector on the outside face of the GS20 and no optical coupling.
4. Polished Al reflector on the outside face of the GS20 and optical epoxy coupling between the GS20 and MAPMT window
5. TiO_2 reflector on the outside face of the GS20 and optical epoxy coupling.
6. No reflector and optical epoxy coupling.

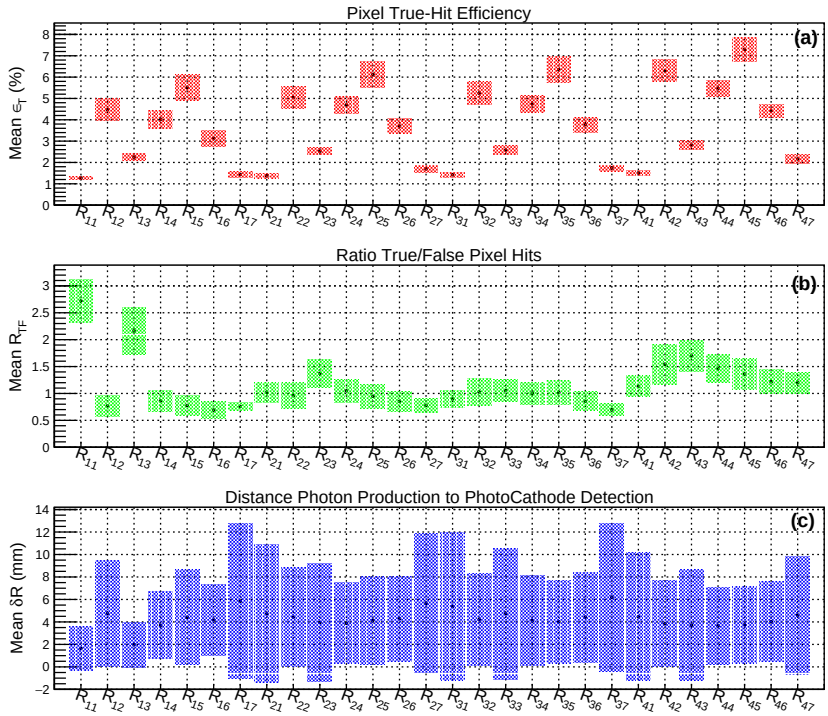

Figure 6: Summary of photon transport results: a) mean values ϵ_T; b) mean values R_{TF}; c) mean values δr. The x-axis labels refer to the run labels R_{ij} explained in the text. The vertical extents of the filled boxes, display the standard deviations (Eq. 1).

7. As item 1, but with the surface polish factor for the GS20 sheet set to $P = 0.8$. P values may be varied from 0.0 to 1.0 [17] where the latter denotes a perfect surface. The MAPMT surface was set to perfectly polished ($P = 1.0$).

Runs have been labelled R_{ij}, where $i = 1, 4$ is the group and $j = 1, 7$ is the sub-group. Analysis of the Monte Carlo output has determined the $x-y$ translation distance, $\delta r = \sqrt{\delta x^2 + \delta y^2}$, where δx and δy are the differences between the photon-start coordinates and the photon-detection coordinates at the MAPMT photocathode. The MAPMT hardware can resolve detected photon position down to the 6×6 mm photocathode pixel size. Thus the analysis determines if the photon-start pixel is the same as the photocathode-detection pixel, which is denoted a true hit. Where the start and detection pixels are not the same, this is denoted a false hit. The true-hit efficiency ϵ_T is just the ratio of detected-to-started photons within a given pixel (expressed in %), while R_{TF} is the ratio of the number of true-to-false hits in a given pixel.

Representative distributions are given for runs R_{11} and R_{45} in Fig. 5, which displays the pixel distributions of ϵ_T and R_{TF} and δr for the entire array. While ϵ_T is much larger for R_{45}, where the TiO_2 reflector increases the overall

light-collection efficiency significantly, R_{TF} is significantly higher for R_{11} (no reflector) which correlates with a significantly smaller average δr.

A summary of the results for all runs is displayed in Fig. 6. Fig. 6(a) displays the mean value of ϵ_T for all illuminated pixels. The error-bars show the standard deviations of the individual-pixel, true-hit efficiencies

$$\sigma_\epsilon = \sqrt{\frac{\sum_{i=1}^{N} (\epsilon_i - \overline{\epsilon})^2}{N-1}} \tag{1}$$

where ϵ_i are the individual-pixel efficiencies, $\overline{\epsilon}$ is the mean efficiency averaged over all illuminated pixels and N is the number of illuminated pixels. Fig. 6(b) displays the mean R_{TF} for each run, and again the error bars denote the standard deviations of the individual-pixel ratios. Fig. 6(c) displays the mean values (averaged over all illuminated pixels) of δr for each run, where the error bars denote the standard deviation of the mean, related to the spread in event-by-event δr values over the entire illuminated region.

Comparing the main group runs, grooving of the GS20 sheet does increase ϵ_T slightly, but compared to no grooving R_{TF} is smaller and δr is slightly larger on average. Within the sub-groups, TiO_2 matt reflector and optical epoxy coupling produce the highest ϵ_T. However a polished Al reflector gives better R_{TF} especially if no epoxy coupling is employed. Overall, the best R_{TF} is obtained in R_{11}: no grooves, no reflector and no epoxy coupling, although in this case ϵ_T is the lowest of all runs. Comparing R_{11} ($P = 1.0$) and R_{17} ($P = 0.8$), the latter shows a large reduction in R_{TF}, a large increase in δr and a small increase in ϵ_T.

3.1. Comparison of flat and non-flat MAPMT window

Optical simulations were performed for 6 geometries of the MAPMT window (Fig. 2): (1) flat face; (2) trapesoidal face $d = 1.00$ mm; (3) trapesoidal face $d = 1.01$ mm; (4) trapesoidal face $d = 1.10$ mm; (5) trapesoidal face $d = 1.50$ mm; (6) trapesoidal face $d = 2.00$ mm; where the width of the overlap ($d - 1.0$ mm) defines the area of GS20-glass contact at the edge of the sheet. Otherwise the SoNDe module was in R_{11} configuration. The results are summerised in Fig. 7. Cases 1 and 2 are very similar, so that the shape of the air gap, trapesoidal or constant thickness, makes little difference. Where parameter $d > 1.0$ mm (cases 3 - 6) , there is an area of contact between the GS20 and borosilicate window. As d increases the mean value of ϵ_T increases slightly, R_{TF} decreases and δr increases. The spread of values of these parameters also increases with d, as the divergence in response between edge pixels, close to the contact area, and more central pixels increases.

The exact shape of the MaPMT surface has not been measured, but it seems unlikely that there will be a large contact area between the GS20 and borosilicate window. Subsequent calculations in Sec. 4 have been made with a flat MaPMT window and correspond to run case R_{11} described above.

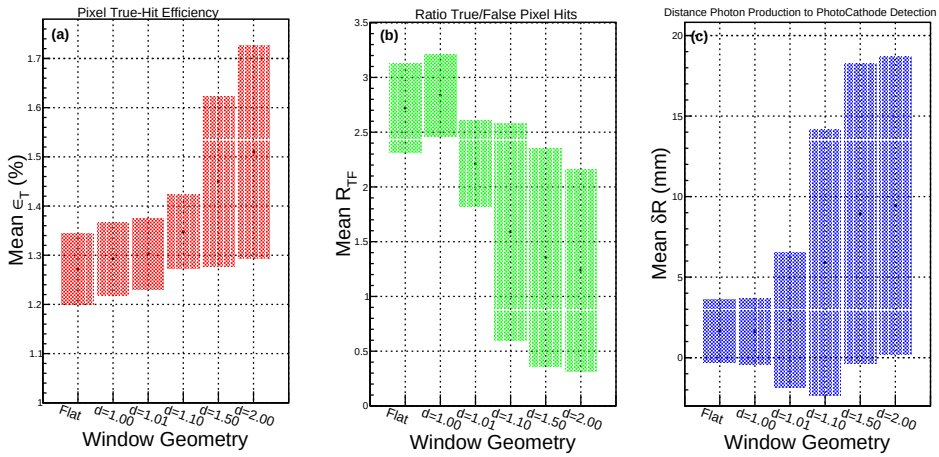

Figure 7: Window-geometry dependence: (a) true-hit efficiency ϵ_T; (b) true-hit/false-hit ratio R_{TF}; (c) δR; The vertical extents of the filled boxes, display the standard deviations (Eq. 1) of the respective parameters.

4. Response to Ionising Radiation

GS20 is designed to detect thermal neutrons but scintillating glass is sensitive to ionising radiation in general. The 1 mm thickness of the GS20 sheet is a compromise between high detection efficiency ($\sim$ 76%) for thermal neutrons and low detection efficiency for background radiation. Increasing the thickness will increase the background efficiency preferentially, relative to that of thermal neutrons. In operation at ESS the potential sources of background will be gamma rays [24] and fast neutrons [25], which will range in energy from sub-MeV to around GeV.

When comparing the response of a scintillator to low-energy particles of different types, non-linear effects due to quenching of the scintillation process must be taken into consideration. This is performed in Geant4 using the empirical formula of Birks [19]

$$\frac{dL}{dx} = S\frac{\frac{dE}{dx}}{1 + k_B\frac{dE}{dx}} \tag{2}$$

which relates the scintillation light yield per unit path dL/dx to the scintillation efficiency S, the differential charged-particle energy loss dE/dx and a material-dependent constant k_B, often known as the Birks parameter. This parameter is not well established for the glass GS20. A study of a variety of inorganic crystaline scintillators [26] has produced values of k_B in the range $10^{-3} - 10^{-2}$ g/cm^2/MeV. A value: $k_B = 10^{-2}$ g/cm^2/MeV has been employed for GS20, which is discussed in Sec. 4.3.3.

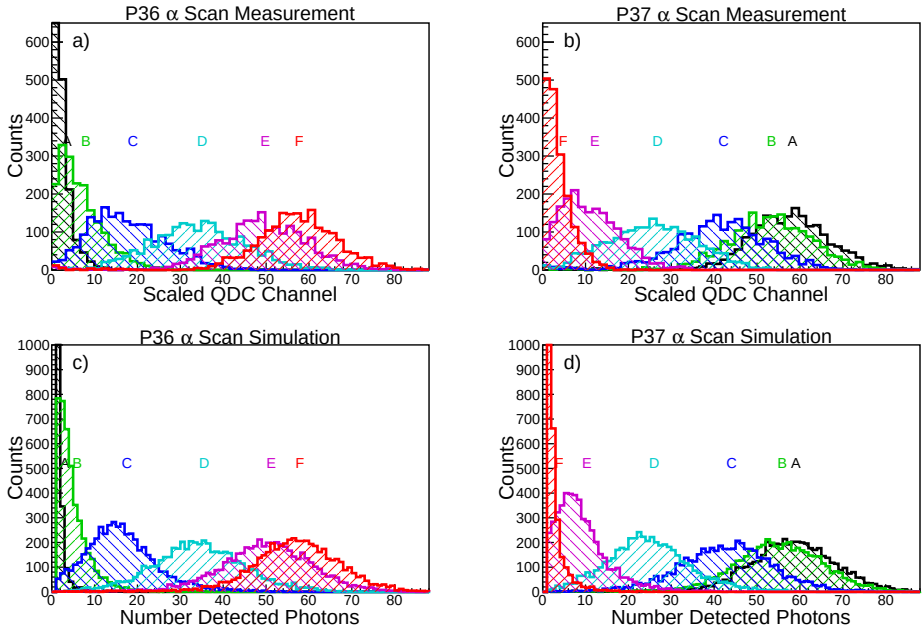

Figure 8: Alpha source horizontal scan signal amplitude spectra: a) P36 measurement; b) P37 measurement; c) P36 simulation; d) P37 simulation.

4.1. Position-Dependent Alpha-Particle Response

A collimated ^{241}Am alpha-particle source was employed to measure the position dependence of the signal amplitude from the individual MAPMT pixels of a SoNDe module. Measurements of the alpha response, as the collimated source was scanned across the face of the GS20 sheet, have been reported in Ref. [12] and these measurements have been simulated with the present computer model. Incident alpha-particle energies were sampled from the measured energy spectrum of the employed ^{241}Am source and their direction was restricted to a cone of half-angle 6.2°. normal to the plane of the scintillator sheet, to reproduce the experimental collimation. The alpha particles passed through $\sim$ 6 mm of air before incidence on the GS20, so that their mean energy at the scintillator was $\sim$ 4 MeV (see Fig. 2 of Ref. [12]) and the diameter of the illuminated spot at the GS20 face was $\sim$ 1.3 mm. There was $\sim$ 0.2 mm uncertainty in the experimental beam spot diameter due to uncertainties in the internal dimensions of the metal source container.

Fig. 8 compares the measured alpha-particle spectra, from MAPMT pixels 36 and 37 (Fig. 1(A)), to the corresponding simulated spectra for a horizontal scan over positions labeled A-F (see Fig. 5 of Ref.[12]). Labels A, B, C, D, E, F correspond to x coordinates 2.74, 1.74, 0.74, -0.26, -1.26, -2.26 mm respectively, with the y coordinate fixed at -3.4 mm. The coordinate system is displayed in Fig. 1(A)). Fig. 9 compares the position dependence of the mean values and widths of the spectral distributions at the 6 scanned x coordinates. The

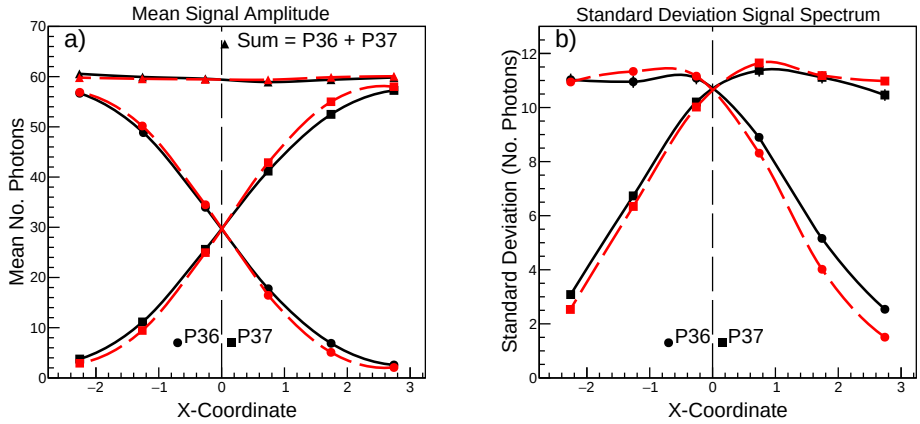

Figure 9: Alpha source scan position dependence: a) measured (black) and simulated (red) signal amplitudes; b) measured (black) and simulated (red) standard deviations of signal amplitude spectra. Circles denote pixel P36 and squares P37. The dashed line denotes the vertical boundary between P36 and P37.

bin widths of the measured histograms (QDC channel in Ref. [12]) have been scaled, so that the average of the 6 summed (P36 + P37) points is equal to the corresponding simulated quantity, i.e. the measured signal charge has been normalised to the calculated mean number of detected scintillation photons.

The agreement between the measured and simulated position dependence of the mean pulse height is excellent. The agreement for the position dependence of the widths (standard deviations of the spectral distributions) is also good, although the simulation slightly overpredicts the change in signal amplitude as one moves from position A to F. This would be expected if effects such as electronic noise, which were not simulated, made a non-negligible contribution to the measurement. This is explored further in Sec. 4.2.

4.2. Position-Dependent Response to Monoenergetic Protons

The Lund LIBAF facility [27] provides finely-collimated, monoenergetic beams of protons and deuterons at energies up to 3 MeV. Ref. [11] describes detailed scans of LIBAF proton beams across the face of a SoNDe module and gives a first comparison of the proton measurements with the simulation. Here we show a further comparison with unpublished data taken at LIBAF and the latest version of the simulation.

Two linear scans were made: horizontal covering coordinates 2.4 - 12.9 mm at fixed $y = 1.90$ mm, in 0.5 mm steps and vertical covering coordinates -5.6 - 1.9 mm at fixed $x = 8.4$ mm, in 0.5 mm steps. The beam energy was set to 2.5 MeV and energy losses in the beam line and air before protons hit the GS20 sheet amounted to around 20 keV. Details of the proton beam line and x-y scanner are found in Ref. [11]. The data were collected using a VMEbus-

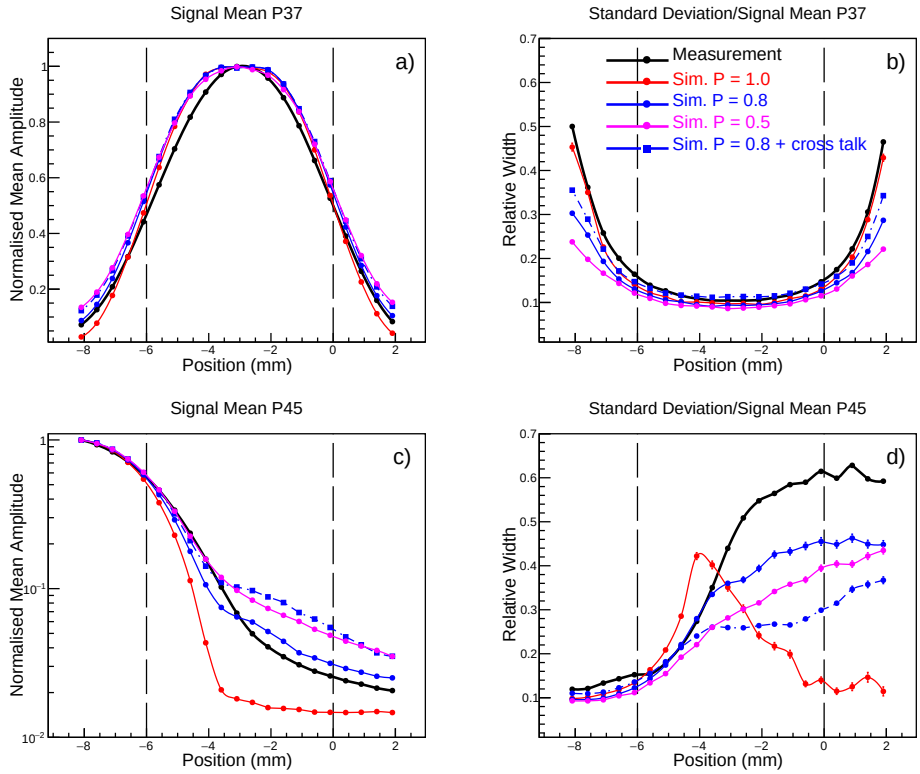

Figure 10: Vertical proton scan: means and standard deviations of pulse-height spectra from P37 (plots (a), (b)) and P45 (plots (c), (d)). Colour coding is shown in plot (b) and applies to all sub-plots. The vertical dashed lines show the boundaries of pixels 45-37 (left) and 37-29 (right).

based, data-acquisition system similar to that described in Ref. [28] with the pulse-height spectra accumulated in CAEN V792 charge-to–digital converters.

Fig. 10 compares the vertical-scan measurements (black circles and lines), for vertically adjacent pixels P37 and P45, with equivalent simulations. Horizontal scan data produced very similar distributions. The base-level simulation (red circles and lines), equivalent to case R_{11} above, modeled optical transport and did not consider electronic effects. A perfectly smooth surface was assumed initially for the GS20 and MAPMT glass, which is parametrised by a 'polish' factor $P = 1.0$. The effect of a non-perfect GS20 surface was then investigated with $P = 0.8$ (blue circles and lines) and $P = 0.5$ (magenta circles and lines). The pure optical-transport calculations were then smeared using simple parametrisations of electronic noise and cross talk in the MAPMT. The resultant distribution at $P = 0.8$ is displayed with blue squares and dashed lines.

The mean amplitudes in plots a) and c), which are the mean channels of the pulse-height spectra, have been normalised so that the highest mean amplitude in each distribution is 1.0. The relative widths plotted in b) and d) are the

ratios of the standard deviations and means of the pulse-height spectra.

The simple model of electronic cross talk assumes that signal leakage from one pixel to a nearest neighbour can be approximated by sampling from a Gaussian distribution centered at 3% of the signal amplitude (number of scintillation photons) with a width (σ) of 3% of the signal amplitude. Measured cross-talk values for the H12700 [29] range from $\sim 1\%$ to $\sim 7\%$. For each nearest neighbour, a randonly-generated leakage signal is then subtracted from the pixel signal and added to the neighbour. For pixel P_j, the nearest neighbours are $P_{j-8}, P_{j-1}, P_{j+1}, P_{j+8}$ (if the neighbour exists). Actual cross talk [29] is rather more complicated as the magnitude varies considerably from pixel to pixel, the spectrum is not Gaussian and the cause can be both misrouting of photoelectrons through the dynode chain and pickup effects at the electronic output side. None the less the model gives an idea of the magnitude of the effect.

Smearing of the signal due to noise has been sampled from a Gaussian of width (σ) obtained from the measured widths of the pedestals of the ADC spectra [28]. The widths are equivalent to ~ 2 detected photons and at this level the effect of noise is small compared to cross talk.

Comparing measurements with the base-level simulation, the latter underpredicts the spreading of scintillation light from its point of origin. It gives a position-dependent distribution of mean pulse height which is too flat close to a pixel centre, and too steep close to a pixel boundary. When imperfect polish is introduced, this increases the scintillation-photon spreading. A value $P = 0.5$ overpredicts the spreading to adjacent pixels while $P = 0.8$ is closer to the measurement, although it still gives a distribution which is too flat near the pixel centre. When 3% cross talk (see above) is introduced at $P = 0.8$ the apparent signal spreading is increased significantly and is similar to the $P = 0.5$ case with no cross talk. Thus it is difficult to separate the two effects through comparison with the present measurements.

Non-uniform sensitivity of the photocathode, as investigated for the similar H8500 MAPMT [30], is a further potential source of distortion of the measured response. It has not been included in the present calculations, pending a better knowledge of the sensitivity of the employed H12700A MAPMT.

4.3. Simulation of Potential Background

Fast neutrons and gamma rays are a potential source of background at the ESS. Here the measured and simulated response of a SoNDe module to these backgrounds is presented. The measurements used the same experimental setup as for the proton scan (Sec. 4.2) and were made on the same day using the facilities of the Lund University Source Test Facility [31].

4.3.1. Neutron and Gamma-ray Source Measurements

The SoNDe module was irradiated with AmBe neutron and ^{60}Co gamma-ray sources. A Pb brick of thickness 20 mm, placed between the AmBe source and detector, attenuated gamma rays. A CH_2 block of thickness 50 mm, placed

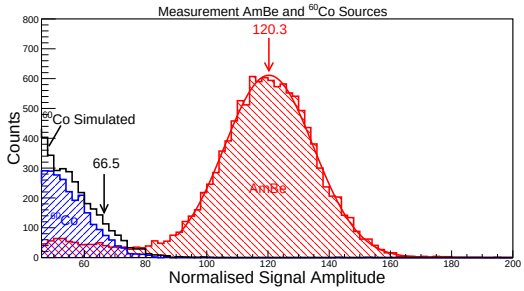

Figure 11: Pulse Height Measurement. Blue: ^{60}Co gamma-ray source, red: AmBe neutron and gamma-ray source. The smooth curve is a Gaussian fit to the measured neutron-capture peak. The black line shows the end-point of the simulated ^{60}Co spectrum.

detector-side of the Pb, provided some moderation of the fast neutrons. The signal amplitude (Fig. 11) has been reconstructed from a nine-pixel cluster sum centered on pixel P37. The AmBe run shows a prominant thermal-capture peak (energy 4.78 MeV) at channel 120.3, which has been normalised to coincide with the simulated number of detected scintillation photons. Measurements of the SoNDe response to a collimated thermal neutron-beam produced at a reactor [13] show that the capture peak is very similar to that obtained with AmBe. Background in the AmBe spectrum from fast neutrons and gamma rays does not pollute the neutron-capture peak significantly. This peak may thus be compared to that of the thermal-neutron simulation (Fig. 12), which does not include the fore-mentioned background.

The ^{60}Co spectrum shows the end point of the smeared Compton distribution and compares it to the simulated distribution (Sec. 4.3.2). The simulated edge (mean energy ~ 1.0 MeV) from the unresolved 1.17 and 1.33 MeV gamma-rays aligns with channel 66.5 while the slope of the measured spectrum, normalised on the same basis as the neutron-capture peak, falls systematically ~ 4 channels lower. Thus the edge position for the measured ^{60}Co spectrum is estimated to fall at channel 63 ± 6.

Compared to Compton electrons, the alpha-triton final state obviously produces less scintillation light per unit energy deposited, which is modeled in the simulation via the Birks formalism (Eq. 2).

4.3.2. Simulated Neutron and Gamma-ray Response

The simulated signal amplitude, in terms of number of scintillation photons, for fast neutrons at incident energies from 0.1 MeV to 100 MeV is compared to the thermal-neutron (0.025 eV) response in Fig. 12(a). The displayed pulse heights are cluster sums of the 9 pixel signal amplitudes centred on P37. At low energies, where the fast neutron has insufficient energy to fragment the nuclei of the glass, there is a weak signal from neutron capture on ^{6}Li. Where the neutron has sufficient energy to break up nuclei, a continuum emerges from the

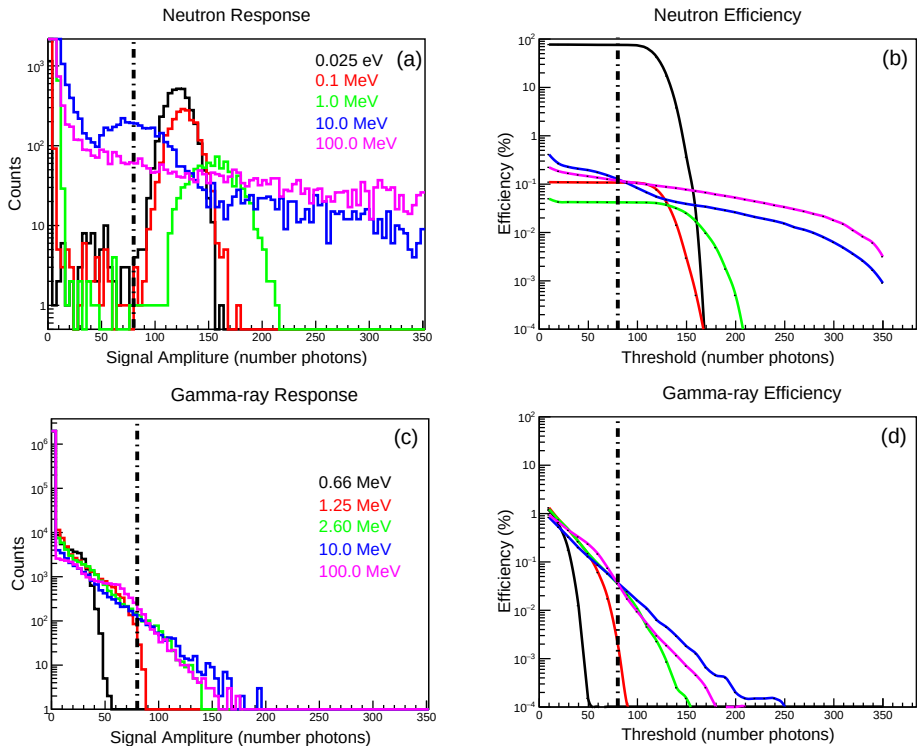

Figure 12: (a) Fast-neutron, signal amplitude compared to that of 0.025 eV neutrons. (b) Neutron efficiency as a function of threshold. The colour coding is as for plot (a). (c) Gamma-ray signal amplitudes for a range of incident energies. (d) Gamma-ray efficiency as a function of threshold where the colour code is as plot (c). The dot-dash line in all panels marks a threshold level of 80 photons. Note that the thermal-neutron spectrum resulted from 5×10^3 incident particles, while the fast-neutron and gamma-ray spectra resulted from 2×10^6 incident particles.

interactions of final state protons and light ions, becoming more pronounced as the energy increases.

Neutron detection efficiency is displayed as a function of threshold in Fig. 12(b). The 80-photon threshold level results in insignificant loss of thermal efficiency (76%). At fast-neutron energies between 0.1, 1.0 MeV, this threshold does not give significent background suppression, while at higher energies it offers limited suppression. Neutron detection efficiency at the 80-photon threshold is given in Table 1, for a range of energies. A fast-neutron efficiency of around 0.1% is similar to that obtained with a 2.54 cm diameter ^{3}He proportional counter [32, 33] operating at 10 bar, but around a factor 10^2 larger than the ^{10}B-coated 'Multi Blade' detector [25] developed for ESS.

The signal-amplitude spectra of the SoNDe module at incident gamma-ray energies from 0.66 MeV to 100 MeV have also been simulated. Fig. 12(c) displays the spectra, in terms of number of scintillation photons, where the signal amplitude was reconstructed as for neutrons. Gamma-ray spectra show a quite

diffuse Compton edge up to energies ~ 1 MeV, but at higher energies secondary electrons from Compton or pair-production processes have too much energy to stop in ~ 1 mm of glass and the distributions appear quite similar from 2.6 up to 100 MeV.

Gamma-ray detection efficiencies, as a function of detection threshold, are given in Fig. 12(d). A threshold of 80 photons (Table 1) gives complete suppression of low energy (≤ 1 MeV) gamma rays and very effective suppression at higher energies. The efficiency of 0.002% for ^{60}Co gamma rays (1.25 MeV) appears higher than that measured for a 2.54 cm, 10 bar ^{3}He tube [33], but here the efficiency values are extremely sensitive to applied thresholds.

Gamma Source	Eff. (%)	Neutron Source	Eff. (%)
0.66 MeV	0.0	0.025 eV	75.8
1.25 MeV	0.002	0.1 MeV	0.108
2.60 MeV	0.035	1.0 MeV	0.042
10.0 MeV	0.037	10.0 MeV	0.127
100.0 MeV	0.036	100.0 MeV	0.119

Table 1: Detection efficiency for gamma rays and neutrons at a threshold of 80 scintillation photons.

The relative signal amplitude from thermal neutrons and gamma rays has been calculated using a Birks factor k_B (Eq. 2) of 0.01 g/cm^2/MeV. The neutron capture peak occurs at 120.3 photons. For ^{60}Co, the two gamma-ray lines have Compton edges at 0.96 and 1.12 MeV, producing mean signal amplitudes of 61 and 72 photons respectively, with the mean of the two at 66.5 photons. The simulated ratio of Compton edge to n-capture peak (0.55) is consistent with the measured ratio of 0.52 ± 0.05 (Sec. 4.3.1).

4.3.3. Comparison with proton data

The measured neutron and gamma-ray pulse-height spectra are directly comparable with the proton data, which were collected on the same system, very close in time. For the vertical scan point closest to the centre of P37, the measured 9-element sum shows a peak at channel 101.8, while the equivalent simulated value is 99.1.

Taking the ratio of proton-peak pulse height to neutron-capture-lpeak pulse height, the measured value is 0.85 ± 0.02, while the simulation gives values of 0.82 at $k_B = 0.01$ g/cm^2/MeV and 0.93 at $k_B = 0.02$ g/cm^2/MeV.

Note that deuteron-beam scans are also reported in Ref. [11] and there the proton and deuteron data are directly comparable. The measured ratio of deuteron-to-proton pulse height [11] was 0.80 while the simulation gives 0.79 with $k_B = 0.01$ g/cm^2/MeV and 0.74 with $k_B = 0.02$ g/cm^2/MeV. Thus the simulation of proton, neutron-capture, deuteron and gamma-ray pulse height is consistent with a value close to 0.01 g/cm^2/MeV. Note that direct comparison

with the alpha-scan data was not possible as this was performed with a different SoNDe module and DAQ system.

5. Summary and Conclusions

A Geant4-based simulation of the SoNDe module, designed for thermal-neutron detection at ESS, is described. Transport of scintillation photons through the glass scintillator and MaPMT window has been used to study the spreading of the optical signal away from the interaction point in the scintillator. This was performed for a variety of scintillator grooving and optical coupling options. The likely experimental configuration, with an ungrooved scintillator and no optical-coupling between the scintillator and MAPMT, was found to give low collection efficiency for the scintillation photons, but results in tighter containment of the detected photons close to their point of origin, a goal of the SoNDe design.

Simulations of the scintillation signal for different incident particles have been compared to equivalent measurements made with alpha-particle, gamma-ray and neutron sources, as well as beams of 2.5 MeV protons and deuterons.

An x-y scan, in 1 mm steps, of a collimated alpha-particle source across the face of a SoNDe module was simulated and compared with measurements. After collimation the illuminated 'spot' on the GS20 was around 1.3 mm in diameter. Excellent agreement was obtained, using the base-level simulation, on the drop in signal amplitude as the interaction position moves away from the centre of a pixel of the MaPMT. However the simulation tended to underestimate the degree of light spreading slightly.

Finer-grained position scanning, in 0.5 mm steps, was implemented using the LIBAF proton beam at Lund, which has a beam spot of $\sim 100\,\mu$m diameter on target. The measured position dependence of the scintillation signal shows some discrepany with the equivalent calculation of the fall of the scintillation signal, as the interaction position is moved away from a pixel centre. The base-level simulation, which assumes perfectly polished reflecting surfaces, gives too small a variation close to the pixel centre and too rapid a fall at the pixel border. It underpredicts the amount of scintillation light spreading to adjacent pixels.

The simulation was extended to include non-perfect reflecting surfaces. As the smearing from perfect specular reflection is increased, the spreading of the optical photons from point of production also increases. Similarly, the apparent amount of signal spreading increases when the effects of electronic cross talk and noise in the MAPMT and associated electronics are folded into the simulation. Much better correspondence between simulation and measurement has been achieved using a surface polish factor $P = 0.8$ and assuming that on average 3% of a pixel signal crosses to its neighbour. However a more detailed knowledge of the SoNDe module is required to quantify the relative contributions of these effects. A measurement of cross talk and photocathode sensitivity, for the actual MAPMT used in the measurements could be performed with a fine-beam laser source. Although the GS20 surface appears smooth to the naked eye, it would

be desirable to investigate its structure more microscopically, or alternatively to make detailed studies of the reflection of a fine optical beam from points on the surface.

The signal from AmBe neutron and ^{60}Co gamma-ray sources was simulated and compared to measurements with the SoNDe module. The relative strength of the signals from neutron capture and Compton scattering of gamma rays are consistent with a Birks parameter of 0.01 g/cm^2/MeV. Based on this comparison, the detection efficiency, as a function of applied pulse-height threshold, has been simulated for thermal neutrons, fast neutrons and gamma rays. A threshold equivalent to 80 detected scintillation photons gives a thermal-neutron efficiency of 75.8%. Gamma rays up to 1 MeV are not detected at this threshold and at higher energies have low efficiencies ($< 0.04\%$). The fast-neutron efficiency is somewhat higher at the 0.1% level, which is comparable to a typical ^{3}He tube but a factor $\sim 10^2$ larger than a ^{10}B -coated thermal-neutron detector.

A comparison between simulation and measurement of the relative pulse height from neutron-capture, $\sim$ 1.0 MeV gamma rays, 2.5 MeV protons and 2.5 MeV deuterons is consistent with a Birks parameter of $k_B = 0.01$ g/cm^2/MeV. However the general validity of this value for a broader range of particle types and differential energy loss dE/dx remains to be investigated.

Acknowledgements

We thank the following organisations for supporting this work: the UK Science and Technology Facilities Council (Grant No. ST/P004458/1), the UK Engineering and Physical Sciences Research Council Centre for Doctoral Training in Intelligent Sensing and Measurement (Grant No. EP/L016753/1), the European Union via the Horizon 2020 Solid-State Neutron Detector Project (Proposal ID 654124), and the BrightnESS Project (Proposal ID 676548). We also thank the LIBAF team at Lund University for the provision and operation of their excellent proton beam. The provision of detector and electronics hardware by the SoNDe collaboration and the Lund Source Test Facility is gratefully acknowledged.

References

[1] R. Garoby *et al.*, Physica Scripta, 93(1) (2017), 014001.

[2] S. Peggs *et al.*, ESS Technical Design Report [ESS-2013-0001]. Technical report, European Spallation Source, 04 2013.

[3] K. H. Andersen *et al.*, Nucl. Instr. and Meth. A 957 (2020), 163402.

[4] S. Jaksch *et al.*, Nucl. Instr. and Meth. A 762 (2014), 22. `https://arxiv.org/abs/1403.2534`

[5] S. Jaksch *et al.*, arXiv 1707.08679, 2017. https://arxiv.org/pdf/1707.08679.

[6] S. Jaksch *et al.*, "Recent Developments of SoNDe High-Flux Detector Project", Proc. Int. Conf. on Neutron Optics (NOP2017), JPS Conf. Proc. 22 (2018), 011019.

[7] 'Scintillator detector with high count rate', EPO patent application 102014224449.8.

[8] GS20 scintillating glass, https://scintacor.com/products/6-lithium-glass/.

[9] Hamamatsu H12700 Series Flat Panel Multianode PMT assembly, https://www.hamamatsu.com/resources/pdf/etd/H12700A_TPMH1348E.pdf

[10] IDEAS Integrated Detector Electronics AS, https://ideas.no.

[11] E. Rofors *et al.*, Nucl. Instr. and Meth A 984 (2020), 164604.

[12] E. Rofors *et al.*, Nucl. Instr. and Meth. A 929 (2019), 90.

[13] E. Rofors *et al.*, arXiv:2010.0637 [physics.ins-det] (2020).

[14] J. Allison *et al.*, Nucl. Instr. and Meth. A 835 (2016) 186-225, and references therein

[15] Geant4 Physics Reference Manual, Release 10.6, 2020, http://geant4-userdoc.web.cern.ch/geant4-userdoc/UsersGuides/PhysicsReferenceManual/fo/PhysicsReferenceManual.pdf

[16] Geant4 Book for Application Developers, Release 10.6, 2020http://geant4-userdoc.web.cern.ch/geant4-userdoc/UsersGuides/ForToolkitDeveloper/fo/BookForToolkitDevelopers.pdf

[17] P. Gumplinger, Optical Photon Processes in Geant4, Users' Workshop at CERN, Nov. 2002.

[18] Optical Cement EJ-500, https://eljentechnology.com/products/accessories/ej-500.

[19] J. B. Birks, The Theory and Practice of Scintillation Counting, Pergamon Press, Oxford U.K., 1964.

[20] TiO_2 based reflective paint, https://eljentechnology.com/products/accessories/ej-510-ej-520.

[21] M.P. Hehlen *et al.*, J. Appl. Phys. 124 (2018),124502.

[22] Optical Glass Data Sheets, Schott AG Advanced Optics, www.schott.com/advanced_optics.

[23] R. Brun and F. Rademakers, Nucl. Instr. and Meth. A 389 (1997) 81. http://root.cern.ch/.

[24] A. Khaplanov *et al.*, J. Inst. 8 (2013), 10025, https://arxiv.org/abs/1306.6247

[25] G. Mauri *et al.*, J. Inst. 13 (2018), 03004, https://arxiv.org/abs/1712.05614

[26] V. I. Tretyak, Astroparticle Phys. 33 (2010), 40.

[27] Lund Ion Beam Analysis Facility (LIBAF), http://www.nuclear.lu.se/forskning/tillaempad-kaernfysik/libaf/.

[28] J. Scherzinger *et al.*, Appl. Radiation and Isotopes 127 (2017), 98.

[29] M. Calvi *et al.*, J. Inst. 10 (2015), 09021, https://arxiv.org/abs/1506.04302

[30] R. A. Montgomery *et al.*, Nucl. Instr. and Meth. A 695 (2012), 326.

[31] F. Messi *et al.*, "The neutron tagging facility at Lund University", IAEA Technical Report on Modern Neutron Detection (2017), https://arxiv.org/abs/1711.10286

[32] G. Mauri *et al.*, Eur. Phys. J. Tech. and Instr. 6 (2019), Article 3, https://arxiv.org/abs/1902.09870v1

[33] F. Piscitelli *et al.*, Eur. Phys. J. Plus 135 (2020), 577, https://arxiv.org/abs/2002.08153v1

Appendix

Appendix A: Conference posters

Response of a Li-glass/multi-anode photomultiplier detector to α-particles

Poster presented 2018 at the *International Workshop on Position Sensitive Neutron Detectors (PSND)* in Jülich, Germany. For further details refer to Paper II and Sec. 2.2.

Response of a Li-glass/multi-anode photomultiplier detector to α-particles from ^{241}Am

Emil ROFORS[1], Laura BOYD[3], Kevin FISSUM[1], Richard HALL-WILTON[2, 4], Ramsey AL JEBALI[2,3], Vendula MAULEROVA[1, 2], Nicholai MAURITZSON[1, 2], Rachel MONTGOMERY[3], Hanno PERREY[1, 2], John R. M. ANNAND[3]

[1]Lund University, Sonnig Group, Lund, Sweden
[2]European Spallation Source, Detector Group, Lund, Sweden
[3]University of Glasgow, Nuclear Physics Group, Glasgow, Scotland
[4]Mid-Sweden University, SE-851 70 Sundsvall, Sweden

GS20 ^{6}Li scintillator

A 1 mm thick sheet of ^{6}Li enriched, Ce-activated aluminosilicate glass scintillator, GS20 from Scintacor, converted the incoming alpha particles to light. Thermal neutrons react in the scintillator through ^{6}Li(n, α)^{3}H. The resulting high energy alpha particle and tritium deposit their energy in ~5-30 µm of the scintillator. The tritium and alpha particle generates around 6000 scintillation photons. As opposed to neutrons, the alpha particles in this study all deposit their energy at the surface of the scintillator.

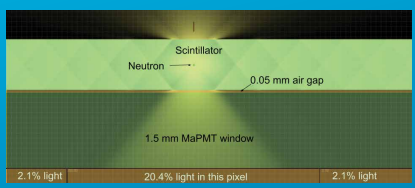

Ray-trace model of the light emitted from a neutron or alpha event in the center of the scintillator. 20% of the scintillation light reaches the pixel right under the event, 2% spread to each neighbouring pixel.

Collimated alpha source

A thin-windowed ^{241}Am source, placed in 3D-printed collimators was used to irradiate the scintillator with alpha particles. The alpha particles have an average energy of ~5.5 MeV. This is close to the Q-value of ^{6}Li(n,α)^{3}H and is a good candidate particle to study neutron interactions in GS20, being both easier to access and manage.

Scan pattern

The collimated source was mounted on a 2D motorised arm that scanned the scintillator surface in 1 mm steps. At each position 10000 alpha events were measured, corresponding to about 10 minutes measuring time.

Multi-anode Photomultiplier Tube

In a multianode photomultiplier tube (MaPMT), the light from alpha particles becomes pulses of electrons. The Hamamatsu H12700 MaPMT consists of 64 6 · 6 mm^2 pixels with complete PMTs that each have a chain of dynnodes that amplify the photoelectrons generated by the scintillation light.

high voltage power supply

Pulse of electrons

At the anodes the electrons have reached a high enough number to be measured. The 64 MaPMT pixels' signals were delayed through about 40 m cable for the electronics to have time to generate a gate signal.

NIM/VME modules

The charges from the MaPMT were processed using standard NIM/VME signal-processing electronics. The system was triggered on dynode 10 from the MaPMT, a common OR signal. The trigger generated a 200 ns gate that was timed to integrate the arriving pixel signals in 64 QDCs and store the charge values, event by event for analysis.

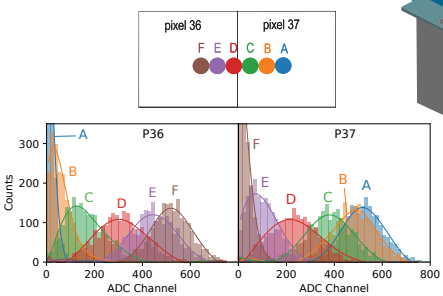

The colored peaks are from alphas measured in pixel 36 and pixel 37. The aplha irradiation spot was moved in mm steps between the pixels as shown in the points A to F in the top pixel map. The colored spectras show how the scintillation light is spreading between the pixels. More and more of the scintillation light reaches the neighbouring pixel as the irradiation occurs closer to the edge. The light proportion in each pixel is shown below, as well as Ray-tracing simulated results. At the edge between the pixels, equal ammounts of scintillation light reaches both pixels. The sum of the two pixels' signalas is constant, meaning the same ammount of light is detected in each position.

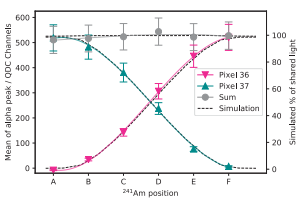

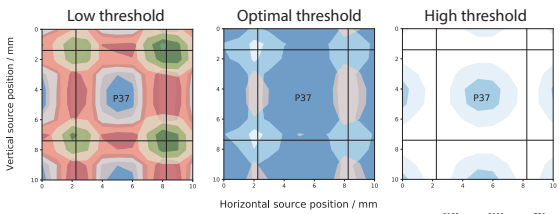

Contour plots of the multiplicity distributions for pixels lying near P37 for different thresholds as a function of alpha-particle beam irradiation location. With a low threshold (QDC channel 100) the detector sees 1-4 pixels above threshold for each alpha particle. As shown in the left plot, irradiation at the pixel corners triggers 3 or 4 pixels, at the edges there are 2 pixels above threshold and only in the center of the pixel will the multiplicity be 1. For this detector it is optimal to maximise the multiplicity 1 area. It was found to be the biggest with the threshold set at QDC channel 235, shown in the middle plot. The right plot shows a threshold set too high at QDC channel 500.

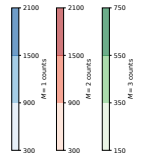

This project is funded by the Horizon 2020 Framework Programme of the European Union. Project number 654124.

Solid-State Neutron Detector

EUROPEAN SPALLATION SOURCE

DETECTOR GROUP

LUND UNIVERSITY

SOurce-based NeutroN Irradiation Group
Department of Nuclear Physics
Lund University

Thermal-neutron response of a SoNDe Detector measured at IFE

Poster presented 2018 at the *Swedish Nuclear Physics Meeting SFS-KF* in Uppsala, Sweden. For further details refer to Paper IV and Sec. 2.4.

Thermal neutron response of a SoNDe detector measured at IFE

Emil ROFORS[1], Kevin FISSUM[1], M. Jagd Christensen[2], Ramsey AL JEBALI[3,4], Kalliopi KANAKI[3], Nicholai MAURITZSON[1], Hanno PERREY[1, 3], The SoNDe Collaboration[1, 3, 5, 6, 7]

[1]Lund University, Sonnig Group, Lund, Sweden
[2]European Spallation Source, Data Managment & Software Center, Copenhagen, Denmark
[3]European Spallation Source, Detector Group, Lund, Sweden
[4]University of Glasgow, Nuclear Physics Group, Glasgow, Scotland
[5]IDEAS, Oslo, Norway
[6]Forschungszentrum Jülich, Jülich Centre for Neutron Science, Jülich, Germany
[7]Laboratoire Léon Brillouin, Paris, France

GS20 ^{6}Li scintillator

A 1 mm thick sheet of ^{6}Li enriched, Ce-activated aluminosilicate glass scintillator, GS20 from Scintacor, converted the incoming neutrons to light. Thermal neutrons react in the scintillator through $^6\mathrm{Li}(n, \alpha)^3\mathrm{H}$. The resulting high energy alpha particle and tritium deposit their energy in ~5-30 µm of the scintillator. The tritium and alpha particle generates around 6000 scintillation photons.

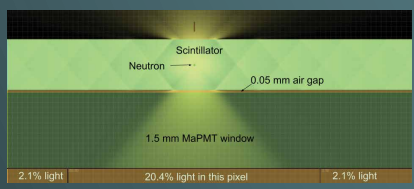

Ray-trace model of the light emitted from a neutron in the center of the scintillator. 20% of the scintillation light reaches the pixel right under the event, 2% spread to each neighbouring pixel.

Incoming neutrons

Thermal neutrons from the R2D2 beamline at IFE in Norway were collimated to 1 and 3 mm diameter beams. The energies were selected through a monochromator to 2.0 and 2.4 Å.

Scan pattern

The collimated beam of neutrons was scanned across the scintillator. The detector was mounted on a 2D motorised table moving in 1 mm steps. At each position 15 s of neutrons were measured.

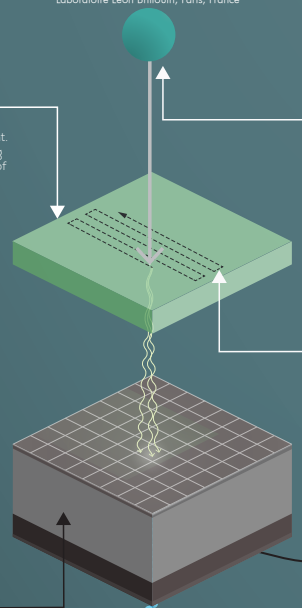

Multi-anode Photomultiplier Tube

In a multianode photomultiplier tube (MaPMT), the light from converted neutrons becomes pulses of electrons. The Hamamatsu H8500c/H12700 MaPMT consists of 64 6 · 6 mm² pixels with complete PMTs that each have a chain of dynnodes, amplifying the photoelectrons generated by the scintillation light.

Pulse of electrons

At the anodes the electrons have reached a high enough number to be measured. 64 single-ended singnals of electron pulses are passed to the readout module.

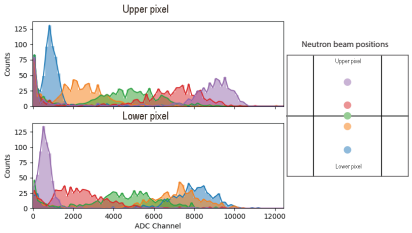

The colored peaks are neutron peaks measured in two pixels as the neutron beam is moving from the upper pixel to the lower. More and more of the scintillation light reaches the lower pixel until only some % is left in the upper pixel. Gain variations in the MaPMT cause the peaks' shift in ADC channels between the two pixels.

Readout module

Triggered on the dynodes of the MaPMT, this electronics module registers the charge of the incoming electrons. Charge sensitive pre-amplifiers, digital logic triggers and all the nessecary electronics are contained in the 52 · 52 · 26 mm³ moadule. With a timing accuracy of under 100 ns and a count rate over 100 k counts per second, it is linear well up to 250 kHz for one 5 · 5 cm² module and to 100 MHz for a full 1 · 1 m².

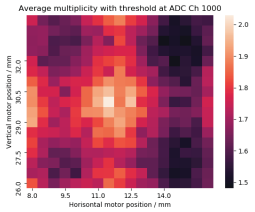

Multiplicity here is defined as the number of pixels that are above threshold for a given event. The average multiplicity for 10000 neutrons as the beam scanned around a 4-pixel corner shows how neutrons might be counted multiple times because of scintillation light spreading to neighbouring pixels.

Add them together

For the ESS implementation of SoNDe, 400 modules will be assembled together. Since the electronics are contained within the footprint of the scintillator and MaPMT, the SoNDe modules can be combined to build any shape of detector.

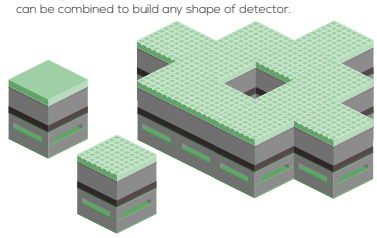

This project is funded by the Horizon 2020 Framework Programme of the European Union. Project number 654124.

Performance tests of a pixelated thermal-neutron detector using a low intensity proton beam

Poster presented 2019 at the *Ion Beam Analysis* in Antibes, France. For further details refer to Paper III and Sec. 2.3.

Performance tests of a pixelated thermal neutron detector using a low intensity proton beam

J. Pallon[a], E. Rofors[a], N. Mauritzson[a], R. Al Jebali[b,c], J.R.M. Annand[c], L. Boyd[c], N. De La Rosa[a], M. Elfman[a], K.G. Fissum[a], R. J. W. Frost[a], R. Hall-Wilton[b,d], P. Kristiansson[a], R. Montgomery[c], E. J. C. Nilsson[a], H. Perrey[a], B. Seitz[c]

Corresponding author email: Jan.Pallon@nuclear.lu.se

[a] Division of Nuclear Physics, Department of Physics, Lund University, Box 118, SE-221 00 Lund Sweden,
[b] Detector Group, European Spallation Source ERIC, SE-221 00 Lund, Sweden
[c] SUPA School of Physics and Astronomy, University of Glasgow, Glasgow G12 8QQ, Scotland, UK
[d] Mid-Sweden University, SE-851 70 Sundsvall, Sweden

Introduction

The Solid-state Neutron Detector (SoNDe)[1] is a position sensitive thermal neutron detector that is being developed to match the high fluxes of the European Spallation Source (ESS), currently being built in Lund. Through the reaction $^{6}Li(n,\alpha)^{3}H$ with Q=4.78 MeV, α and ^{3}H ions are created and depositing their kinetic energy within 5-30 µm in the scintillator [2]. A Hamamatsu H12700A multi-anode photomultiplier tube (MAPMT)[3] converts the light into an electric signal.

To investigate the detailed positional response, the GS20 Li-glass was excited with a focused proton beam. Spread of scintillation light within the scintillator and border effects between MAPMT pixels were mapped using motor controlled scans of the detector across the proton beam.

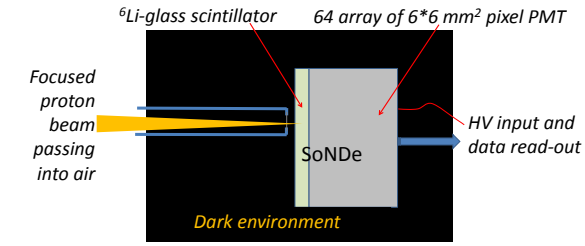

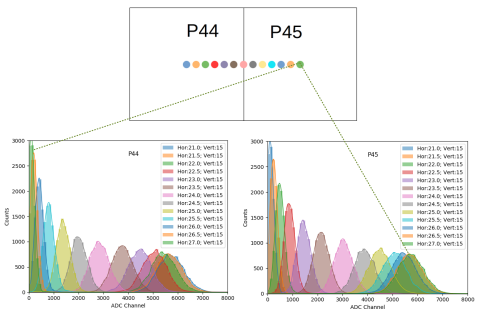

The colored peaks are from proton hits in pixel 44 and 45. The irradiation spot was moved in 0.5 mm steps between the pixels as indicated in the top figure. The colored spectra show how the scintillation light is spreading between pixels. More and more of the scintillation light reaches the neighbouring pixel as the irradiation approaches the edge.

The light proportion in each pixel is shown below. At the edge equal amounts of scintillation light reaches both pixels. The sum of the two pixels' signal is constant (gain corrected means).

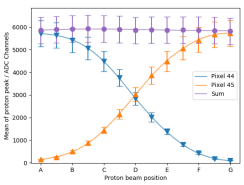

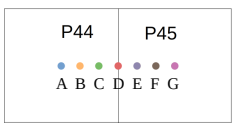

Methods

A proton beam of 2.5 MeV energy at the LIBAF microbeam setup was brought out from vacuum condition through a thin silicon nitride window passing a few mm of air and focused to about 50 µm diameter spot while being observed through a microscope with a TV-camera. The object and aperture slits were closed until the beam was hardly observable.

The SoNDe detector was placed on the motorized sample stage and its read-out was used to monitor the proton rate while the slits were closed further until the count-rate was below 10 000 c/s. After position calibration, the detector was scanned in front of the stationary beam in different patterns across the detector pixels.

Pixel layout and scanned area

Threshold: ADC channel 900

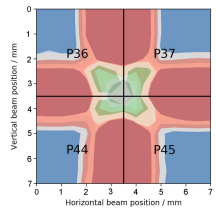

Threshold: ADC channel 1500

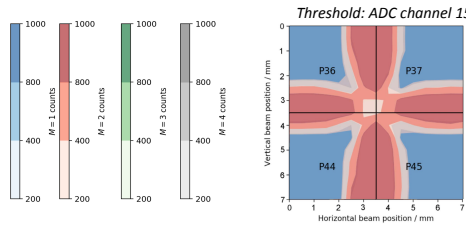

Multiplicity zones in four quadrants of pixels around a pixel corner. Closest to the corner, 4 pixels are above threshold (grey zone, top image). As the protons hit farther from the pixel boundaries, the multiplicity goes down to M = 3 (green), M = 2 (red) and to M = 1 (blue) in the center areas of the pixels. With higher ADC channel thresholds the multiplicity decreases, see middle and bottom images. At the threshold 2300 (bottom) a dead region begins to form.

Threshold: ADC channel 2300

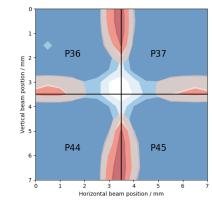

Discussion

The observations done with the focused proton beam reveals details in much higher resolution than the previously performed detector characterization done using a ^{241}Am alpha source [4]. In a next step deuterons are to be used. Thus by having the three different ions p, d and α it will be possible to determine Birk's constant that describes how much scintillation light that is created for different ions. This constant is unknown for the GS20 scintillator. By combining the measurement into a GEANT 4 simulation a more detailed understanding of the particles and reactions involved in the scintillation process will be obtained. This understanding will be essential for optimizing the parameters for ESS use of the SoNDe detector.

[1] Jaksch, S. et al. (2018). Recent Developments SoNDe High-Flux Detector Project. NOP2017, Journal of the Physical Society of Japan. https://doi.org/10.7566/jpscp.22.011019
[2] https://www.crystals.saint-gobain.com/sites/imdf.crystals.com/files/documents/glass-scintillator-material-data-sheet_69772.pdf
[3] https://www.hamamatsu.com/resources/pdf/etd/H12700_TPMH1348E.pdf
[4] Rofors, E. et al.(2019). Response of a Li-glass/multi-anode photomultiplier detector to α-particles from 241Am. NIMA, 929, 90–96. https://doi.org/10.1016/j.nima.2019.03.014

Appendix B: MAPMT Scanner GUI

To streamline the process of controlling motors, reading positions, starting and stopping data readouts etc., a graphical user interface (GUI) called `MAPMT Scanner GUI` was developed by the author. The interface, was built in `QT Designer`, and functions and calls were scripted in `Python`, see Fig 1. `MAPMT Scanner GUI` provides an interface to the various brands of motor controllers and readout systems that were used. The current position of the particle beam or laser in use is shown on a MAPMT map, which is clickable to allow easy XY-movement of the beam or detector (depending on the measurement). Once a scan has been configured, its progress can be monitored.

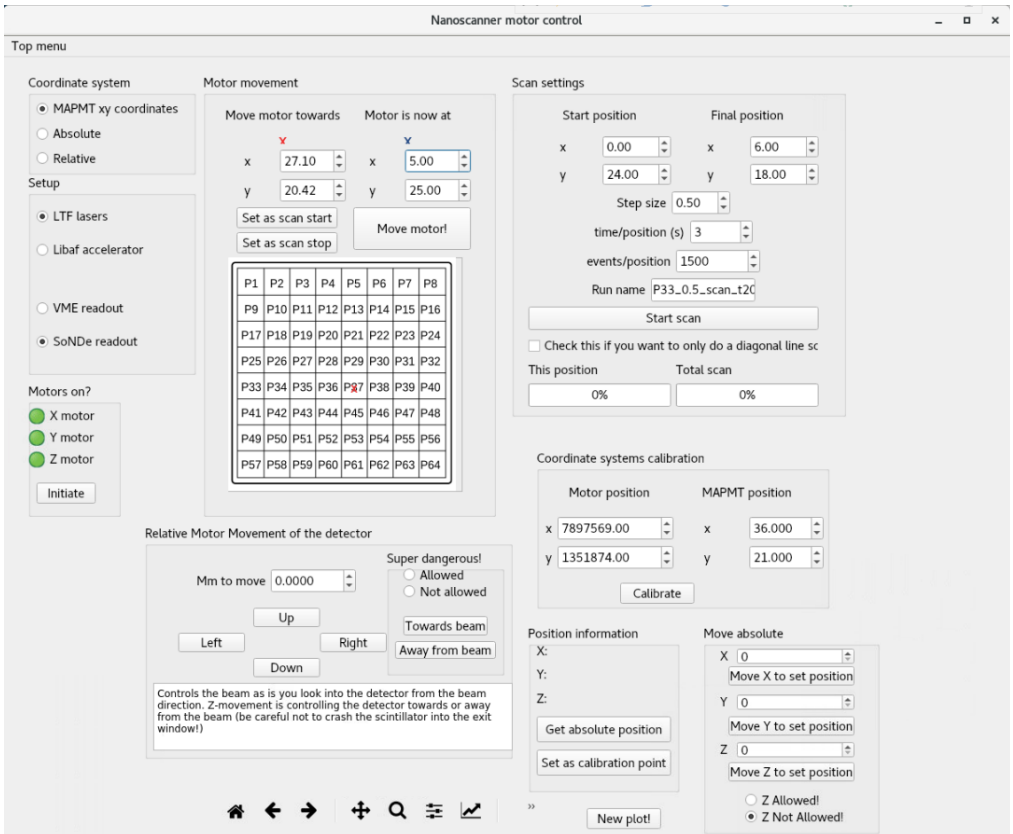

Figure 1: A graphical user interface built in QT Designer to facilitate controlled irradiations and scans across the detector.

Appendix C: Presentations

Talks

- 2016-04-28, "Fast Photoneutron Detection", ESS detector seminar, Lund, Sweden
- 2016-05-06, "Building a boron-10 based neutron detector", Central European Training School on neutron techniques, Budapest, Hungary
- 2016-09-09, "From neutron to data", CERN School of computing, Mol, Belgium
- 2018-05-16, "Thermal-neutron response of a SoNDe detector measured at IFE", International Workshop on Position Sensitive Neutron Detectors (PSND), Jülich, Germany
- 2019-10-24, "Characterization of the Solid-State Neutron Detector (SoNDe) using a low current proton beam", Swedish Nuclear Physics Meeting 2019, Lund, Sweden

Posters

- 2016-01-10, "Thermal-Neuron Detector for high-flux applications", MAXIVESS-FUN meeting, Lund, Sweden
- 2017-05-16, "Thermal-Neuron Detector for high-flux applications", Swedish Neutron Scattering Society annual meeting, Uppsala, Sweden
- 2018-05-16, "Response of GS20 to alpha radiation measured with multi-anode PMT", International Workshop on Position Sensitive Neutron Detectors (PSND), Jülich, Germany
- 2019-07-01, "Response of a Li-glass/MAPMT detector to α-particles from ^{241}Am PMT", European Conference on Neutron Scattering (ECNS), Saint Petersburg, Russia
- 2019-10-14, "Performance tests of a pixelated thermal neutron detector using a low intensity proton beam", Ion beam analysis 2019, Antibes, France

Appendix D: Outreach

Presentations

- 2018-02-01, "The European Spallation Source and why we want to count neutrons", 45 min breakfast lecture with questioning for the IDEON Rotary Club in Lund
- 2018-03-15, "Att räkna neutroner i en heliumkris", 45 min lecture, NMT-days in Lund
- 2018-03-20, "Neutroner, näringsliv och nya möjligheter", explained ESS and answered questions with a perspective on the industry around Skåne, `https://handelskammaren.com/evenemang/neutroner-naringsliv-och-nya-mojligheter/`
- 2018-11-09, "ESS och varför vi vill räkna neutroner", Stora Tillväxtdagen organised by Tillväxtverket
- 2019-01-17, "ESS and MAX IV for dummies", Enter the Loop lunch, `https://youtu.be/3PzFrsUppX0`
- 2019-03-20, "Why researchers love neutrons and the art of counting them", 45 min lecture, NMT-days in Lund
- 2019-03-21, "Att räkna neutroner i en heliumkris", Forskarturnen Husiebiblioteket, Malmö
- 2019-03-26, "Att räkna neutroner i en heliumkris", Forskarturnen Lindängens bibliotek, Malmö
- 2019-04-04, inspirational lecture for the technical preparatory program and high school students, Helsingborg
- 2019-10-09, "Att räkna neutroner i en heliumkris", Forskarturnen Lunds stadsbibliotek
- 2019-09-21, "Why researchers love neutrons and the art of counting them", Kulturnatten Lund

- 2020-04-16, inspirational lecture for the technical preparatory program, Helsingborg

Competitions

- 2016-08-26, Awarded for the best poster at the summer retreat of the research school COMPUTE on the theme scientific outreach
- 2017-07-04, "Att räkna neutroner i en heliumkris", won the 5-minute Science Slam at Swedish annual political gathering Almedalen, https://youtu.be/0Yz9VVWxLj8?t=3839
- 2017-10-04, "Att räkna neutroner i en heliumkris", won the 4-minute Science Slam in Lund called Forskar Grand Prix
- 2017-11-28, "Att räkna neutroner i en heliumkris", placed 4th in the finals of Forskar Grand Prix, broadcast on UR Jan 2018, https://youtu.be/RcwTMHCraPo?t=3520
- 2019/10/15: Won the Lund University rounds of Three-Minute Thesis (3MT) https://universitas21.com/get-involved/student-competitions/three-minute-thesis-competition/u21-three-minute-thesis-0

Interviews

- 2017-11-09, "Varför ska man tävla i Science Slam?", Lund University Magazine, LUM, https://www.lum.lu.se/varfor-ska-man-tavla-i-science-slam/
- 2018-02-23, "Globala forskningsnav med lokal affärspotential", Chamber of Commerce and Industry of Southern Sweden Magazine, number 4, 2017 (pages 18–19), https://handelskammaren.com/om-oss/tidningen-sydsvenskt-naringsliv-2/
- 2018-04-02, "Do You Know What a Neutron Detector Is? You Should.", interview on Academic Stories, https://academicstories.com/story/inspiring-ideas/do-you-know-what-a-neutron-detector-is-you-should

Others

- 2016-06-19, ESS booth at opening of MAX IV, answering questions from the public
- 2017-10-22, Vattenhallen Science Center, show and tell for people of all ages about ESS and MAX IV.
- 2018-10 to 2019-04, Supervised high school students from Peder Skrivares Skola in Varberg in building a radiation detector for their final year project.